Accession No. 65-07416

SID 65-816

ENGINEERING METHOD TO PREDICT SATURN V VEHICLE AND LAUNCH COMPLEX ENVIRONMENTS DUE TO ROCKET JET IMPINGEMENT

FINAL REPORT
CONTRACT NAS8-11407

29 JULY 1965

Prepared for the
George C. Marshall Space Flight Center
National Aeronautics and Space Administration

by

A. Africano
A. Africano
Principal Scientist - Propulsion Research

Approved by

F. G. Etheridge
F. G. Etheridge
Program Manager

W. H. T. Loh
W. H. T. Loh, V
Director

Power and Environmental Systems Department
Research and Engineering Division

NORTH AMERICAN AVIATION, INC.
SPACE and INFORMATION SYSTEMS DIVISION

FOREWORD

This final report is submitted by North American Aviation, Inc., Space and Information Systems Division (NAA/S&ID) to the National Aeronautics and Space Administration, George C. Marshall Space Flight Center (NASA/MSFC) in fulfillment of the technical requirements on Contract NAS 8-11407. The report includes the complete results of the 13-month program of analytical investigation and correlation with available experimental data on engineering methods to predict the force and heat load environments due to rocket jet impingement. The environments include jet plume descriptions from sea-level to near-vacuum altitudes and typical surfaces of the Saturn V Vehicle and Launch Complex simulated by canted or uncanted flat plates, cylinders, and spheres located at various axial and radial distances from the reference nozzle exit center origin.

The program was conducted under the direction of Mr. J. C. Cody, Contracting Officer's Representative, and Mr. J. L. Moses, Alternate, of the George C. Marshall Space Flight Center Propulsion and Vehicle Engineering Division, Thermal Engineering Section, Fluid Mechanics and Thermodynamics Branch, National Aeronautics and Space Administration, Huntsville, Alabama.

Principal S&ID Aerospace Sciences personnel contributing in the effort included Mr. A. Africano, Project Engineer and principal investigator (technical coordination, geometry of impingement, sea-level plume approximation, impingement forces, and general correlation studies); Dr. E. P. French (plume radiation study, gaseous and solid particles); J. W. Rolley, G. M. Hanley, and R. Norcross (convection heat transfer studies); R. J. Hoffman (Saturn S-II plume analysis computer program 7N-213 and study of shifting specific heat ratio); and R. Rashidian and F. J. Douglas (Apollo plume analysis computer program AP-214, including addition of freestream effect). Mr. F.G. Etheridge, Chief of Propulsion and Power Systems, was Program Manager for S&ID with responsibility for executing the program assigned to the Power and Environmental Systems Department, directed by Dr. W. H. T. Loh.

TECHNICAL REPORT INDEX/ABSTRACT

ACCESSION NUMBER	DOCUMENT SECURITY CLASSIFICATION
65-07416	UNCLASSIFIED

TITLE OF DOCUMENT	LIBRARY USE ONLY
ENGINEERING METHOD TO PREDICT SATURN V VEHICLE AND LAUNCH COMPLEX ENVIRONMENTS DUE TO ROCKET JET IMPINGEMENT. FINAL REPORT	
AUTHOR(S): A. AFRICANO	

CODE	ORIGINATING AGENCY AND OTHER SOURCES	DOCUMENT NUMBER
	NAA/S&ID RESEARCH AND ENGINEERING DIVISION	SID 65-816

PUBLICATION DATE	CONTRACT NUMBER
29 JULY 1965	NAS 8-11407

DESCRIPTIVE TERMS

SATURN V
ENVIRONMENTS (JET PLUME)
RADIATION HEAT TRANSFER
CONVECTION HEAT TRANSFER
IMPINGEMENT PRESSURES
PLUME FLOW FIELDS
CHARACTERISTIC VELOCITY

ABSTRACT

This report presents the results of investigations made during a 13-month study program on the prediction of forces and heat loads induced by rocket jet plume impingement on typical structures of the Saturn V Vehicle and Launch Complex simulated by flat, cylindrical, and spherical surfaces. Ambient environments of the jet plumes considered ranged from sea-level to near-vacuum conditions.

Topics discussed in the six major sections of the report include:

I. Program objectives, environments, and special problem areas.
II. Jet plume flow fields, approximate descriptions, method of characteristics, and influence coefficients for "standard" jet plumes.
III. Jet plume impingement geometry for true angle of streamline impingement on canted and uncanted flat plates and cylinders, and on spheres.
IV. Impact pressures due to jet plume impingement, with discussion of contributions of photon impingement (radiation), molecular impingement (stagnation pressure), and impingement of flowing gases (transport velocity effect).
V. Heat transfer due to jet plume impingement, covering radiation from gaseous and solid particle constituents, radiation from the impingement shock layer, convection heat transfer in the oblique, normal, stagnation, and turbulent flow regions, and the "characteristic velocity" concept of the heat transfer-impingement pressure relationship.
VI. Conclusions and recommendations.

FORM 131-V REV 11-64
PUBLICATIONS USE ONLY

ABSTRACT

This report presents the results of investigations made during a 13-month study program on the prediction of forces and heat loads induced by rocket jet plume impingement on typical structures of the Saturn V Vehicle and Launch Complex simulated by flat, cylindrical, and spherical surfaces. Ambient environments of the jet plumes considered ranged from sea-level to near-vacuum altitudes. Topics discussed in the six major sections of the report are as follows:

I. Program objectives, environments, and special problem areas.

II. Jet plume flow fields, approximate descriptions, method of characteristics, and influence coefficients for "standard" jet plumes.

III. Jet plume impingement geometry for true angle of streamline impingement on canted and uncanted flat plates and cylinders, and on spheres.

IV. Impact pressures due to jet plume impingement, with discussion of contributions of photon impingement (radiation), molecular impingement (stagnation pressure), and impingement of flowing gases (transport velocity effect).

V. Heat transfer due to jet plume impingement, covering radiation from gaseous and solid particle constituents; radiation from the impingement shock layer; convection heat transfer in the oblique, normal, stagnation, and turbulent flow regions; and the "characteristic velocity" concept of the heat transfer-impingement pressure relationship.

VI. Conclusions and recommendations.

CONTENTS

ILLUSTRATIONS

Figure Page

TABLES

I. INTRODUCTION - PROGRAM OBJECTIVES

This final report, submitted by North American Aviation, Inc., Space and Information Systems Division (NAA/S&ID) to the National Aeronautics and Space Administration, George C. Marshall Space Flight Center (NASA-MSFC) under Contract NAS 8-11407, documents and summarizes the results of the entire contract performance period, 29 June 1964 through 29 July 1965. The program comprised a 13-month investigation of the correlation between theoretical and experimental rocket jet plume impingement forces and heat loads to nearby structures as represented by categorized flat or curved surfaces, with the Saturn V Vehicle and Launch Complex utilized as a reference configuration.

A. STATEMENT OF WORK

The detailed purpose and scope of the program, as described in the Statement of Work, Appendix A of the procurement request (Reference 1), are quoted as follows:

"I. Introduction

A. Pressure and heat loads due to jet impingement could be detrimental to Saturn V vehicle and launch complex structures with scheduled or possibly inadvertent firing of solid or storable propellant motors. The objective of this project is to generate a reliable engineering method to predict the effects of jet impingement.

B. Currently available information is insufficient to accurately predict the heat transfer or the pressure loads resulting from an impinging jet. The important parameters affecting the heat transfer need to be established and analytical methods developed so that jet impingement phenomena can be predicted from given engine characteristics and impingement geometry. These analytical methods would be used to verify preliminary analyses for Saturn V vehicle and launch complex.

II. Scope

A. The contractor shall use his best efforts to develop an engineering method to predict space vehicle and launch complex environments due to rocket jet impingement. ("Environments" was agreed to be interpreted to mean jet plume and interactions with air flow and with flat, concave, and convex surfaces.)

B. Experimental work should include tests with both solid and storable propellant motors to establish the important parameters affecting heat transfer and impingement pressures. A method of analysis which completely describes the phenomena should be developed. The method of analysis should be correlated with test data and shown to be valid, as far as possible, for a wide variety of problems, including but not necessarily limited to the following:

1. Heating and pressure loads at various altitudes (sea level to near vacuum).

    a. Convective heating by the gas.
    b. Radiant heating from the solid particles.
    c. Radiant heating from the gas.
    d. Heating due to collision of solid particles on impingement area (also, experimental data on surface erosion caused by impinging solid particles would be of value).
    e. Effective thermal radiation from the jet for problems not involving direct jet impingement.

2. Geometric shapes to be considered:

    a. Flat plates at various angles to gas flow.
    b. Bodies with blunt leading edges (cylinder, sphere).

3. Location of the heated body relative to jet plume (The effect of immersion distance within the plume should be investigated).

4. Type of Motor:

   a. The effect of various propellant mixtures, combustion conditions, and jet exhaust constituents.
   b. Effect of solid particle size and density within the jets, e.g., relating chamber pressure to particle size, hence to the heating rate.
   c. The effect of nozzle expansion angle and shape."

The concepts and parameters in the foregoing tabulation indicate the wide variety of separate problem areas included in the overall jet plume environments problem. Although almost all program objectives have been substantially achieved, a few, which proved to be beyond the scope of the schedule effort of Reference 2, remain. Careful search of the literature in these few cases showed lack of any theory, or inadequate theory, together with inadequate general test data, leaving recourse to projection of model test data to the prototype design environment as the only practical expedient.

Fortunately, a considerable background of pertinent plume analysis and test experience has been accumulated in various space programs, notably in the S&ID Apollo and Saturn S-II Programs. This background has been drawn upon, as much as possible, in the conduct of the investigations described in this report. Rocket jet plume impingement testing, whether at sea level or at the simulated near-vacuum conditions approached in high-altitude test chambers, is generally very expensive; therefore, the results of the study of the degree of correlation possible between the existing or developed prediction methods and the available test data should serve to define future test programs more realistically and aid in reducing their costs.

The order of presentation of the topics included in the Statement of Work (Reference 1) has been revised to result in a logical progressive treatment of distinct facets of the complex overall plume problem. Thus, after completing discussion of "before and after" launch environments and of some special problem areas in this section of the report, the description of the jet plume flow field in Section II and of the analytical solid geometry of impingement in Section III provide the physical environments that are prerequisites for solution of the desired impingement pressure and heat transfer prediction methods in Sections IV and V. Results of the correlation studies are included after presentation of the analytical methods in Section IV and, for a clear understanding of the parameters and their units during the development of the analytical methods in Section V.

This final report is a summary of the results of all work performed under the contract, and is drawn principally from the detailed quarterly progress reports (References 3, 4, 5) submitted in accordance with contractual requirements following the first three quarterly periods. The tables, graphs, curves, sketches, photographs, and drawings, together with numerical examples which ensure use of consistent units in the variety of prediction equations, are presented in sufficient detail to provide a comprehensive grasp of the overall plume-impingement problem and the resulting prediction method.

B. ENVIRONMENTS BEFORE LAUNCH

A typical sea-level environmental relationship of the Saturn V launch vehicle to its umbilical tower and access and servicing platforms (Reference 6) is shown in Figure 1. Except for the booster blast deflectors (not shown), the elements depicted are those nearest the rocket at launch. While the basic relations developed for jet plumes apply in the case of scheduled or inadvertent firing of the major propulsion engines when the vehicle is still on the stand of Complex 39, the handling of the enormous quantity of generated heat is more a matter of gross damage prevention by the usual techniques of adequate heat-absorbing water or chemical-quenching fog sprays, or of determining blast damage potential in terms of TNT equivalent of the propellants, than a matter of determining precise jet plume descriptions. Nevertheless, since the jet plume is a starting point for such studies, available test data from large-engine, sea-level firings were investigated in addition to test data from models and plates specially instrumented for jet impingement studies at high-altitude environments.

Within the seventeen categories of solid and liquid propellant engines of the Saturn V (Figure 2, Table 1 and Reference 7), the Apollo SM reaction control engine (No. 5) was selected as the best practical choice for detailed prediction studies, since experimental plume impingement and heat transfer data were available from a test program already completed at the Tullahoma AEDC facility for the Apollo Program. Plumes from other engines were also examined to provide a variety of engine exhaust parameters and results for correlation with predicted results. Jet plume free-flow fields already established for the Saturn S-II cryogenic LO_2/LH_2 engine and the ullage engine were studied, and new jet plume fields were calculated to determine the effects of the different input parameters.

The great number of actual structural components and servicing accessories which might be subject to normal or inadvertent jet impingement precluded consideration of their individual design aspects. The only feasible impingement environments for initial studies, therefore, necessarily were reduced to typical surfaces exposed to the jet plumes. These include flat plates, canted or uncanted, concave and convex surfaces representing the

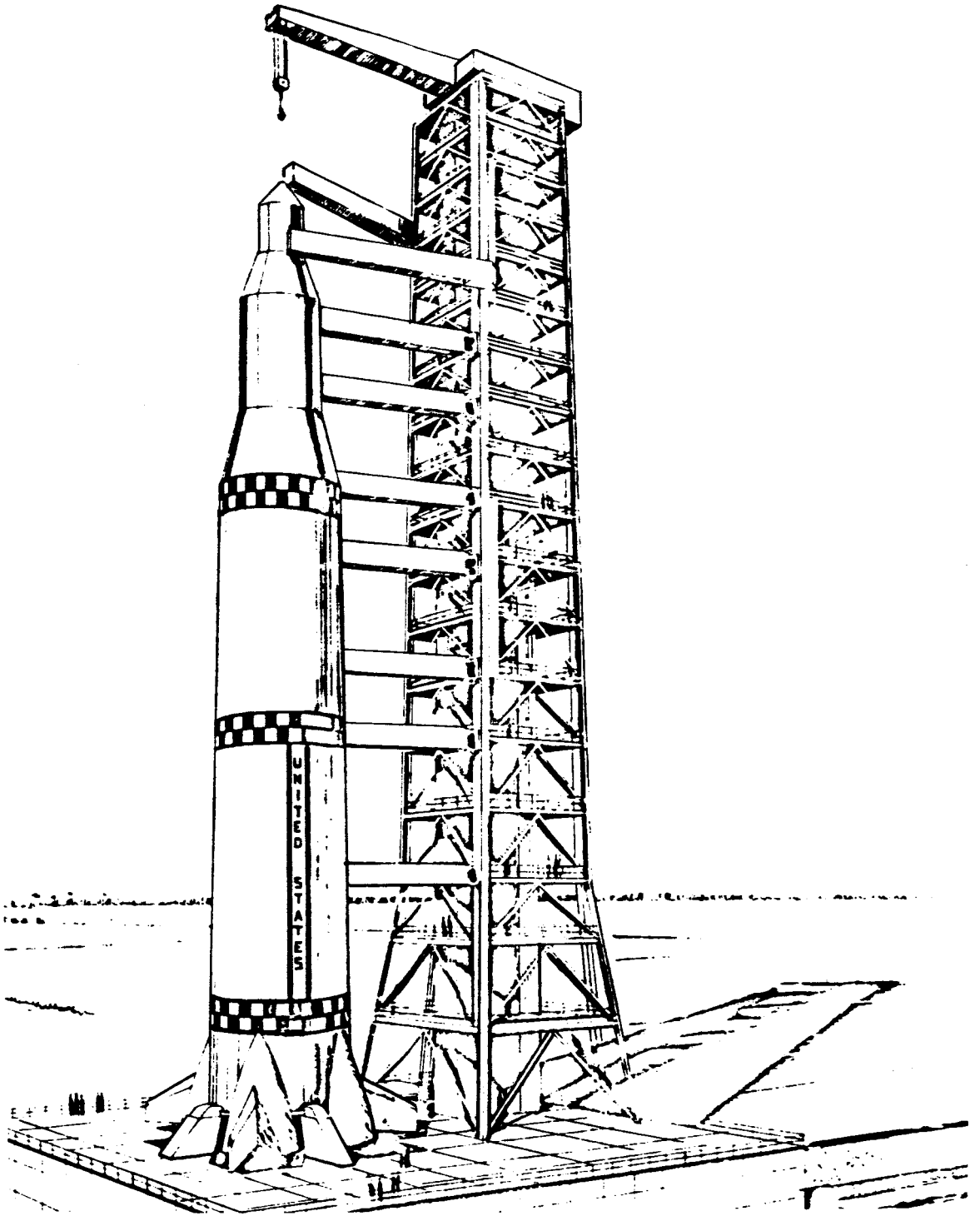

Figure 1. Typical Saturn V Vehicle and Launch Complex Environment

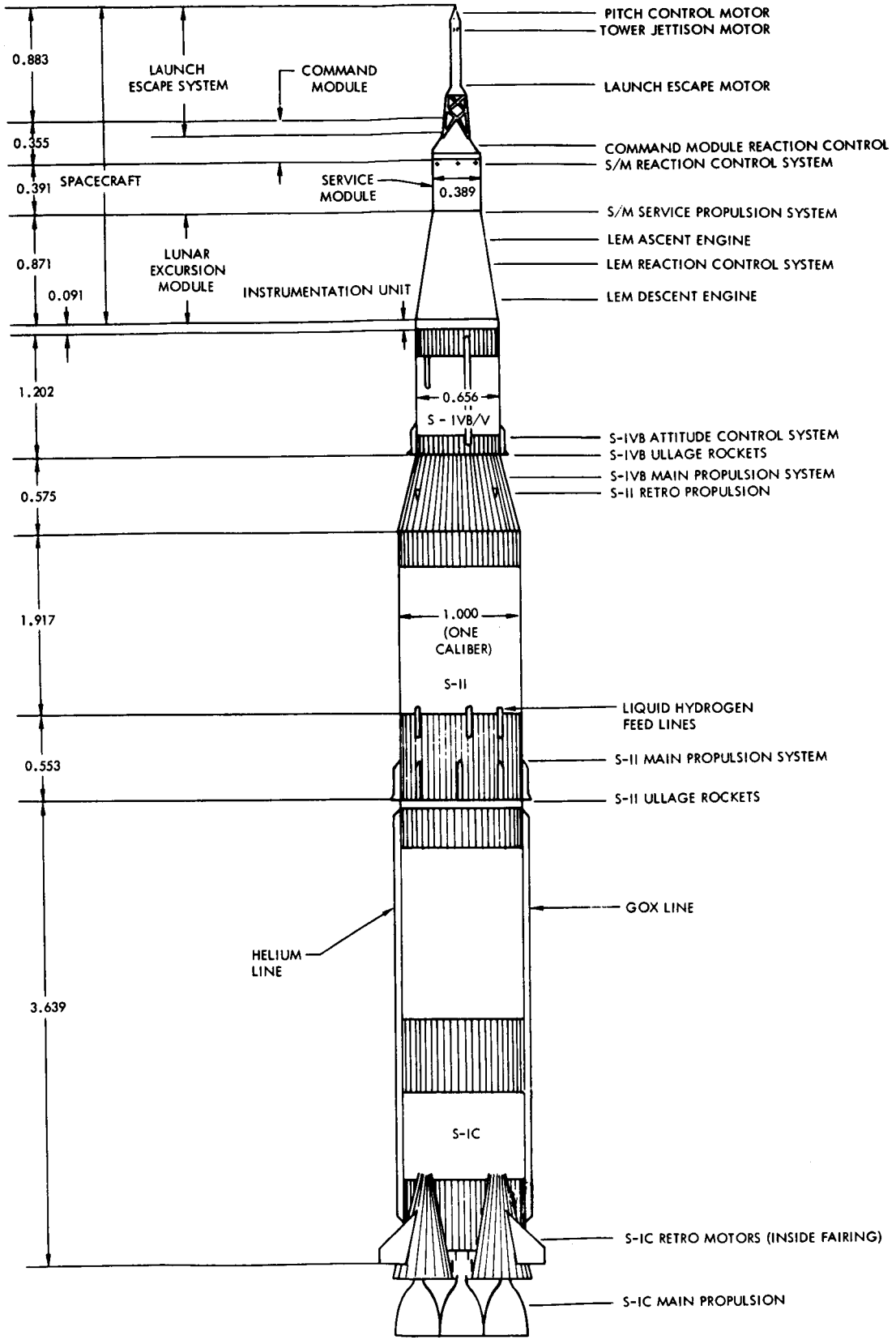

Figure 2. Saturn V Protuberances and Rocket Engine Locations

Table 1. Saturn V Solid and Liquid Propellant Rocket Engine Summary

Category No.	Rocket Engine Name or Function	Type	Propellant Combination	Approximate Thrust (lb ea)	Approximate Burn Time (sec)	Number of Engines
1	Pitch control motor	Solid	Polysulfide ammonium perchlorate	2,200	0.6	1
2	Tower jettison motor	Solid	Polysulfide ammonium perchlorate	31,600	1.0	1
3	Launch escape motor	Solid	Polysulfide ammonium perchlorate	139,400	3.2	1
4	CM reaction control	Liquid	N_2O_4/MMH	100	--	12
5	SM reaction control	Liquid	N_2O_4/50-50*	100	--	16
6	SM service propulsion	Liquid	N_2O_4/50-50*	22,000	--	1
7	LEM ascent engine	Liquid	N_2O_4/50-50*	3,500	--	1
8	LEM descent engine	Liquid	N_2O_4/50-50*	10,500	--	1
9	LEM reaction control	Liquid	N_2O_4/50-50*	100	--	16
10	S-IVB attitude control system	Liquid	N_2O_4/50-50*	150/70	--	6
11	S-IVB ullage rockets	Solid	Polysulfide ammonium perchlorate	3,500	3.9	2
12	S-IVB main propulsion system	Liquid**	LO_2/LH_2	200,000	480	1
13	S-II retro propulsion	Solid	Polysulfide ammonium perchlorate	34,500	1.5	4
14	S-II main propulsion system	Liquid**	LO_2/LH_2	200,000	390	5
15	S-II ullage rockets	Solid	PBAA-A1-AP	22,900	3.7	8
16	S-1C retro motors	Solid	Polysulfide ammonium perchlorate	88,800	1.0	8
17	S-1C main propulsion system	Liquid**	LO_2/RP-1	1,500,000	150	5

*50% UDMH - 50% N_2H_4

**Cryogenic propellant systems; other liquid systems are storable propellants.

interior and exterior surfaces of cylinders, and a hemispherical surface representing the front end of a blunt body immersed in the plume. Degree of severity of the resulting impingement in all cases is a function of the axial location from the nozzle exit plane and the radial distance from the plume axis.

The output of the test-correlated engineering prediction methods, in terms of impingement forces and heat loads to these basic surfaces, provides the designer of the umbilical arms, pipes, cables, hoses and shielding surfaces with the input he needs to proceed with his detailed design. Similarly, the predicted jet plume temperature and heat transfer rates at various distances provides the input needed for determination of any protective measures for personnel in vulnerable areas such as indicated by the example of possible interaction locations in Table 2.

Table 2. Examples of Possible Interaction Locations of External Rocket Engine Plumes With the Umbilical Tower Arms of Complex 39

Arm No.	Approx. Vehicle Station (inch)	Engine	Direction of Jet Plume Centerline
1	3929 3980	Launch escape motor	35° outward from vertical centerline
	3815 3810 3751 3939	CM reaction control	Varies widely
2	3734 3682 3644	SM reaction control	Horizontal and 90° up and down; 10° outward
3	3199	S-IVB retro rockets	Upward and about 15° outward
4	2729 2639 2627	S-II retro propulsion	90° upward

C. ENVIRONMENTS AFTER LAUNCH

The principal environmental change after launch is the decreasing ambient air pressure which decreases logarithmically with increasing flight altitude and results in huge mushrooming jet plumes at the near-vacuum conditions. Early in the launch, the coaxial free air stream and cross-wind effects would not appreciably affect the relatively high-velocity exhaust gases of the main booster engines, although later, at high altitudes, they would. Thus, the jet-plume free-flow field description is required for each operating engine (and for others susceptible to inadvertent firing) at a series of altitudes the pressures of which range from sea level to near-vacuum conditions.

In addition, changes in distances from engines to nearby surfaces occur during normal staging sequences; however, again the basic types of surfaces with ambient pressure, distances, and the engine nozzle exit conditions as the principal plume input variables are the appropriate starting point toward solution of the overall problem. The interaction of the free plume boundary with the wind tunnel air flow data of Reference 7 for the general shapes simulating the actual protuberance shapes would then permit detailed local plume flow fields to be estimated. While such applications are outside the scope of the present study, basic equations for incorporating the Newtonian impact of such air flows on the plume boundary location are presented herein in Section II.

D. SPECIAL PROBLEM AREAS

1. Reverse Exhaust Gas Flow[1]

Although cluster engines do not represent the basic conditions delineated for this study, interest in the pluming phenomena was initially stimulated by this problem and resulted in an extensive test program yielding much applicable data. As indicated in the preceding discussion on environments after launch, in general, an appreciable exhaust-jet air-flow interaction occurs whenever a rocket motor in a moving vehicle exhausts into the atmosphere. The problem is particularly severe in the case of clustered engines at the lower altitudes, and, of course, must be considered for the effects on the exhausts of the various auxiliary solid-propellant launch escape, ullage, and retro rockets at the higher altitudes when the vehicle velocity is also high. For example, the reverse gas flow resulting from mutual impingement of the five J-2 engines in the Saturn S-II stage backs into the protective heat shield below the vehicle base, chokes in the lateral

[1] Based on study contributed by NAA/S&ID Flight Sciences

exit areas between nozzles when ambient pressure is low enough, and vents, (Figure 3) for the four outer engines. In addition to the four principal nozzle design parameters, the important cluster parameters include the pitch or spacing diameters (D_s), the free distance (L) between the nozzle exits and the vehicle base, and the core and side-vent areas. The side view indicates the approximate streamline flow paths and how, at some effective stagnation point a short distance downstream of the nozzle exit, a small fraction of the impinging flow is diverted to flow upstream toward the vehicle base. The flow again changes direction by escaping through the openings between the thrust chamber cylinders.

The plume characteristics for a simulated four-nozzle cluster propulsion system are shown in Figure 4 as a function of altitude. At low altitudes (A), the exhaust plumes expand relatively little, and impingement occurs far downstream of the base, if at all. This produces an aspirating effect in the base region, creating a low pressure on the base and drawing atmospheric air into the base region (negative reverse flow). Additional atmospheric air flows into the base area due to the interference between the external flow and the exhaust jets. In this altitude regime of aspiration (from zero to approximately 50,000 feet) the integration of the base pressure minus freestream pressures over the base area results in a drag force; the base heating due to recirculation of rocket exhaust gases is nonexistent or small compared with the base heating due to afterburning of entrained fuel-rich rocket exhaust gases with atmospheric air.

At intermediate altitudes, increasing from approximately 50,000 feet to the critical altitude, the exhaust plumes greatly expand. The jet impingement point moves nearer the base, and the reverse mass flow due to the impinging jets increases. In the lower part of this intermediate altitude regime, however, the reverse flow is able to escape between the jets before reaching the nozzle exit plane, as shown in Figure 4 (B). Thus, the net base flow is still negative due to the aspiration and external-flow interference effects. Nearing the critical altitude, however, the reverse-flow effect overcomes the aspiration effect, and the effects of external flow become minor; thus the net base flow becomes positive, escaping to the sides between the exhaust nozzles, as shown in Figure 4 (C). In the intermediate altitude regime, from approximately 50,000 feet to the critical altitude, the integration of the base minus freestream pressures over the base area changes from a drag force to a thrust force as the altitude increases; the base heating due to recirculation of rocket exhaust gases increases with altitude; and the base heating due to afterburning is minor in the low part of this regime, becoming nonexistent with increasing altitude. Test results illustrating these phenomena have been published (References 8 through 12).

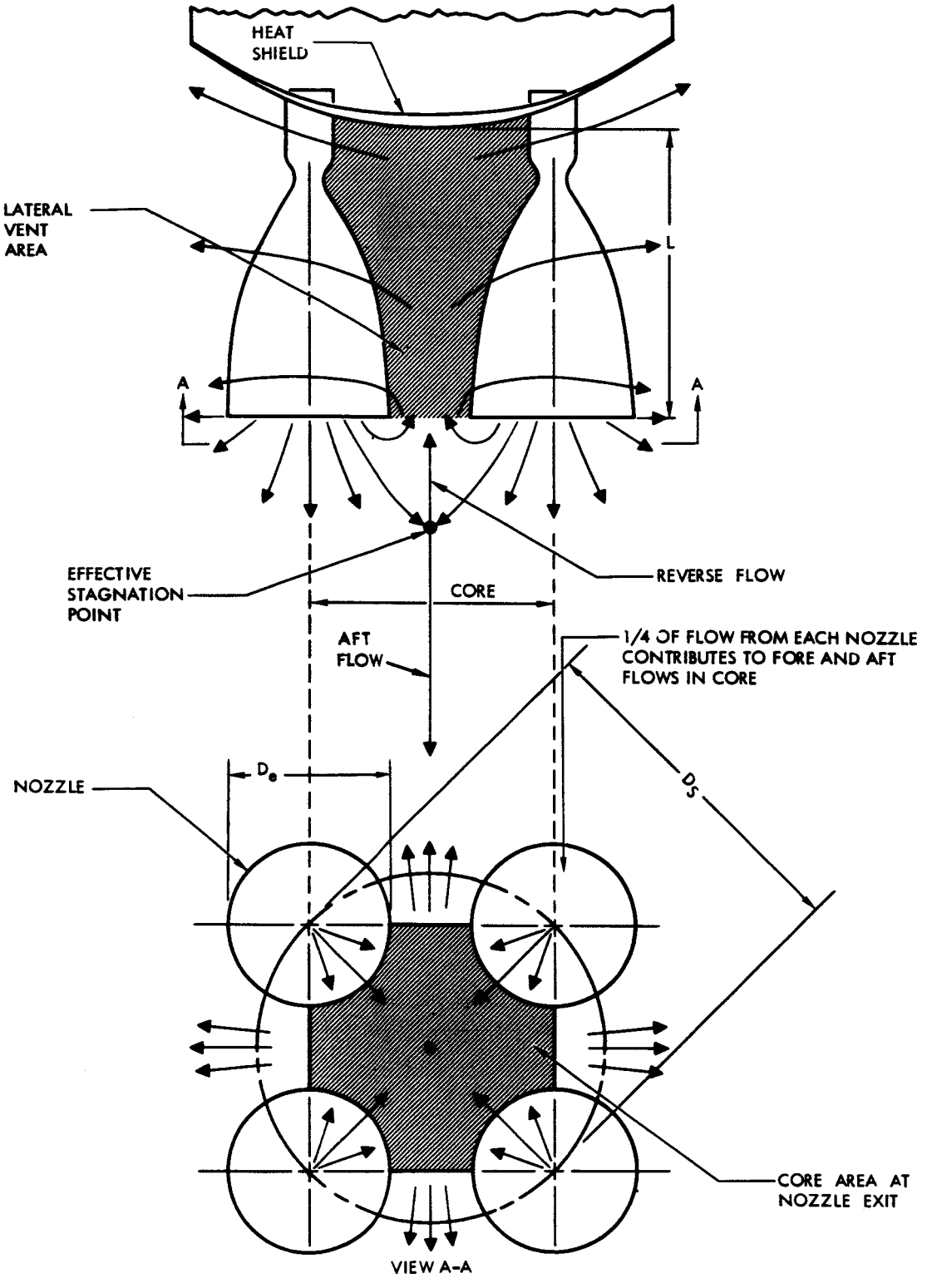

Figure 3. Reverse Flow Problem with Clustered Engines

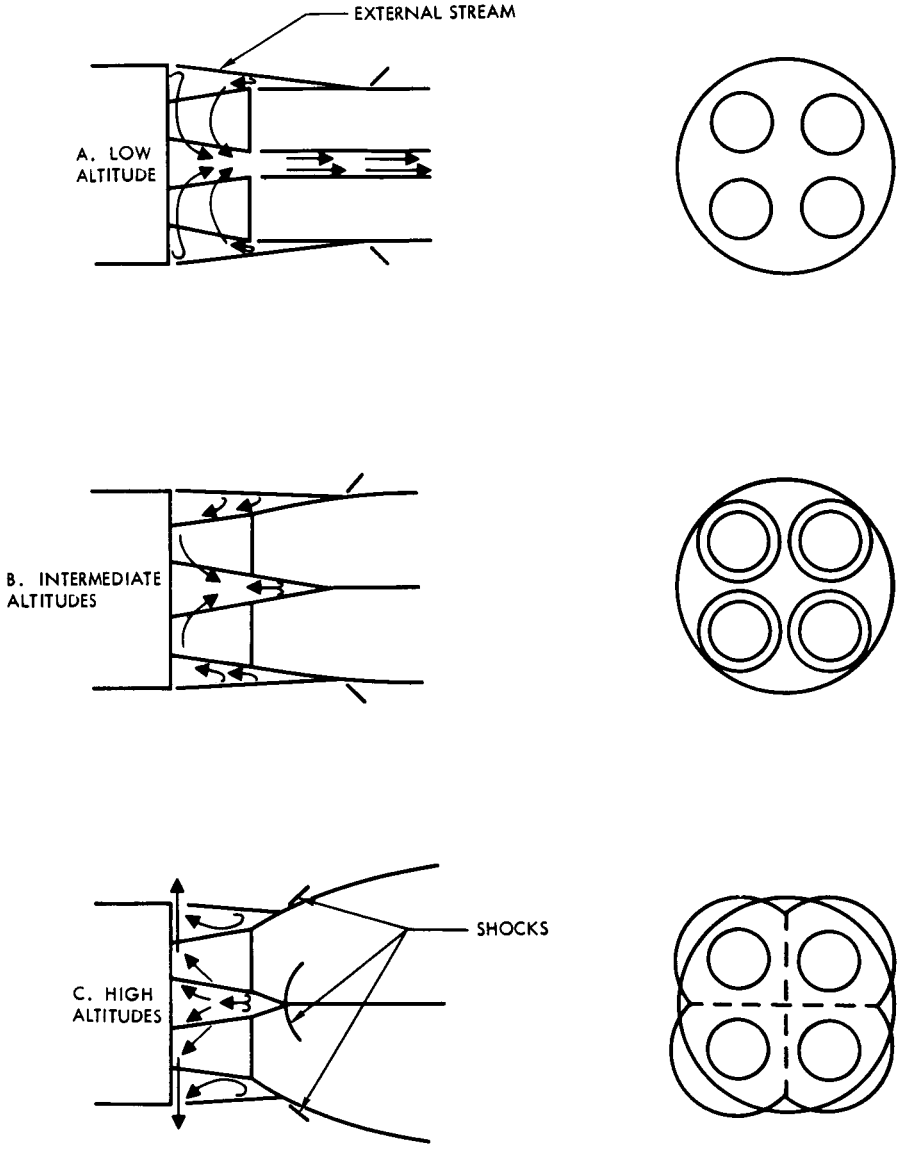

Figure 4. Effects of Altitude on Base Flow

At the critical altitude, the exhaust plumes expand greatly and the reverse mass-flow rate has increased to the point where the lateral escape area between the exhaust nozzle is choked. Test data (Reference 12) indicate that the choking takes place over a finite range in altitude. It appears that choking of the lateral escape area starts in the plane of the base and then grows toward the nozzle exit plane with increasing altitude. The altitude at which the escape areas are completely choked is called the critical altitude. Data from References 8 through 12 indicate the following for a four-engine cluster at altitudes equal to or greater than the critical altitude:

1. The amount of reverse flow at the base is constant.

2. The static pressure at the center of the base is constant.

3. The heating rate at the center of the base is constant.

4. The distribution of static pressure on the base remains constant.

5. The integration of the base minus the freestream pressures over the base area results in a thrust force.

6. The effects of external flow become negligible.

Various hypotheses of the base-flow mechanism, based on test data and fluid dynamic principles, have been developed. For a four-engine base, (Figure 3) Goethert hypothesized (Reference 9) that if the core area is greater than the lateral vent area between the engines, the base flow would choke in the core area and expand supersonically into the base region, forming a normal shock over the base. In both cases, the flow is assumed to choke at the lateral escape areas between the nozzles and expand supersonically into the atmosphere. However, some Saturn S-IV four-engine model test data (Reference 10) were obtained using a pitot probe which was transversed through the base-flow field along the vehicle centerline from the plane of the base to the jet impingement point; these data indicated that, despite the fact that the lateral vent area was greater than the core area, the reverse flow was supersonic before it reached the nozzle exit plane. The Mach number at the nozzle exit plane was about 3. A maximum of about 3.5 was reached about an inch from the model base. The data indicated, therefore, that the flow in the base region will be supersonic regardless of which area is greater.

The probability of theoretically predicting such interaction flow patterns for complex geometrical configurations is remote. Wind-tunnel tests are

required to establish the combined flow velocities and pressures, although an approach could be made by applying the methods of this report to estimate the interaction using the air flow data from wind-tunnel tests with subscale models.

2. Oblique or Scarfed Nozzles

Existing jet plume solutions cover only the axially symmetric nozzles. Frequently the nozzle conical exit or quasi-elliptical exits protrude beyond a desired aerodynamic fairing surface and are cut off by an oblique transverse plane or curved surface to be mounted flush. Two practical expedients to estimate the usually small effect on impingement and heat loads at low altitudes are as follows:

1. Pass a plane through the axis of the nozzle and through the major axis of the elliptical cross-section; combine the two halves of axially symmetric plume flow fields calculated separately for each exit radius at the respective nozzle lip locations; and finally join the displaced but corresponding isomachs by tangent circular or elliptical arcs passed through the plume axis at the axial location of the same Mach number determined from a third calculation of a centrally located plume flow field.

2. Since the centerline of the scarfed nozzle plume must be angularly displaced from the nozzle axis, a correction can be applied to the preceding expedient by estimating the eccentric nozzle wall pressure times area force increments, and summing to obtain a force which, added vectorially to the axial thrust for the symmetrical portion, gives the approximate desired angle of the resultant representing the momentum of the actual plume flow path.

A more serious problem arises at high velocities, particularly in the case of satellite reentry, when small reaction control engine plumes may be whipped up against the outer walls as the impact pressure increases. This is an extreme case of interaction of the freestream flow field with the exhaust gases which merits continued study but was outside the scope of the present investigation. Somewhat related environmental conditions exist in the analogous case of gaseous and liquid fuel injection inside the nozzle to obtain vector control of the thrust. An approach indicated by the experimental data would be to estimate the effect of the back pressure in changing the exit conditions to those of a pseudothroat beyond a critical extreme condition, and proceeding with the expansion under the conditions of the external aerodynamic flow. Initially, of course, at vacuum or near vacuum altitudes, the impact pressures would be slight enough to assume vacuum free flow field plumes to apply.

3. Erosion and Sooting Problems

(a) Erosion

The exhaust from most solid-propellant rocket engines contains a significant fraction of solid particles. As these particles have higher temperatures and velocities, which persist because of a time lag from the normal adiabatic expansion of the molecular gas constituents, they can contribute a large portion of the heat transfer due to impingement. Even the combustion products of liquid propellants which contain carbon in the fuel, the calculated equilibrium composition of which may indicate a completely negligible fraction (10^{-3} to 10^{-4}), may have as high as a one-percent fraction locally because of fuel-rich mixtures near the chamber and nozzle walls due to incomplete injector mixing or introduction of low-mixture ratio turbo-pump exhaust gases into the nozzle for disposal.

The radiation heat-transfer effect of such particles was investigated and is presented in Section V of this report. However, search of the literature revealed only scant references to the sandblast effect from the solid nozzle exhausts which can quickly erode holes in half-inch-thick steel side plates located close to the nozzle exit. No experimental data were found to warrant checking even the cursory preliminary theoretical assumption of transfer of full enthalpy from the particles to the surface material. Present expedients are to use a sufficient thickness of ablating material determined from simulated empirical tests, or to avoid the use of propellants which produce solid particles altogether in critical applications where a temporary jettisonable shield is impractical.

This problem was discussed with personnel of the S&ID Space Sciences Laboratory with experience in shock-tube work on cratering due to meteoric particle impact. Unfortunately, the test data available applied at reentry velocity levels on the order of 20,000 feet per second and higher. Special tests appear feasible for simulating the relatively low rocket exhaust speeds of 5000 to 10,000 feet per second but would have to be made in a special program oriented to the plume impingement problem.

It is of interest to note that in a paper (Reference 13) describing experimental investigation of this related problem area, Maiden and McMillan state that the results of a program planned initially to determine the effect of compressibility of shielding material, ". . . turned out to be of more importance in emphasizing the effects of heating due to the impact process."

(b) Sooting

The Mercury Flight Reports (e.g., Reference 14) mention obscured vision several times. Astronaut Schirra attributed it to debris deposited on

the window when the LES motor was fired and described it as a thin-pinkish streaked film especially noticeable against sunlight. The sooting resulting from low-altitude operation of the jet plumes of the Apollo launch escape tower (Figure 5) is illustrated in Figure 6, which shows the command module after the boilerplate launch escape tower test made at White Sands proving ground. The tower jettison motor normally (no abort) is operated at altitudes above 200,000 feet, where the plumes will envelop both the launch escape tower and the command and service modules. If the tower jettison motor fails to operate, the launch escape motor is used to jettison the LES and the tower from the command module.

The total amount of exhaust products impacting the window can be estimated by considering the total mass impingement flow during the possible exposure time at various points in the separation trajetory. Only a small fraction of this total remains because of continued removal by the scrubbing action of the plume, however the remaining fraction may be excessive. An experimental program is needed to establish the empirical relation of the remaining fraction with the local conditions of the jet plume and impacted surface.

4. Bending of Jet Plumes by Oblique Air Flow

The effect of oblique air flow across a plume was also studied in connection with the boilerplate Apollo launch escape tower tests made at the White Sands proving ground. Figure 7 shows predicted interactions with the air flow at a 25-degree angle of attack for four different times during the firing of the launch escape system solid-propellant motor. The markedly regressive shape of the thrust-time curve shown in the insert in the upper portion of the figure causes corresponding increasing bending as the resisting momentum of the jet exhaust plume steadily decreases. Such predictions can be made from the results of a series of numerical solutions based on the general principles described in this report together with the specific engine characteristic data, physical structure environments, and trajectory of the vehicle.

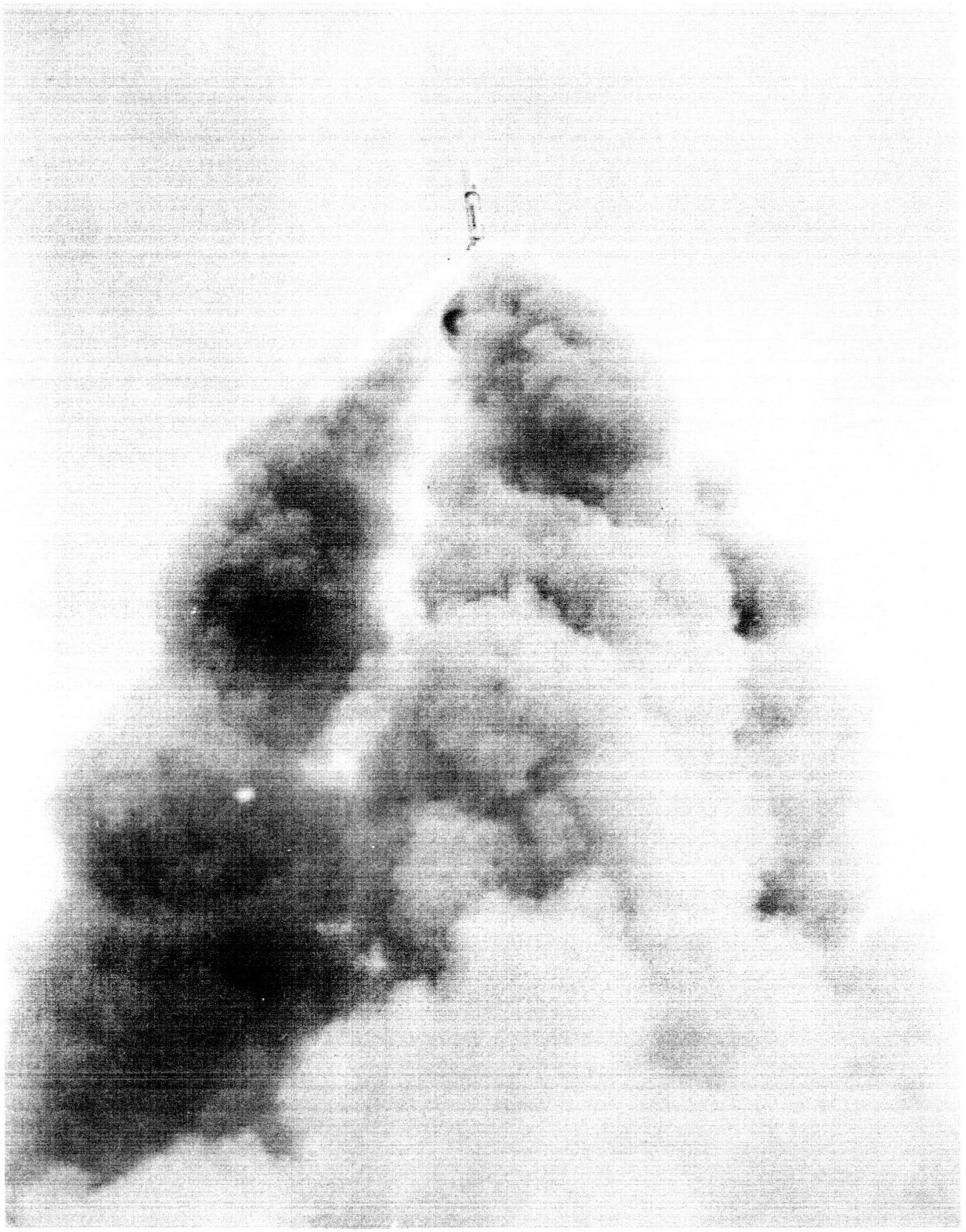

S-63-13889

Figure 5. Jet Plumes from Launch Escape Tower Solid Motor

5-63-13888

Figure 6. Sooting Due to Solid Products in Jet Exhaust

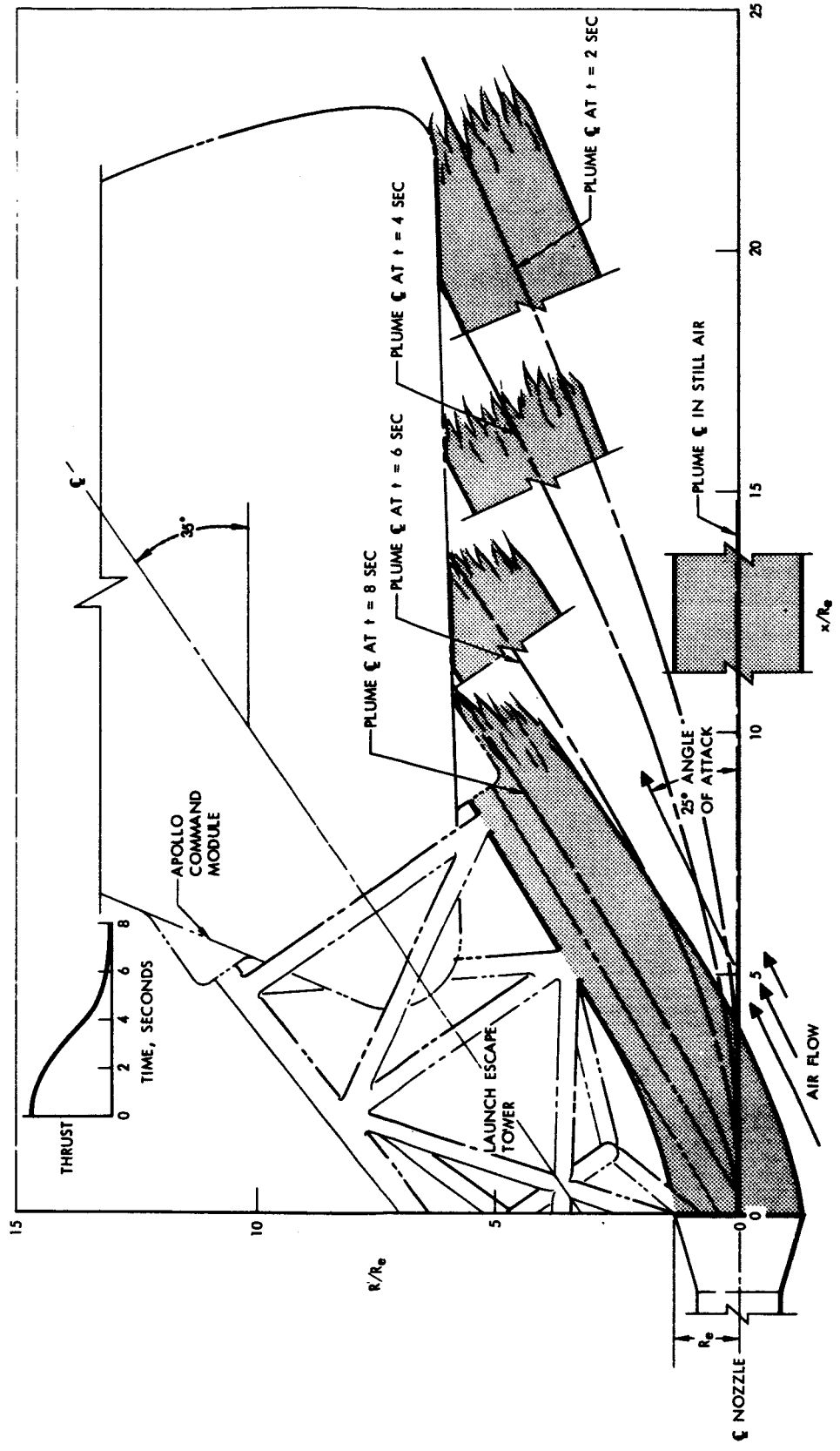

Figure 7. Bending of Jet Plume Due to Cross Air Flow

II. JET PLUME FLOW FIELDS

A. DESCRIPTION OF A JET PLUME

Solution of the variety of problems involved in radiative and convective heat transfer, impingement forces, radar and telemetering signal attenuation, and other effects of jet plumes requires a comprehensive knowledge of the many properties of the plume throughout its flow field. While some of these properties are not yet well established, a proposed standardized target specification for the complete description of a jet plume flow field should include the following parameters in a grid extending as far as may be needed for the solution of the particular problem at hand:

1. The dimensionless radial distance from the nozzle axis; i.e., R/R_e, the ratio, actual distance to the nozzle exit radius, for plumes symmetrical about the nozzle axis

2. The dimensionless axial distance from the nozzle exit plane; i.e., x/R_e, or ratio of actual axial distance to the nozzle exit radius

3. The above point locations to be, preferably, along selected streamlines representing 10, 20, 30, 40, 50, 60, 70, 80, 90, 95 and 99 percent of the enclosed mass flow-rate (assuming each axisymmetric streamline revolved about the nozzle axis)

4. The streamline flow angle, θ, measured with respect to the nozzle axis

5. The local Mach number, M, or ratio of actual velocity to the local velocity of sound of the gas

6. The complete gas composition, including solid particle distribution and temperatures (if different from the mean value in the gas), ratio of specific heats of the gas, specific heat of the solid particles, ionization level, spectral distribution of emmisivity and absorptivity, etc., - all for shifting equilibrium expansion to the local conditions at each point.

Most of the published reports on jet plumes include only a family of constant Mach number or isomach curves plotted on the dimensionless rectangular coordinate system with rather scant additional information on the

detailed gas properties. Much work is needed to meet the above specification of the complete plume description which obviously is beyond the scope of the present program. Nevertheless, in many practical cases the specification approximations have yielded surprisingly good correlation with experimental data.

B. APPROXIMATE JET PLUME METHODS

Until the classic and relatively exact method of characteristics for calculating jet-plume free-flow fields was successfully applied and used by most organizations, various approximate methods were the only recourse. The usual basic simplifications were to assume an ideal gas with "frozen" composition and specific heat ratio, no viscous effects or mixing of the exhaust gases with air along the plume boundary, a nonmoving nozzle or quiescent ambient atmosphere, and empirical relations from test data. Two methods are described in the following sections.

1. Empirical Circular Arc Boundary Method

Latvala's circular arc approximation for the initial plume boundary is a good example of these methods (Reference 14) and an aid in understanding the elements of the plume description problem. Figure 8 shows the geometry of the Latvala method. It is first necessary to calculate the boundary angle, θ_B, that the tangent to the plume at the nozzle lip makes with the axis of the nozzle. This angle is the algebraic sum of three component angles:

$$\theta_B = \theta_a - \theta_e + \theta_N \qquad (1)$$

where

θ_B = net boundary angle sought

θ_a = maximum expansion angle given by the Prandtl-Meyer equation for expansion from Mach 1 to Mach M_B at the boundary or ambient pressure

θ_e = expansion angle from the Prandtl-Meyer equation for expansion from Mach 1 to Mach M_e at the nozzle lip (negative since the capacity to expand to this value would be wholly suppressed by the nozzle wall in an axial exit design),

θ_N = nozzle exit, or half-cone, angle (additive when, as is usually the case, the rocket nozzle exit angle is not zero, since an excess has been subtracted by θ_e in this case).

The equation for the Prandtl-Meyer wave expansion angle is the integral of the differential equation

$$d\theta = \sqrt{M^2-1}\left(\frac{dV}{V}\right) \tag{2}$$

which is the basis of the method-of-characteristics exact solution and determined from the geometry (in the limit) of the two-dimensional flow illustrated in Figure 9. The well-known integration of Equation 2 which may be found, for example, in Reference 15, is:

$$\theta = \sqrt{\frac{k+1}{k-1}}\tan^{-1}\sqrt{\frac{k-1}{k+1}}\sqrt{M^2-1} - \tan^{-1}\sqrt{M^2-1} \tag{3}$$

in which

θ = total angle, in radians, swept out during expansion from Mach 1 to Mach M_a and also to Mach M_e

k = specific heat ratio of the gas c_p/c_v, assumed constant.

The center of the radius of the circular arc lies along a perpendicular to the plume boundary tangent at angle θ_B from the axis. The empirical Latvala radius based on careful examination of the schlieren photographs made during various series of tests with air, and extended to include the effect of different specific heat ratios of other gases, is (Reference 14):

$$R_c = R_e\left[\left(\frac{R_c}{R_e}\right)_{air}\right]\sqrt{\frac{(k+1)\ (5+M_e^2)}{12\left(1+\frac{k-1}{2}M_e^2\right)}} \tag{4}$$

where R_e is the nozzle exit radius, $(R_c/R_e)_{air}$ is the empirical radius ratio as a function of M_e from prior experimental data with air (Table 3), k is the specific heat ratio of the gas, and M_e its Mach number at the nozzle exit lip conditions.

Adamson (Reference 16) states that while circular arc methods such as the above may be a good approximation to the boundary near the nozzle exit, it is difficult to calculate the appropriate average radius of plume curvature, since the maximum jet diameter must be known a priori to extend the good correlation obtained in the initial portion of the jet. An S&ID approach to

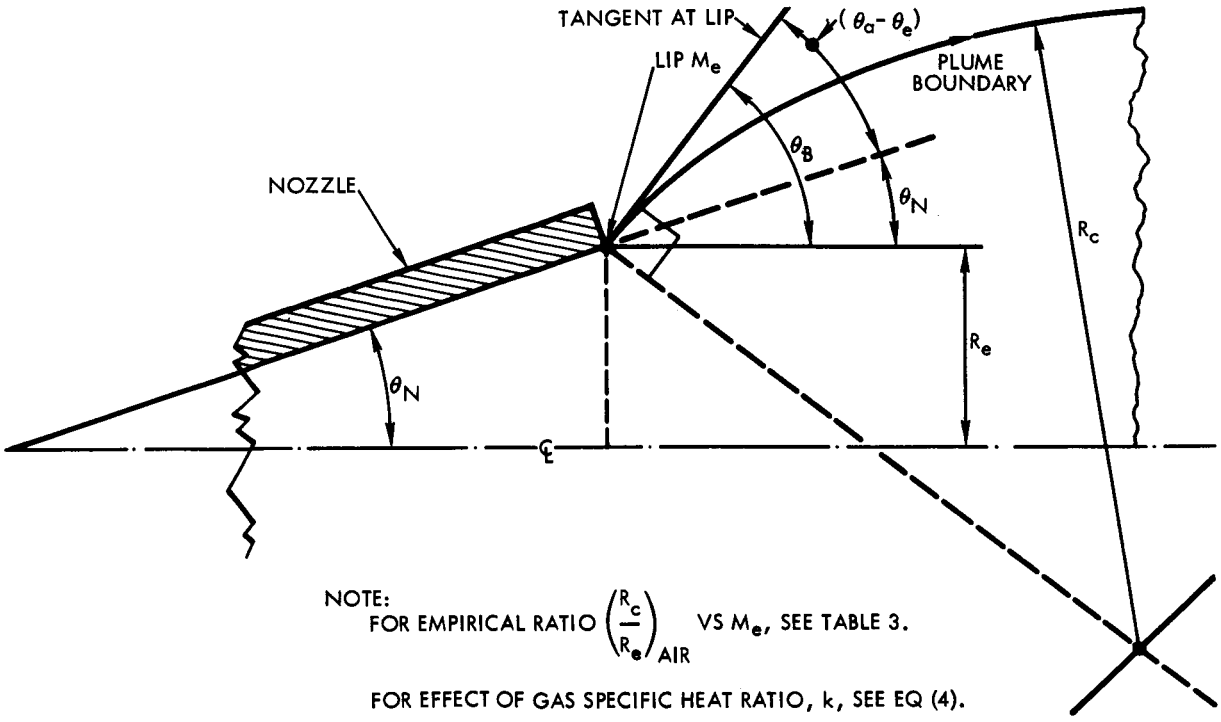

Figure 8. Latvala Circular Arc Jet Boundary Approximation

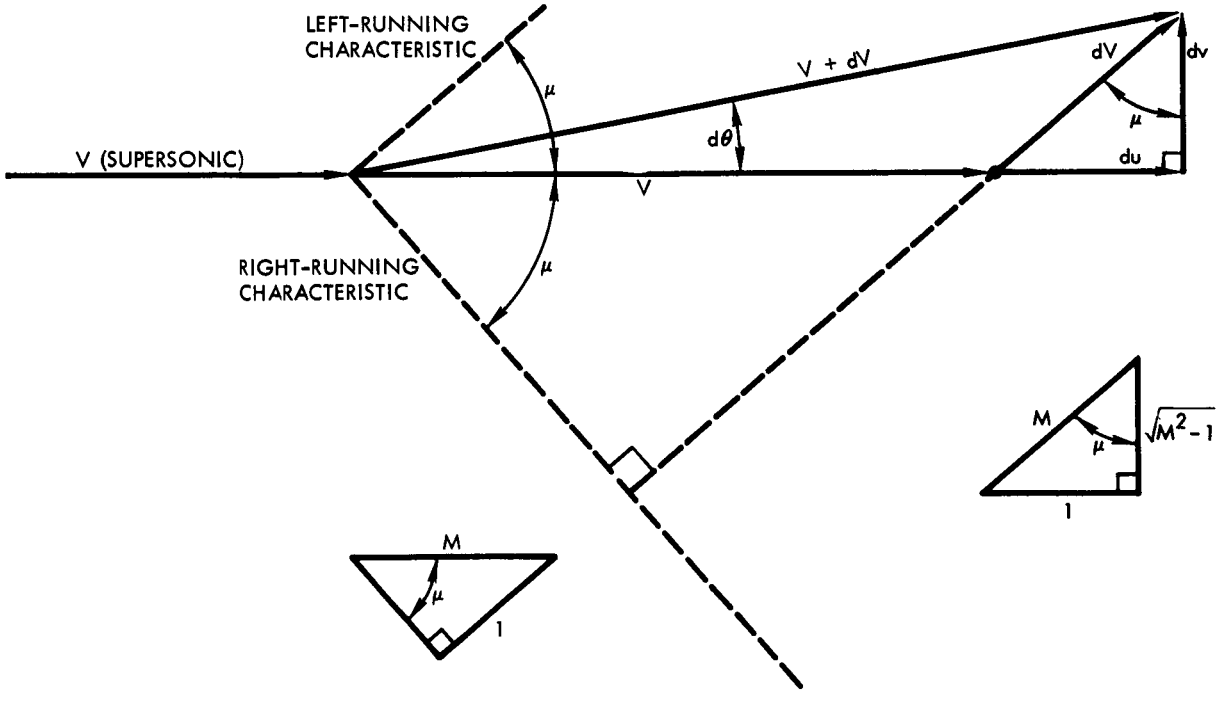

Figure 9. Basic Two-Dimensional Wave Expansion Geometry

Table 3. Latvala Plume Boundary Radius Ratio Versus Nozzle Exit Mach Number for Air

M_e	R_c/R_e	M_e	R_c/R_e
1.0	38.3	3.5	18.4
1.5	28.0	4.0	17.8
2.0	23.1	4.5	17.4
2.5	20.9	5.0	17.1
3.0	19.2	5.5	16.8

determine this average or increasing radius was initially planned for development, but work on it was deferred at NASA-MSFC request to provide available time to include correlation studies with Saturn SA-5 test launch data, using existing plume approximation methods.

2. Empirical Decay-Ratio Method for Sea-Level Jet Plumes

Anderson and Johns review the work of a variety of able investigators who have attempted to develop a satisfactory theory for the mixing of a jet with quiescent air (Reference 17). The theoretical treatment is highly complex, with the decay in the supersonic region greatly complicated by shock and expansion-wave interactions.[1] These authors state that while significant contributions has been made, a satisfactory theoretical description of the flow in this region is practically impossible, and proceed to treat the problem from an experimental and empirical approach which yielded some very useful

[1] The location of the first Mach disc, or Riemann shock distance, was investigated following the technical discussions at Huntsville on January 27-28, 1965 (Reference 18). Study of the results by Love et al. (Reference 19, Page 90) indicate that no Riemann wave occurs for a nozzle-exit Mach Number of about 3.2 and an exit-to-ambient pressure ratio of about 0.64 (values from one-dimensional flow calculation). This appears somewhat unrealistic since a shock must occur, at least starting within the nozzle, to bring the average exit pressure up to ambient pressure at, or shortly downstream of, the nozzle exit. Adamson (Reference 16) emphasizes the inability of the characteristics method solution of the jet plume to predict the first Mach disc, inherently, but describes an empirical method supported by test data for air at $M_e = 2$. Despite the discrepancy in Mach number his graph indicates that the shock location, if it occurs, would be very close to the nozzle exit, thus outside the path of the plume over the SA5-SA6 data points of interest. It will be shown in later sections on impingement pressures and radiation from an impinging shock layer that the approximate sea-level plume method described in this section yields good results.

dimensionless pressure, temperature, and velocity decay-ratio profiles. Typical values of the decay ratios derived from those profiles are shown in Table 4. For convenience, all five sets of ratios (Sections A to E) are compressed into one table to be readily available while making the empirical computations.

Section A of Table 4 shows the impact pressure decay ratio, q_{mx}/q_e, versus the dimensionless axial distance, x/R_e, downstream of the nozzle exit. With the nozzle exit conditions established, the basic impingement or impact pressure on a normal plane can be computed from $p_{I_e} = 2q_e = 2(\rho_e V_e^2/2)$. Thus, the maximum normal impingement pressure along the jet axis, using the empirical decay ratios in Section A of Table 4, is:

$$p_{I_{mx}} = p_{I_e}\left(\frac{q_{mx}}{q_e}\right) \tag{5}$$

Section B of Table 4 shows the empirical dimensionless temperature difference ratio,

$$r_{\Delta T} = (T_{mx} - T_\infty)/(T_e - T_\infty)$$

versus the axial distance, x/R_e. With nozzle exit temperature, T_e, and the (still) atmosphere temperature, T_∞, known, maximum temperature along the jet axis is then:

$$T_{mx} = r_{\Delta T}(T_e - T_\infty) + T_\infty \tag{6}$$

Section C of Table 4 shows the empirical axial subsonic velocity ratio to the sonic velocity (Mach Number 1) at the tip of the "supersonic core or cone" versus the axial increment Δ_x/R_e, beyond the distance x_s/R_e where this occurs. The supersonic cone length is estimated by assuming that the jet pressure is ambient, p_∞, and locating the axial distance, x_s/R_e, from the critical pressure ratio

$$r_{p_{cr}} = p_\infty/p_T = p_\infty/(p_{Ixs} + p_\infty) \tag{7}$$

and its isentropic relation

$$r_{p_{cr}} = \left(\frac{2}{k+1}\right)\left(\frac{k}{k-1}\right) \tag{8}$$

where k = the specific heat ratio, giving practically the same two significant-figure values for a variety of exhaust gases:

k =	1.23	1.26	1.30	1.4 (air)
$r_{p_{cr}}$ =	0.56	0.55	0.55	0.53

Table 4. Empirical Decay Ratio - Properties of Jet Plumes at Sea Level

Section A	
Impact Pressure Ratio q_{mx}/q	Axial Distance Ratio x/R_e
1.00	0
0.99	5
0.98	8
0.95	10
0.90	12
0.80	15
0.70	18
0.60	21
0.50	24
0.40	28
0.30	33
0.20	40
0.15	45
0.10	54
0.08	58
0.06	68
0.04	80
0.03	88
0.02	100

Section B	
Temperature Difference Ratio $\frac{T_{mx} - T_\infty}{T_e - T_\infty}$	Axial Distance Ratio x/R_e
1.00	0
0.99	5
0.97	10
0.95	17
0.90	30
0.85	41
0.80	53
0.75	63
0.70	72
0.60	88
0.50	101
0.40	112

Section C	
Axial Subsonic Velocity Ratio V_{ss}/V_s	Axial Distance Increment Ratio $\Delta x/R_e$
1.00	0
0.90	1
0.80	2
0.70	4
0.60	6
0.50	9
0.40	14
0.30	20
0.20	36
0.10	66
0.09	69
0.08	77

Section D	
Half-Axial Velocity Radius	
x/R_e	R_o/R_e
10	0.5
15	0.8
20	1.0
30	1.5
40	2.0
50	2.6
60	3.2
70	3.8
80	4.5
90	5.1
100	5.8

Section E			
Radial Decay Ratios for q, V, & T	Radial Ratios		
	R/R_o for q/q_{mx}	R/R_o for V/V_{mx}	R/R_o for $\frac{T_R - T_\infty}{T_{mx} - T_\infty}$
1.00	0	0	0
0.99	0.15	0.15	0.15
0.95	0.24	0.25	0.29
0.90	0.32	0.34	0.40
0.80	0.45	0.50	0.60
0.70	0.57	0.66	0.77
0.60	0.70	0.85	0.93
0.50	0.75	1.00	1.12
0.40	0.85	1.17	1.30
0.30	1.00	1.36	1.52
0.20	1.20	1.60	1.80
0.10	1.45	1.95	2.15
0.05	1.75	2.25	2.40
0.04	1.82	2.37	2.46
0.03	1.91	2.50	2.50

The sonic velocity is obtained from the familiar relation

$$V_s = \sqrt{g_o \, kR_g \, T_{xs}} \tag{9}$$

which raises the need for estimating the variation of the gas constant, R_g, along the axis from a consideration of the varying molecular weight. Fortunately, this is also a slow-moving variable with the asymptotic value of 29 for 100 percent air. The empirical axial subsonic velocity, using r_{vs} for the tabular ratio, is then

$$V_{ss} = r_{vs} \, V_s \tag{10}$$

Section D of Table 4 shows the radial radius ratio, R_o/R_e, at which the velocity along a streamline is half of the maximum value existing along the jet axis. These values furnish the empirical distribution basis for estimating the radial decay-ratios of impact pressure, velocity, and temperature difference shown in Section E of Table 4 at particular locations in the transverse planes of the plume. For example, to find the velocity decay-ratio for a point located $R/R_e = 2$ from the plume axis when the maximum velocity in the transverse plane has already been determined, first find the reference R_o/R_e value from Section D of Table 4 at the x/R_e location, then the desired ratio can be located in Section E of Table 4 when the listed radial ratio R/R_o satisfies the relation $(R_o/R_e)\,(R/R_o) = 2$. The radial impact pressure and temperature difference ratios are found in a similar manner using simple interpolation as necessary.

In accordance with the request for a theoretical analysis of two data points of the Saturn SA-5/SA-6 launch test data submitted by NASA-MSFC (Reference 20), the approximate properties of a single booster engine plume at sea level were calculated in the above manner. Figure 10 shows the results used in following sections of the present report for this analysis. Static pressure throughout the plume was assumed to be equal to ambient at sea level. The assumption proved to be adequate since the resulting impingement pressure correlation discussed in the next section is remarkably good. It is believed that similar tables of axial and radial plume property ratios can be developed for the higher-altitude plumes to reduce the time and cost of calculating a new plume each time some minor parameters are changed from a few basic engine- and altitude-input conditions.

C. METHOD OF CHARACTERISTICS

Shapiro (Reference 15) and other authors describe the method of characteristics in detail and, therefore, only notes covering its application at S&ID will be reported here. In general, due to the complexity of the problem, a numerical solution must be used, with accuracy of the results depending on

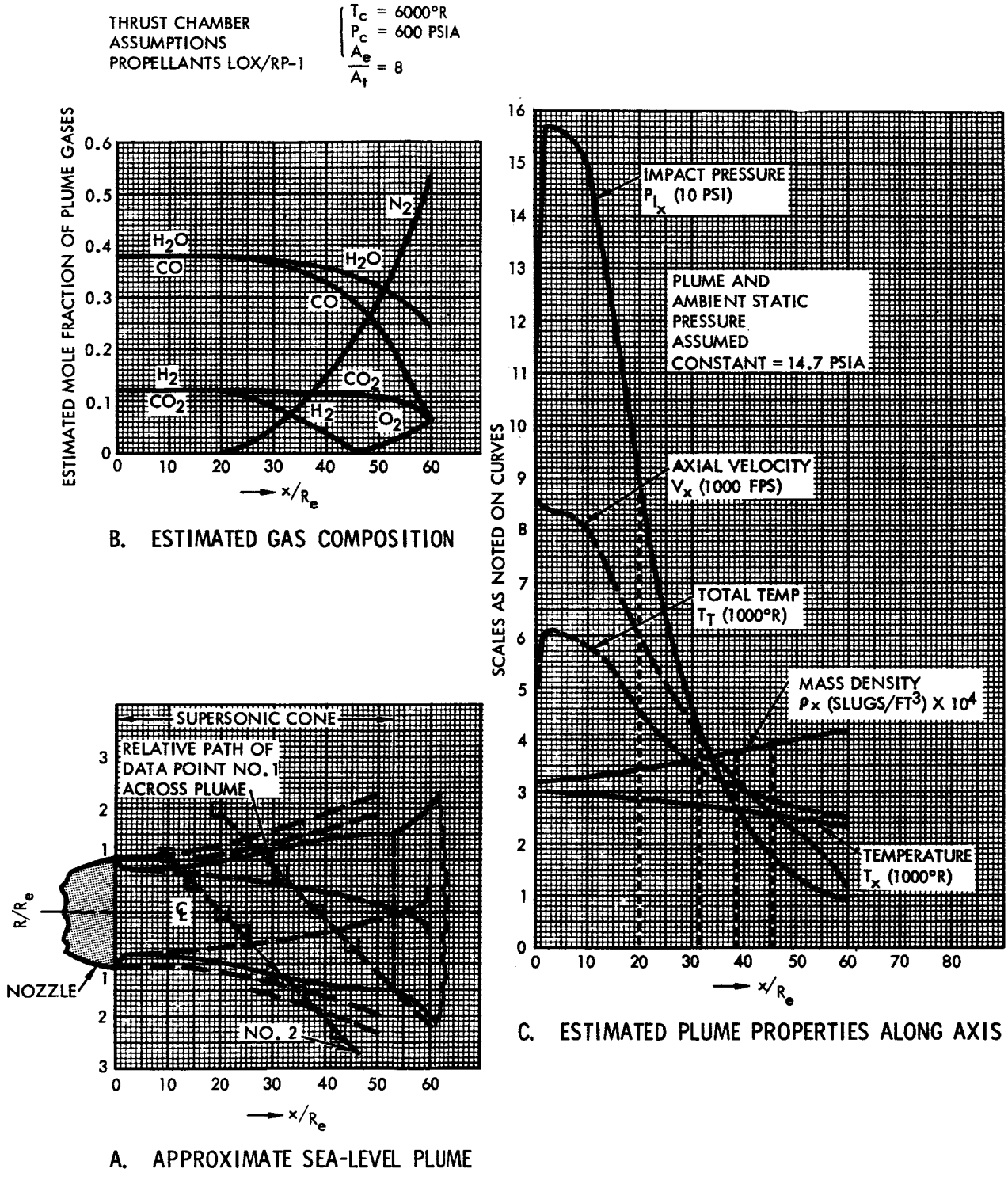

Figure 10. Sea-Level Jet Plume Properties Along Axis by Decay-Ratio Method

the fineness of the steps, or mesh size, during which streamline velocity, direction, pressure, and other related properties may be assumed constant for the simultaneous solutions of the various relations.

Several IBM-7090 programs, with increasing accuracy and flexibility in handling special inputs, have been developed at S&ID in connection with requirements of the Apollo and Saturn S-II programs. Several subroutines also have been developed to simplify handling and analysis of the results. These programs and some of the subroutines are described in the following sections.

1. Saturn S-II IBM Jet Plume Programs[1]

Several progressively improved IBM-7090 computer programs were formulated during the prior Saturn S-II work in this area. The earlier Program Numbers 7N-200 and 7N-210 will not be used in future studies due to development of Program Number 7N-213 which was made available for studies in connection with the present investigation.

(a) Program Number 7N-200.

Based on material from outside sources (Reference 21), this program utilizes the method of characteristics for describing the flow of exhaust gas from conical and parallel flow nozzles. The program has been successfully used at S&ID since late 1962 for several cases and has aided in the prediction of experimental impingement pressure measurements. The program input data include the Mach number at the nozzle lip, the ratio of specific heats, ratio of nozzle-lip pressure to total chamber gas pressure, ratio of gas density at the nozzle lip to total gas density, ratio of ambient pressure to total chamber-gas pressure, and divergence angle of the nozzle. The program assumes radial flow at the nozzle exit and constructs a spherical surface through the nozzle lip, which is assumed to define constant properties for Mach number, pressure, density, and specific heat ratio. The two-dimensional view of this surface for the axisymmetrical jet plume serves as the basic starting line for the method of characteristics calculations.

After defining a Prandtl-Meyer expansion fan at the nozzle lip, as shown in Figure 11, based on a ratio of p_∞ / p_L and the flow angle before expansion, the program constructs left-running characteristics between the starting line and the plume boundary, utilizing the method of characteristics-flow equations in finite difference form.

---

[1] Descriptions of the Saturn S-II jet plume programs together with results of prior calculated plumes, in addition to those for special new plumes calculated to show the effect of shifting instead of constant specific heat ratio, were supplied to Power and Environmental Systems by R.J. Hoffman.

A method of obtaining the location and flow properties downstream of an approximated boundary shock formed by the coalescence of reflected compression waves (right-running characteristics) from the boundary is included in the calculation along the left-running characteristics. This method yields a solution for the position of the boundary shock slightly farther from the nozzle axis than a more exact shock solution.

The calculations are continued until either the required flow field has been computed or the calculations are stopped by the encounter of a Riemann wave and consequent subsonic flow.

(b) Program Number 7N-210

This program is also a method of characteristics, obtained from NASA-MSFC in early 1962, and has been in use at S&ID since 1962. The program has been successfully used for supersonic nozzle plumes for both conical and contoured nozzles. The required input to this program is the right-running characteristic emanating from the lip of the nozzle. To obtain this characteristic, a nozzle-flow program was used based on Program Numbers 7N-201, 7N-202, 7N-203, and 7N-204, obtained from the Rocketdyne Division. This program is in three principal parts. First, it calculates the kernel flow between a slightly supersonic line at the nozzle throat and the right-running characteristic emanating from the tangency point of the throat wall curvature and the nozzle contour, as illustrated in Figure 12. Using the right-running characteristic from the tangency point as input to the second part of this program, the left-running characteristics from the bell analysis are constructed between the kernel line input and the nozzle wall, the last characteristic being the one ending at the nozzle lip. Part three of this program computes the flow along right-running characteristics, using the left-running characteristic to the lip as input. The last line computed by this program (exit flow) is the right-running characteristic emanating from the nozzle lip, as illustrated in Figure 12. This line is the input to the NASA Program Number 7N-213.

(c) Program Number 7N-213

This Method of Characteristics Rocket Exhaust Plume Analysis Program was developed by the S&ID Saturn project to analyze the exhaust plume of an underexpanded nozzle flow (Reference 22). Essentially, the basic mechanics follow the NASA-MSFC Program Number 7N-210; however, many improvements have been incorporated. The program has been checked out for both conical and contoured nozzles and for design to near-vacuum ambient pressures (10^{-10} psia).

Since the output of plume analysis programs would require a prohibitive amount of space to report in detail, an attempt has been made to summarize

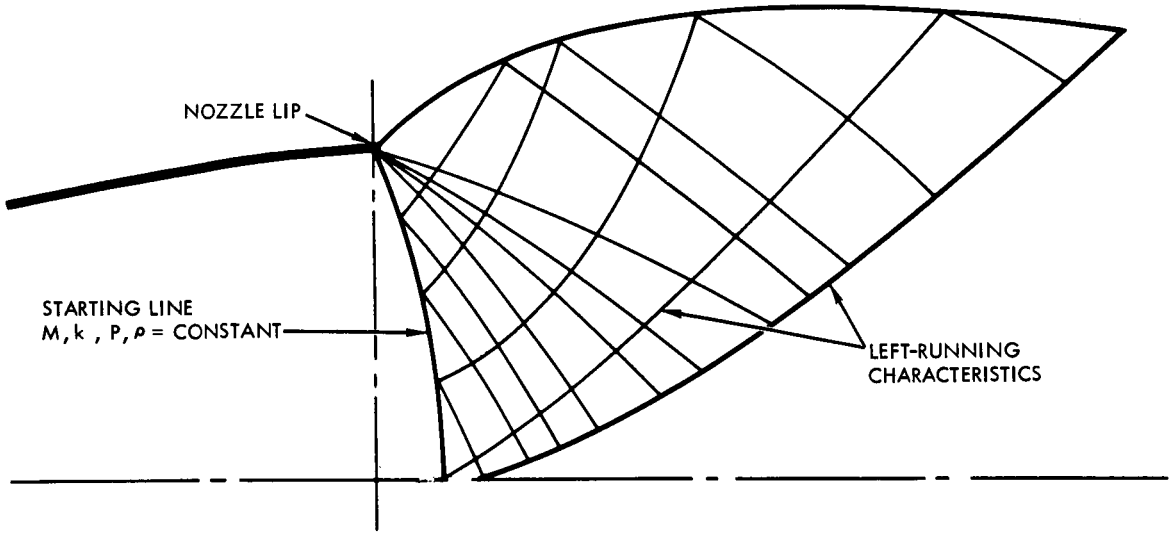

Figure 11. Prandtl-Meyer Expansion Fan for No. 7N-200

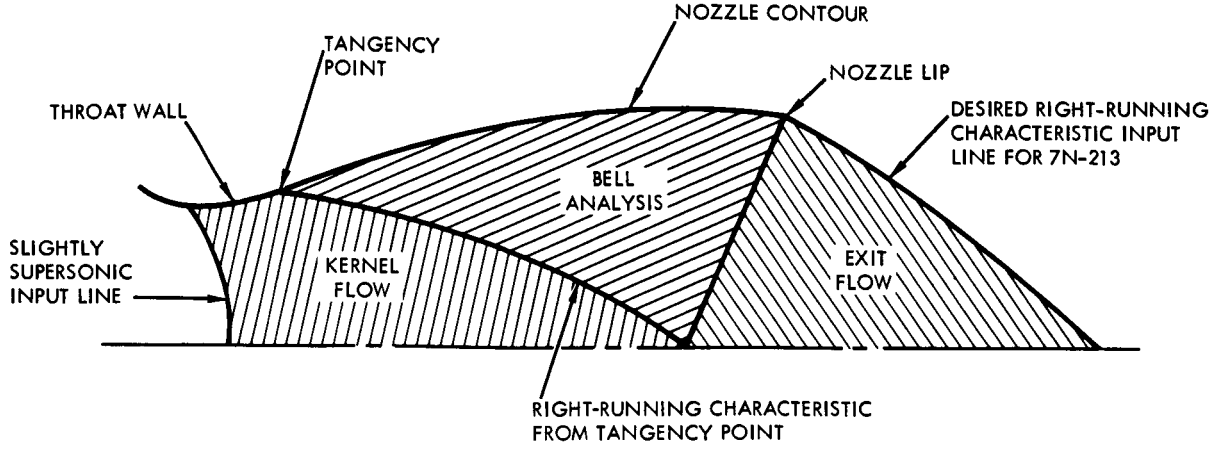

Figure 12. Method of Characteristics in Three Subprograms

the results already obtained from running this program at various altitudes and other conditions. Figure 13 shows a sample of a graphical type of condensed plume as a family of constant Mach curves and another family of constant streamline flow angle curves. Another way (shown in Table 5) to present the condensed plume is as a group of related Mach numbers and flow angles along the dimensionless radial distance for each of a series of selected downstream planes. These condensed plume descriptions are useful for hand calculations that might be needed in applying a general engineering prediction method to a specific force or heat transfer problem which is outside the scope of available subprograms. They can also be useful for interpolation between the assumed conditions of the program outputs. A similar attempt to reduce the information from a large number of plumes to usable proportions may be found in Reference 19, which contains many good schlieren photographs of jets exhausting into still air and into supersonic streams. Study of these photographs helps gain insight into plume problems.

(d) Effect of Gamma

Since the specific heat ratio, k or γ (gamma) is the only variable that presently relates the plume to the chemical properties of the propellant combustion products, further investigation of its effect on the actual jet plume free-flow fields appeared worthwhile. Even if the exhaust gases are completely inert or unreactive chemically, a variation in gamma still occurs as an increasing function of the decreasing temperature (principally) and pressure. Due to the complexity of the method of characteristics solution, it has been the usual practice to assume some "effective" gas specific heat ratio at the nozzle exit plane, or nozzle lip (e.g., 1.25 to 1.30) and keep this constant for the plume calculation. This increased value provided a marked improvement in the shape and location of the plume boundary over the earlier poor assumption that the very low combustion-chamber equilibrium value remained constant throughout the expansion in the nozzle and in the plume. However, since the specific heat ratio of all rocket propellant exhaust gases continues to increase as the expanding gas temperature decreases, even though the gas composition may effectively become "frozen" shortly downstream of the nozzle throat, some uncertainty remained as to the error involved by the use of the constant nozzle exit or lip value.

To determine the extent of the error involved in present general use of a constant, albeit nozzle exit-adjusted gamma, the following IBM runs were made with Program Number 7N-213 using a tabulated input of gammas versus Mach numbers and pressure;

1. Shifting gamma, with chemical equilibrium expansion
2. Shifting gamma, with frozen chamber composition expansion
3. Shifting gamma, as in (1), except for use of a frozen composition at some designated "freezing point" during the plume expansion.

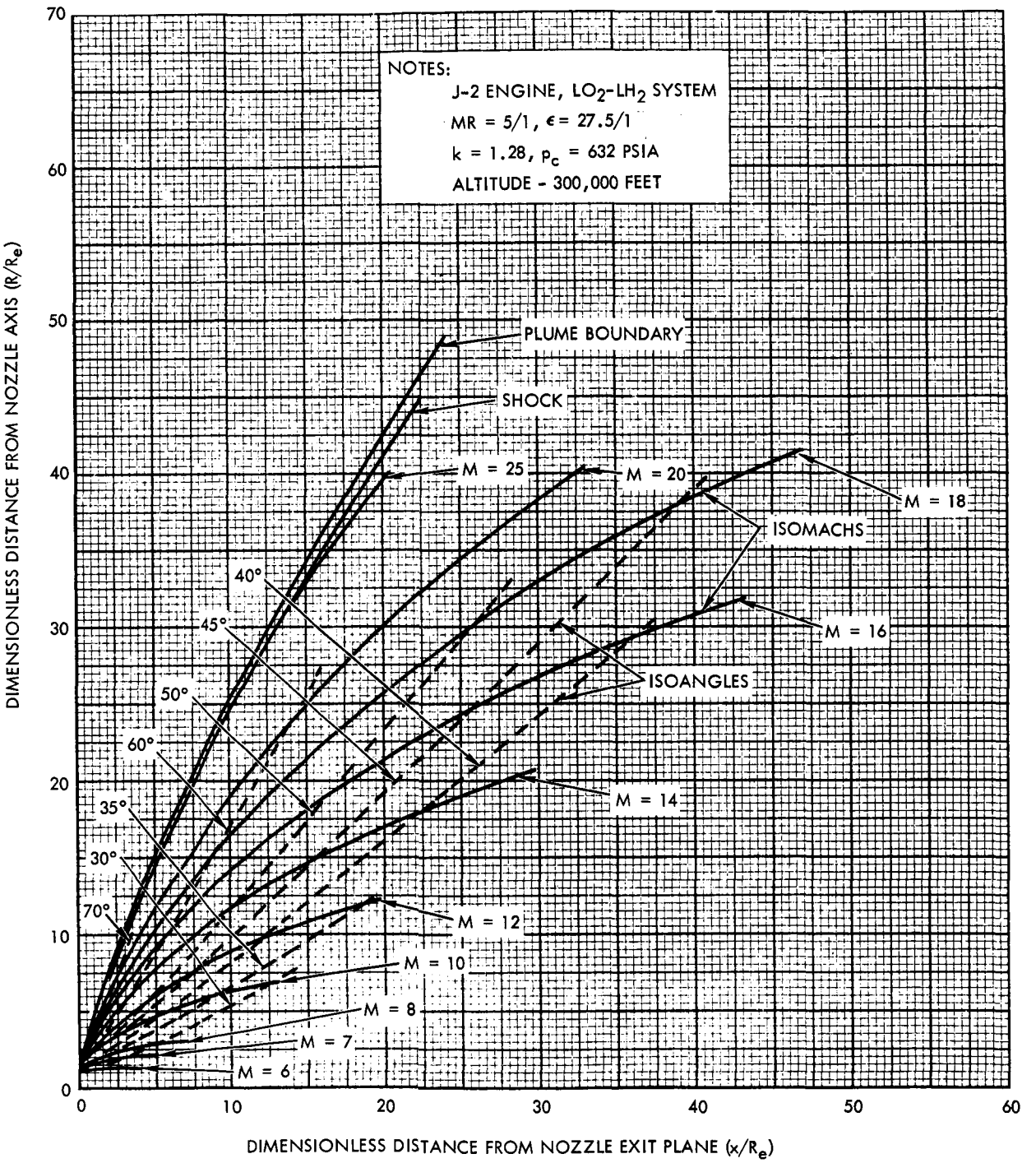

Figure 13. Sample of Graphical Condensed Jet Plume Flow Field

Table 5. Example of Tabulated Condensed Jet Plume Free Flow Field (Listing M and θ in a Series of x/R_e Planes)*

x/R_e	R/R_e	M	θ (degrees)	x/R_e	R/R_e	M	θ (degrees)
1	3.0	12.5	62.5	12	17.0	17.0	52.0
	2.0	9.2	51.0		15.0	15.4	52.0
	1.5	6.6	35.4		10.0	12.0	40.4
	0.8	4.2	0		6.2	9.7	28.3
2	4.8	12.2	58.8	14	20.0	12.1	46.4
	3.5	11.5	56.0		15.0	14.5	48.0
	2.0	7.1	34.0		10.0	11.6	36.6
	1.0	5.1	9.5		8.0	10.5	31.2
3	6.4	12.2	56.7	16	22.0	12.1	45.1
	4.0	10.8	50.6		20.7	17.0	53.5
	2.0	6.8	26.1		15.0	14.0	44.5
	1.0	5.3	9.0		10.0	11.3	33.2
4	7.8	12.2	55.0	18	24.0	12.1	44.0
	4.0	9.6	42.5		20.0	15.9	49.2
	2.0	6.7	21.1		15.0	13.5	41.3
	1.4	6.0	14.2		10.5	11.4	31.7
6	10.5	12.2	52.6	20	26.0	12.0	43.0
	8.0	13.2	53.1		20.0	15.4	46.4
	4.0	8.7	31.8		15.0	13.1	38.0
	2.5	7.3	21.4		12.0	11.8	32.5
8	13.0	12.2	50.0	25	30.3	12.2	40.7
	10.0	13.8	52.0		25.0	16.2	46.1
	6.0	10.1	36.9		20.0	14.4	39.9
	3.5	8.0	24.0		16.0	12.9	34.0
10	15.3	12.0	49.0	30	34.5	12.2	38.7
	15.0	11.7	49.7		30.0	17.0	46.1
	10.0	12.7	45.5		25.0	15.5	41.0
	5.0	9.1	27.2		20.0	13.9	35.2

*For J-2 engine at 200,000-foot altitude with LO_2/LH_2, O/F = 5/1; ϵ = 27.5/1; k = 1.28, $p_T/p_\infty = 1.3 \times 10^6$; and p_T/p_{Lip} = 118.2

A control run using a constant average nozzle exit gamma of 1.28 was also made for evaluation of the effects. The Saturn S-II J-2 engine with LO_2/LH_2 at 200,000-foot altitude was used for all four cases, with the assumptions of a still atmosphere and inviscid flow. The right-running characteristic from the nozzle lip to the nozzle axis, with the corresponding varying specific heat ratio values required as input for the determination of the improved plume, was obtained, in part, from the previously described Rocketdyne Kernel and Bell Analysis Program (S&ID Program Number 7N-202) developed for this purpose for conical nozzles. For the J-2 engines of Saturn S-II, only a partial starting line was obtained by use of this program which does not handle the internal shocks occurring in sharply contoured nozzles. This right-running characteristic was computed for the following assumed conditions; ratio of specific heat constants at 1.23, nozzle area ratio, 27.45, J-2 contour, chamber pressure, 632 psia, ratio of radius of curvature at throat-to-throat radius, 0.392.

The first two cases utilized equilibrium composition properties and frozen chamber composition properties computed by a program obtained from NASA-Lewis (S&ID Program Number 7N-219). The "freezing point" analysis was obtained from a Rocketdyne program similar to the NASA-Lewis program, but with the added refinement of allowing the composition to shift until predetermined "freezing point" criteria are satisfied, and then freezing the composition as the expansion continues. Some extrapolation below 200 K was necessary in all cases.

Figure 14 shows the resulting plume boundaries for the three assumed conditions of shifting specific heat ratio, and for comparison, the corresponding boundary based on a constant value of 1.28. The results show an apparently appreciable displacement of the constant specific ratio plume boundary from the other three boundaries which practically coincide. However, the effects of displacements on impingement pressure and heat transfer from the tenuous gas exhaust at 200,000-foot altitude may be negligible. Therefore, additional composites are included in Figure 14 of the inner Mach 9 and 6 isomachs. These are close enough together to indicate that the impingement errors due to assumption of a constant effective specific heat ratio might be negligibly small.

The constant value of 1.28 is representative of the average specific heat ratio for the J-2 LO_2/LH_2 engine nozzle with its 27.5 area expansion ratio. Lower values of the order of 1.23 and 1.25 would be typical for lower expansion ratios, e.g., of booster engines, and for $LO_2/RP-1$, or solid propellants, while 1.32 has been used for computing plumes for the very high expansion ratio of 40 in the Apollo SM-RCS engine with storable $N_2O_4/50\%\ N_2H_4$-50% UDMH propellants.

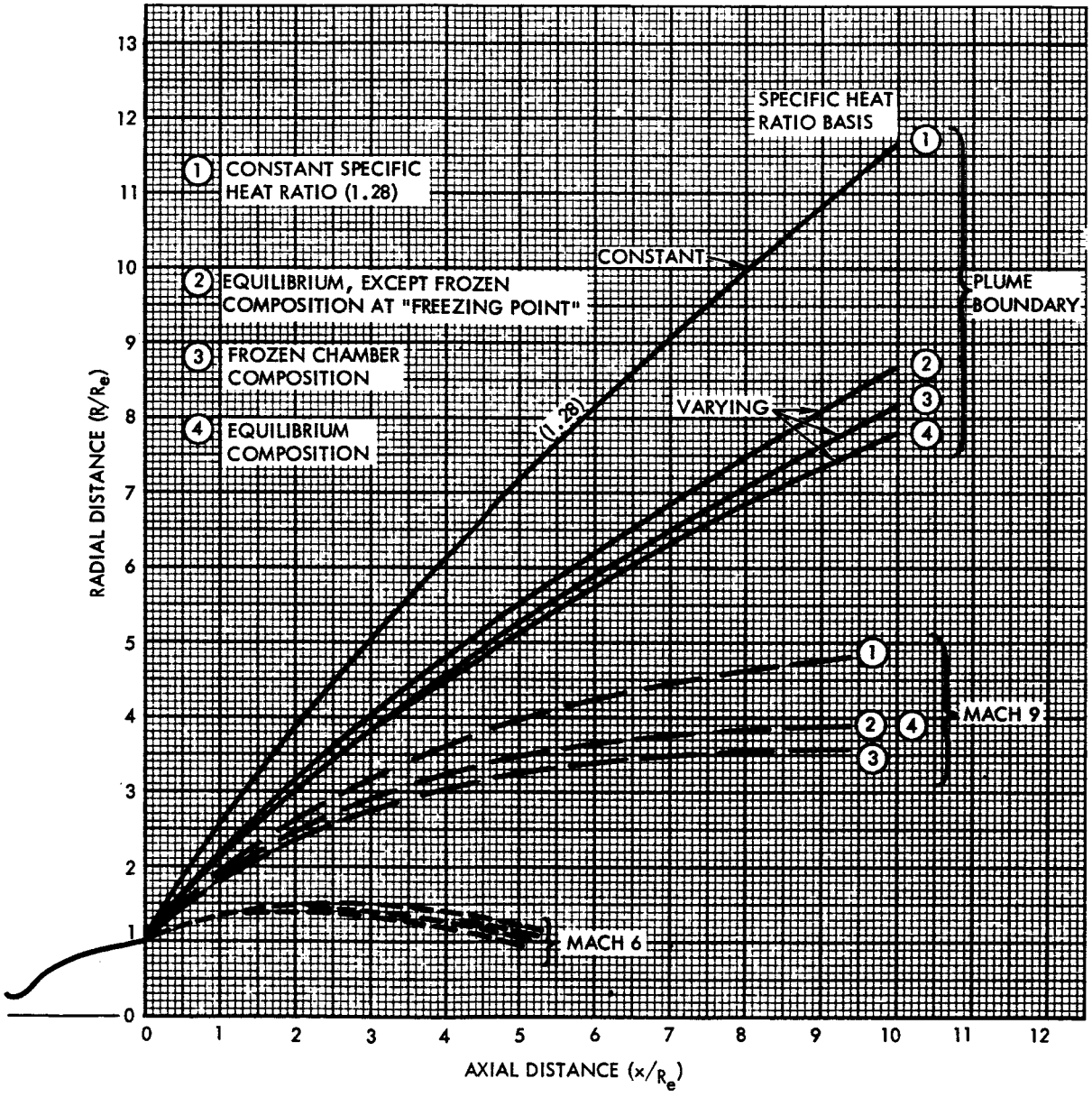

Figure 14. Effect of Constant Versus Varying Specific Heat Ratio on Jet Plume Boundary and Isomach Lines

Considering the above results together with the possibly far greater effect of the freestream Mach Number on the free-flow field jet plume (discussed in the next section), it appears that modification of plume programs to obtain the slight increase in accuracy with the shifting specific heat ratio may not be presently justified, although for high altitudes and for long plume firing durations, some special cases may benefit from, or even require its use.

2. Apollo IBM Jet Plume Programs

(a) Program Number AP-214

Program Number AP-214 was the basic deck used in the prior Apollo work for determination of a free-flow field jet plume in still air from the nozzle design altitude to near-vacuum altitude conditions. A subroutine for the determination of streamlines in the flow field of the exhaust was formulated.[1] This subroutine is dependent upon the knowledge of the flow field along the left-running characteristic emanating from the nozzle-exit spherical boundary for conical nozzles, and from the exit plane, for bell-shaped nozzles. The input utilizes the nozzle exit flow field, flow properties of the gases (ratio of specific heats), and the total-to-ambient pressure ratio. The output consists of streamlines, isomach lines, properties across the plume boundary shock, and position. The stream functions are nondimensionalized relative to mass-flow rate, by having each streamline represent a certain fraction of the total mass-flow rate. Thus, integration along any line from the centerline of the jet to the jet plume boundary should yield a value of unity which serves as a check on accuracy of the method.

Another subroutine uses an iteration procedure for obtaining relatively accurate definition of the flow field inside the jet exhaust of the supersonic axisymmetric nozzle without resorting to the fine mesh required for the input data and the correspondingly prohibitive number of data points, even for machine computation.

To eliminate crossing of the characteristics and the jet boundary (a physically impossible situation, which, however, results from the mathematical method of characteristics equations), the condition for weak shock was introduced into the basic program where the compression waves cross. This approach, although approximate, gives good results for isentropic expansion of the jet exhaust and also for the position of the shock. Comparison of results obtained by this and other exact methods has been satisfactory both in terms of flow properties and of shock and jet boundary contour. The shock is the envelope of the compression waves reflected from the jet boundary as the overexpanded flow is forced to turn in order to conform with pressure at the jet boundary.

[1] By R. Rashidian, who provided the Apollo Program description above and support to Power and Environmental Systems in formulating and programming the AP-214 freestream subprogram described in, subsection 2(b).

(b) Program Number AP-214 (Freestream)

When a jet exhausts into quiescent surroundings, the jet boundary pressure is assumed to be constant all along the jet boundary and equal to the ambient pressure. With this assumption, the boundary Mach number is a constant and is determined by the isentropic relation:

$$M_{b1} = \left\{ \frac{2}{k_e - 1} \left[\left(\frac{p_T}{p_{b1}} \right)^{\left(\frac{k_e - 1}{k_e} \right)} - 1 \right] \right\}^{1/2} \tag{11}$$

However, when a rocket is traveling in the atmosphere, the assumption of constant pressure on the jet boundary is no longer valid, because the interaction between the freestream flow and the jet boundary results in a pressure distribution that varies along the jet boundary. The pressure distribution on the jet boundary is dependent upon the freestream Mach number and the local slope of the jet boundary. In the transonic regime, by far, the most difficult, even the plume fineness ratio (ratio of the primary wave-length to the maximum plume diameter) is an important parameter in defining the boundary pressure.

At low altitude, the ambient pressure is relatively high, and the spreading of the jet exhaust is small. Then, if the freestream Mach number is supersonic, small perturbation or second order theory is likely to be simple and should yield satisfactory results. At high altitude, the ambient pressure is low and the freestream Mach number is usually high. At low ambient pressure, the jet exhaust spreads substantially; even reversal of the exhaust flow may occur in the vicinity of the nozzle lip. Thus, the jet boundary slope is very high, and with the high freestream Mach number the Newtonian Impact Theory is quite suitable. In this case, the boundary pressure may be expressed as a function of freestream Mach number and the jet boundary inclination at the point in question:

$$\frac{p_{b1}}{p_\infty} = 1 + k_\infty M_\infty^2 \sin^2 \theta_{b1} \tag{12}$$

The initial slope of the jet boundary, θ_{b1}, is calculated from the nozzle exit conditions as given by Equations 1 and 3 in the previous section. Simultaneous solution of Equations 1, 11, and 12 gives the initial boundary Mach number, slope, and pressure. Iteration is required to result in the correct initial slope. Once the initial slope is known, the succeeding points along the boundary may be computed from the geometry shown in Figure 15.

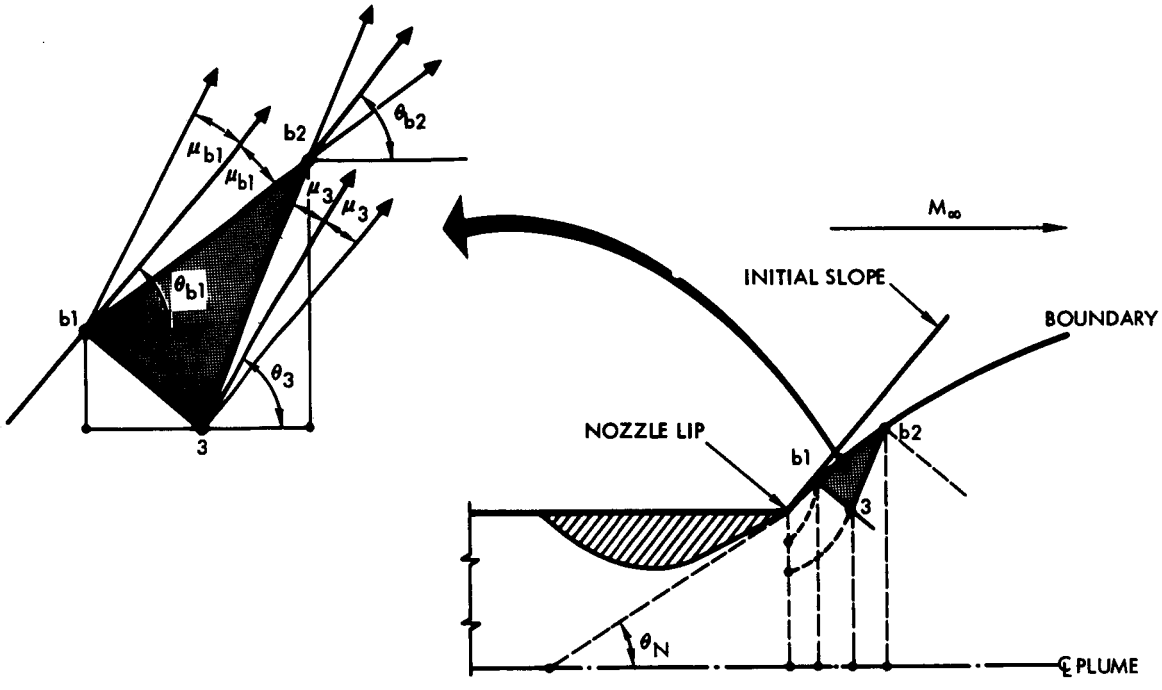

Figure 15. Geometry of Freestream-Plume Characteristics Solution

With points b1 and 3 known, point b2 is computed as follows:

$$x_{b2} = \frac{x_3 + K_3 \, (r_{b1} - r_3 - x_{b1} \tan \theta_{b1})}{1 - K_3 \tan \theta_{b1}} \tag{13}$$

where $K_3 = \cot (\theta_3 + \mu_3)$

$$r_{b2} = r_3 + \frac{x_{b2} - x_3}{K_3} \tag{14}$$

$$p_{b2} = p_\infty \, (1 + k_\infty \, M_\infty^2 \, \sin^2 \theta_{b1}) \tag{15}$$

$$M_{b2} = \left\{ \frac{2}{k_e - 1} \left[\left(\frac{p_{Tb2}}{p_{b2}} \right)^{\frac{k_e - 1}{k_e}} - 1 \right] \right\}^{1/2} \tag{16}$$

$$\theta_{b2} = \theta_3 + A_3 \, (M_{b2} - M_3) - B_3 \, (x_{b2} - x_3) + C_3 \, (S_{b2} - S_3) \tag{17}$$

where

$$A_3 = \sqrt{M_3^2 - 1} \Big/ \left[M_3 \left(1 + \frac{k-1}{2} M_3^2 \right) \right]$$

$$B_3 = 1 \Big/ \left[r_3 \left(\sqrt{M_3^2 - 1} \cot \theta_3 - 1 \right) \right]$$

$$C_3 = \sqrt{M_3^2 - 1} \Big/ \left[(k-1) M_3^2 \right]$$

and

$S_{b2} - S_3$ = entropy change

For the approximate shock solution, p_{Tb2} is the same as the chamber total pressure, and the entropy term in Equation 17 is deleted; for the exact shock solution, p_{Tb2} has to be computed and the entropy term should be retained.

Equation 12 is not valid for θ_b greater than 90 degrees; therefore, to avoid difficulty in cases where the boundary reversal occurs, it was assumed that the boundary pressure is equal to the stagnation pressure behind a normal shock; i.e., θ_b = 90 degrees.

A more exact treatment of the external flow employs exact shock and characteristic solutions in the region bounded by the "external" freestream shock and the jet boundary, but this would require additional work. The approximate method was programmed as a subroutine to the S&ID method of characteristics solution for the jet plume free-flow field.

Initial results of the combined computer program (AP-214, Freestream) showed how the width of the plume from a moving rocket was contracted from its free-flow field width as a function of the freestream Mach number, M_∞, for a series of planes located 1, 2, 5, 10, and 15 nozzle-exit radii downstream of the exit plane (Table 6). The case selected for study was for a nozzle-exit Mach number M_e = 3.0, exit specific heat ratio k = 1.3 (assumed constant during subsequent plume expansion), ratio of total pressure at exit to ambient pressure p_T/p_∞ = 10,000, and nozzle exit half-cone angle θ_N = 15 degrees. The marked reduction in plume diameter near the nozzle exit with an exit Mach number of 4 instead of 3 in the above case is illustrated by comparing the plume diameter contraction ratios at freestream Mach number 5:

x/R_e	$\frac{x}{R_e} = 1$	2	5	10	15
Mach number 3	0.56	0.50	0.48	0.47	0.45
Mach number 4	0.24	0.33	0.40	0.43	0.45

Table 6. Plume Boundaries and Contraction Ratios Versus Freestream Mach Number at Various Downstream Planes*

Mach Numbers (M_∞)	$x/R_e = 1$	2	5	10	15
DIMENSIONLESS RADIAL DISTANCES					
0	3.2	5.0	9.1	14.2	18.5
1	2.8	4.1	7.0	11.0	13.8
2	2.4	3.5	6.0	9.2	11.5
3	2.2	3.1	5.3	8.1	10.1
4	2.0	2.8	4.8	7.3	9.1
5	1.8	2.5	4.4	6.6	8.3
6	1.7	2.3	4.0	6.1	7.7
7	1.6	2.2	3.8	5.7	7.2
8	1.6	2.1	3.7	5.4	6.7
9	1.6	2.1	3.5	5.1	6.3
10	1.5	2.1	3.4	4.8	5.9
CORRESPONDING CONTRACTION RATIOS					
0	1.00	1.00	1.00	1.00	1.00
1	0.88	0.82	0.77	0.76	0.75
2	0.75	0.70	0.66	0.65	0.62
3	0.69	0.62	0.58	0.57	0.54
4	0.63	0.56	0.52	0.51	0.49
5	0.56	0.50	0.48	0.47	0.45
6	0.53	0.46	0.45	0.43	0.42
7	0.52	0.44	0.42	0.40	0.39
8	0.50	0.42	0.40	0.38	0.36
9	0.50	0.42	0.38	0.36	0.34
10	0.49	0.41	0.37	0.33	0.32

*For $M_e = 3$; $k = 1.3$; $p_T/p_\infty = 10,000$, and $\theta_N = 15°$

The effect of varying the specific heat ratio during plume expansion was discussed and results presented in a previous section for the case of the free-flow field plume of a nonmoving nozzle. In order to determine the effects with the freestream interaction for the moving nozzle, additional runs were made with the freestream program and the following input variables;

1. Specific heat ratio of 1.2, instead of 1.3, to provide a large percent change in the event that the effect was small (as proved to be the case),

2. Nozzle half-cone exit angle of 10 instead of 15 degrees to provide a closer approximation to the more typical design condition of the larger area expansion ratio nozzle,

3. Exit total-to-ambient pressure ratio of 100, instead of 10,000, to provide conditions simulating a lower-altitude nozzle design.

All of these cases were computed using the same nozzle-exit Mach number of 3.0 as a reference value, constant specific heat ratio of 1.4 for the freestream (air), and freestream Mach numbers of 0, 5, and 10, except in one case with the combined lower pressure ratio and exit angle, for which a solution was obtained only for $M_\infty = 0$ and 2.

The results showing the effects of the two specific heat ratios and exit angles on the contraction of the plume boundary are shown in Figures 16 and 17 (with intermediate freestream Mach number effects obtained by cross-plotting). As anticipated, the effects on the range of specific heat ratio and nozzle angle excursions tested had only relatively small influence on the contraction ratio for all freestream Mach numbers, particularly after the first few exit radii downstream of the nozzle exit. For example, from Figure 16, the plume contraction ratios at the dimensionless downstream distance $x/R_e = 5$, for freestream Mach numbers of 0, 1, and 2, using the specific heat ratio $k = 1.3$ as the reference, are 9.1/9.1, 7.0/9.1, and 6.0/9.1, or 1.00, 0.77, and 0.66, respectively. The ratios corresponding to a change in k of (1.2-1.3/1.3) 100 = -7.7% are then 9.8/9.1, 7.3/9.1, and 6.2/9.1, or 1.08, 0.80, and 0.68, respectively.

Dividing the percent changes in the ratios by the percent change in the varied parameter now indicates that the contraction ratios for $M_\infty = 0$, 1 and 2 are 1.04, 0.39, and 0.26% higher than the reference values due to 1% decreases in the specific heat ratio.

Similarly, from Figure 17, the contraction ratios for $M_\infty = 0$, 1, and 2 at $x/R_e = 5$ may be calculated as 0.33, 0.30, and 0.23% lower than the reference values due to 1% decrease in the nozzle half-cone exit angle. Of course

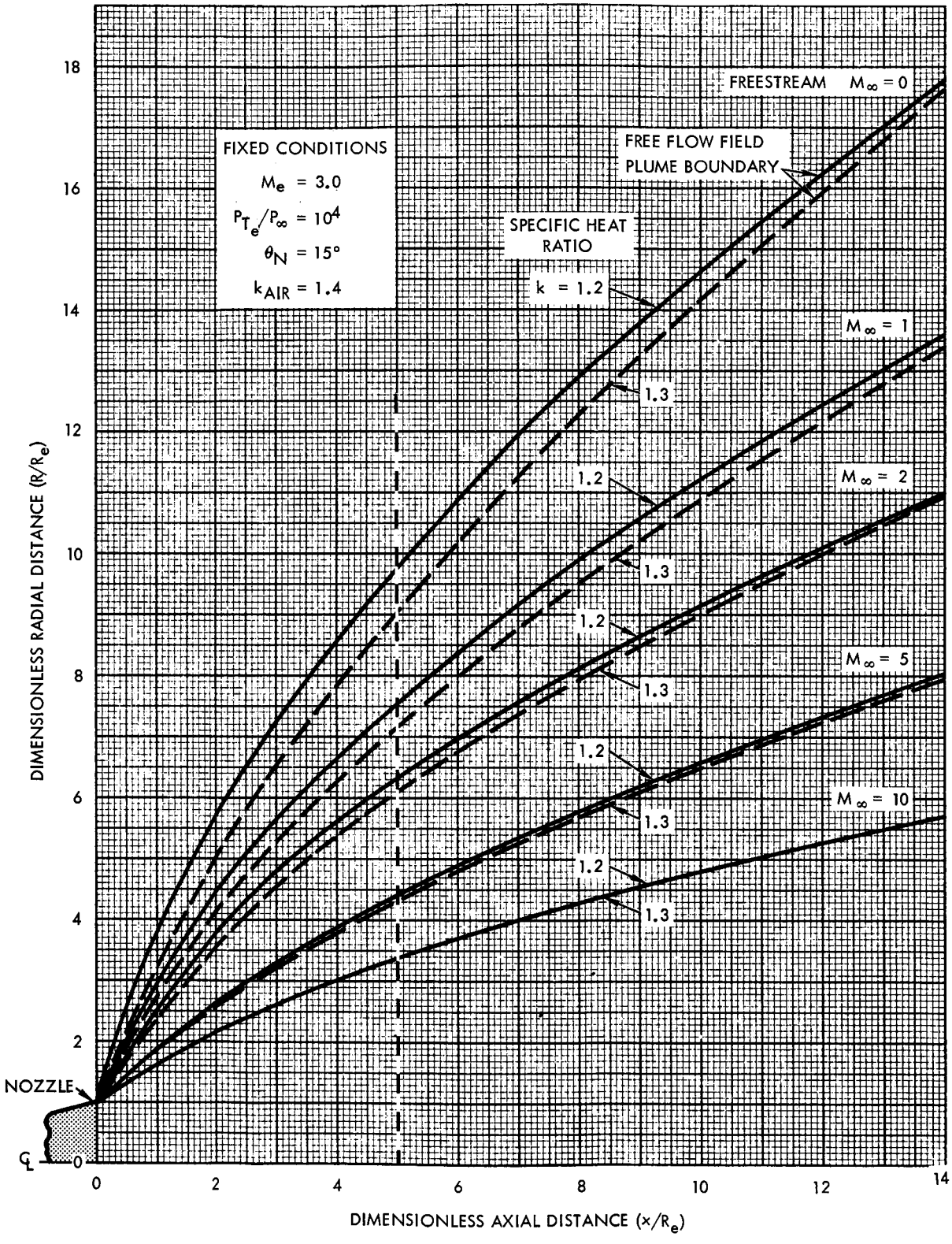

Figure 16. Effect of Freestream Mach Number and Specific Heat Ratios of 1.2 and 1.3 on Jet Plume Boundary

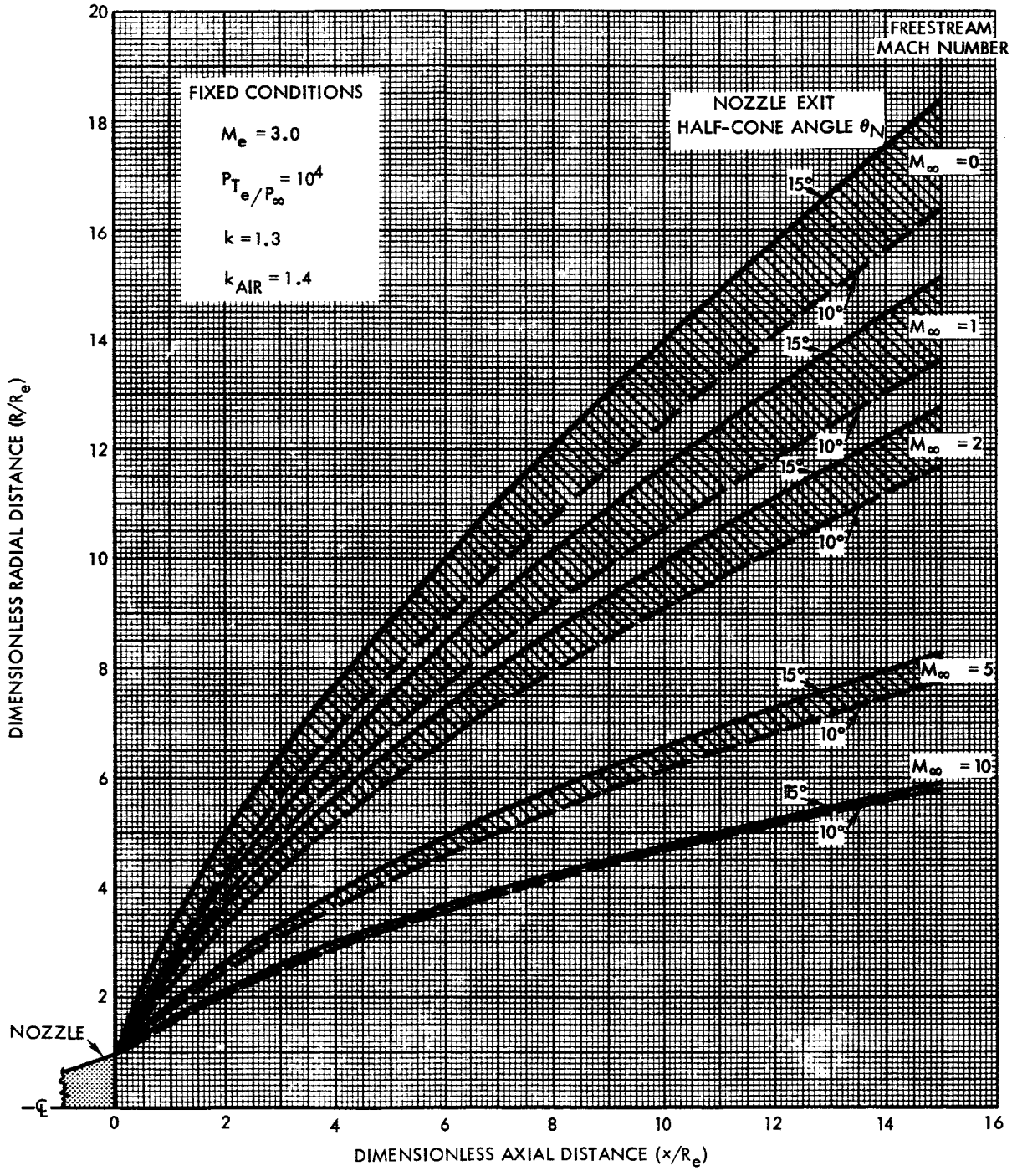

Figure 17. Effect of Freestream Mach Number and Nozzle Exit Angles of 10 and 15 Degrees on Jet Plume Boundary

the reference nozzle half-cone angle could be selected preferably at 10 degrees, as a more representative case, and the resulting percent contraction changes for M_∞ = 0, 1, and 2, then would be +0.38, +0.34, and +0.23, respectively, at the same x/R_e distance, for a +1% increase in θ_N.

D. INFLUENCE COEFFICIENTS FOR "STANDARD" JET PLUMES

Similar influence coefficients for the principal variables entering into the jet plume calculation could be determined over a variety of plume environments. The preliminary results indicate that the concept of a broad band of practical sea level and in-flight jet plume descriptions handled by a judicious choice of such influence coefficients may be feasible, due to the small effects of many of the variables. Since the very large number of possible combinations of the variables precludes making general tables of plume descriptions covering all cases, an approach to this goal in future investigations would be the determination of sets of influence coefficients applicable to selected "standard" plumes for low-, intermediate-, and high-altitude environments.

III. JET PLUME IMPINGEMENT GEOMETRY

Since an elemental area on any curved surface fits into the category of a canted plane, the obvious practical expedient frequently used for solution of impingement pressures on complex shapes has been to divide up the complex surface into a series of canted planes, locate these with respect to the nozzle exit reference origin, and then proceed with this approximate type of solution.

However, except for typical structural members of the umbilical towers and launch pads, most actual cases of impingement surfaces are more accurately described as portions of the concave and convex surfaces of cylinders whose longitudinal axes are parallel, axially canted, or at right angles to the plume axis, or as a portion of the convex surface of a sphere. Explicit solutions for these typical cases are desirable. Original derivations based on the consistent use of standardized jet plume flow field parameters in analytical solid geometry are presented in the following sections. These include the cases of impingement on the surfaces of;

1. The canted or uncanted side impingement plate
2. The concave cylinder parallel to the plume axis
3. The convex cylinder parallel to the plume axis
4. The convex cylinder canted to the plume axis
5. The convex cylinder at right angles to the plume axis
6. The sphere.

While the more complex cases might have been derived first and the results then reduced to those for the simpler cases, the development proceeding from the simpler cases serves to emphasize the visualization technique leading to the generally similar methods of solution. For simplicity and better understanding of the geometrical analysis, the actual plume distances, x_p, from the nozzle exit plane and the radial distances, R, from the plume axis are depicted in the diagrams for the curved surfaces and used in the derivations rather than the customary dimensionless distances, x_p/R_e and R/R_e, relative to nozzle exit radius, R_e. However, the resulting equations are applicable using these dimensionless plume parameters provided all other dimensions, including those describing the surfaces, are read as

dimensionless ratios relative to R_e. In all cases the desired result is the sine function of the true streamline impingement angle which is required to solve the impact pressure prediction equation derived in Section IV of this report.

A. IMPINGEMENT ON FLAT PLATES

There are various ways of establishing the location of a general plane surface at any distance and orientation from the plume reference origin which is the center of the rocket nozzle-exit plane. However, since the instrumentation and side plate location in the Apollo SM-RCS tests at Tullahoma were determined and controlled by an offset dimension measured from the nozzle exit center, together with a hinge or cant angle between a parallel to the nozzle and plume centerline and a line through the side plate, these parameters are used here to facilitate correlation with the test data. Figure 18 shows the geometry of the impingement of a streamline on a canted plate. The resulting relations cover the case for an uncanted plate by simply making the cant angle zero.

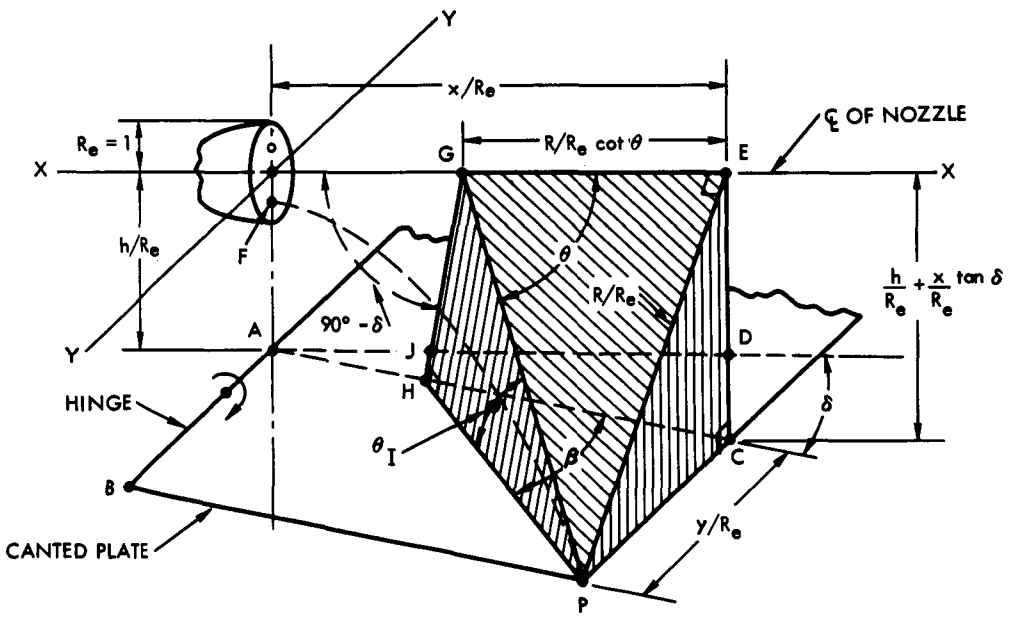

Figure 18. Geometry of Jet Impingement on a Canted Plate

The canted side plate ABPC is located by (1) the radial offset distance OA, or h/R_e from the nozzle-exit center perpendicular to the plate hinge axis AB in dimensionless ratio units relative to the nozzle exit radius R_e, and (2) the angle CAD, or δ, that the line AC makes with AD and also with the nozzle axis in the vertical plane OACE through the axis.

The tangent to streamline FP at the plate impingement point, P, and intersecting the axis at G is GP.

The perpendicular plane GHP which passes through this tangent, intersects the plate along the line HP and contains the true impingement angle GPH, or θ_I. It is established by swinging GH from the line OG by the complement of the cant angle, or $90° - \delta$. This true impingement angle must be expressed in terms of the streamline flow angle, PGE, or θ and the dimensionless coordinates of the point P in the jet plume, x/R_e and R/R_e. The latter is the hypotenuse of the right triangle PCE with P at the transverse distance CP, or y/R_e from the nozzle axis.

Noting that the vertical distance of point P from E is EC or $h/R_e + x/R_e \tan\delta$, the radial distance becomes:

$$\frac{R}{R_e} = \sqrt{\left(\frac{y}{R_e}\right)^2 + \left(\frac{h}{R_e} + \frac{x}{R_e}\tan\delta\right)^2} \tag{18}$$

The sine of θ_I is GH/GP, in which GH is evaluated by noting that

$$GH\cos\delta = \frac{h}{R_e} + \left(\frac{x}{R_e} - \frac{R}{R_e}\cot\theta - GH\sin\delta\right)\tan\delta$$

and GP is $(R/R_e)/\sin\theta$. After simplification, the sine of the true impingement angle in terms of jet plume free-flow field parameters and the defined location of the canted plane becomes:

$$\sin\theta_I = \sin\theta\cos\delta\left[\frac{\frac{h}{R_e} + \frac{x}{R_e}\tan\delta}{R/R_e}\right] - \cos\theta\sin\delta \tag{19}$$

For the case of the uncanted plane with $\delta = 0$ in Equation 19, the sine of the true impingement angle is simply

$$\sin\theta_I = \sin\theta\left(h/R_e \Big/ R/R_e\right) \tag{20}$$

The azimuth angle β shown in Figure 18 is also of significance for indicating direction of flow from the line of symmetry on the impacted surface. Time was not available to develop the use of this parameter for calculating reverse flow rates.

B. IMPINGEMENT ON CONCAVE AND CONVEX CYLINDERS

1. Concave Cylinder Parallel to Plume Axis

As illustrated in Figure 19(A) the plane tangent to the curved surface at the point of impingement, P, must now be considered in place of the canted plate, to determine the true angle APE, or θ_I. Since the axis of the cylinder in the XX direction is parallel to the plume axis, the view in the XZ plane shows the true length of the perpendicular BD dropped from the axis end A of the streamline tangent AP to the tangent plane DP (shown as AE in the perspective view on the left). These lengths can be evaluated using plane analytical geometry as follows:

BD is the cosine projection of the radial distance R of impingement point P from the axis. The angle DBP, or α, is the same as the alternate interior angle BPC between parallel lines BD and PC, and evaluated by the cosine relation for the plane oblique triangle BPC with three sides known. The length AP is simply defined in terms of the plume parameters, as $R/\sin\theta$. Dividing and simplifying these results leads to the desired value of $\sin\theta_I$ in terms of the known cylinder radius, R_c, and location of the cylinder axis in the YZ plane, Z_c, and the known jet plume parameters, R, and the angle θ made by the tangent to the streamline at point P and the plume axis:

$$\sin\theta_{I_{cc}} = \frac{(R_c^2 + R^2 - Z_c^2)\sin\theta}{2 R_c R} \tag{21}$$

for the case of impingement on the concave surface of a cylinder whose axis is parallel to the plume axis.

Solutions could be made for a series of radial distances, R_o, R_1, R_2, etc., from the plume axis, with impingement occurring from the minimum value, $R_o = R_c - Z_c$, to the maximum value, $R_c + Z_c$, and repeated for as many transverse planes located at distances x_1, x_2, etc., as needed, to envelop the particular cylindrical shape subjected to impingement.

The locations of the impingement points on the cylinder in each X plane are obtained from simultaneous solution of the equations of the plume impingement circle with radius R and the cylinder circle with radius R_c, or from:

$$R^2 = Z_p^2 + y_p^2 \tag{22}$$

$$R_c^2 = (Z_p - Z_c)^2 + y_p^2 \tag{23}$$

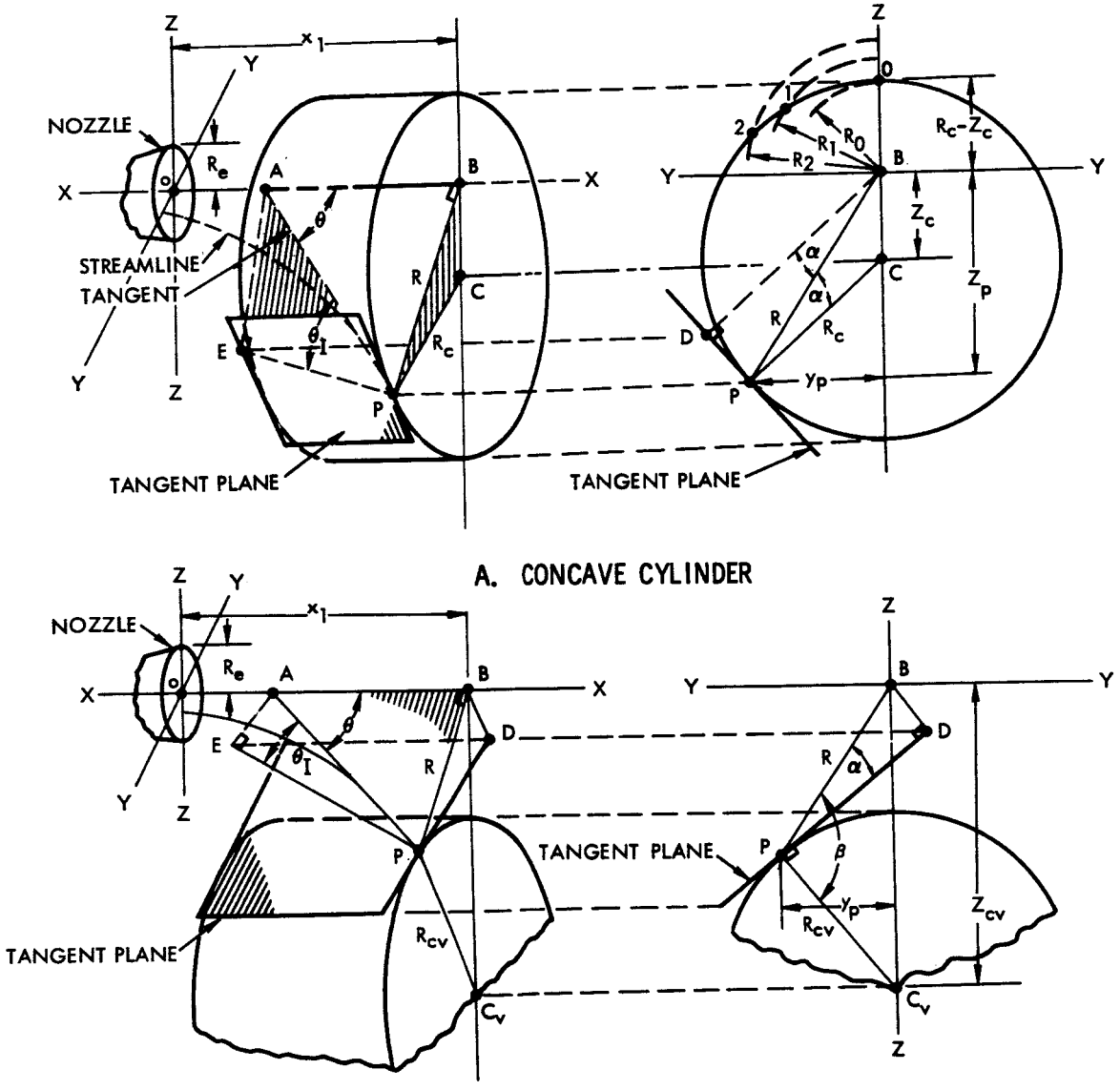

Figure 19. Geometry of Jet Impingement on Concave and Convex Cylinders Parallel to Plume Axis

which yield

$$Z_p = \frac{Z_c^2 + R^2 - R_c^2}{2 Z_c} \tag{24}$$

and

$$y_p = \sqrt{R^2 - Z_p^2} \tag{25}$$

In the case of a cluster of nozzles, a first approximation to the total impingement pressures could be obtained by using the principle of superposition, or simple summation of the individual plume pressure contributions. This may be sufficient to indicate maximum pressure locations. A second approximation could include the effects of primary mutual impingement of the plumes on phantom separation walls, and then the secondary impingement of the resulting composite plume on the actual wall surface. Such estimates are needed also to establish the aft and forward (reverse) flows for base pressure and heating investigations. These calculations are complex and should be made for specific applications where the detailed geometry and engine plume descriptions are available, but they are outside the scope of the present effort to establish the basic engineering techniques.

2. Convex Cylinder Parallel to Plume Axis

Figure 19(B) shows the elements of this problem. Again the true value of $\sin \theta_I$ is desired. The required right triangle consisting of the perpendicular to the tangent plane and the tangent to the streamline is shown as AEP in the perspective view, and as BDP in the YZ plane view. The true length of the tangent AP, in terms of the plume flow-field parameters, is $R/\sin\theta$. Thus, $\sin \theta_I$ = BD (or AE)/AP, or $R \sin \alpha / (R/\sin \theta) = \sin \alpha \sin \theta$.

The angle BDP, or α, is evaluated by observing that $\beta = 90° + \alpha$, and $\sin \alpha = \cos \beta$. Using the cosine law of plane geometry to solve for $\cos \beta$ in triangle BPC_v, with side PB = R, side $BC_v = Z_{cv}$, and side $PC_v = R_{cv}$, we have

$$\cos \beta = \frac{R_{cv}^2 + R^2 - Z_{cv}^2}{2 R_{cv} R} \tag{26}$$

The desired sine function of the true impingement angle then becomes

$$\sin\theta_{I_{cv}} = \frac{(Z_{cv}^2 - R_{cv}^2 - R^2)\sin\theta}{2\,R_{cv}R} \tag{27}$$

for the parallel convex cylinder surface impingement.

As before, a series of solutions are required in each transverse section, and sufficient transverse sections considered to envelop the portion of the cylinder under impingement. The same equations (22 through 25) apply for locating the impingement points as given above for the concave cylinder.

3. Canted Convex Cylinder

This case, illustrated in Figure 20, is typical for the impingement of angled pitch and yaw, reaction-control, engine plumes on the vehicle cylinder. The location of the cylinder axis relative to the plume coordinate system is defined by the cant angle δ and the perpendicular distance, a, from the nozzle exit center origin to the nearest element of the cylinder. The elliptical section of the cylinder cut by a transverse plume plane at distance x_p from the nozzle exit is shown in Section A-A, and a transverse plane through the cylinder cutting the plume axis at its intersection with the streamline tangent AP is shown in Section B-B. The location of the coordinates of the streamline impingement point on the cylinder is determined by simultaneous solution of the equation of the circle of plume radial distance, R, (with x_p constant):

$$R^2 = y_p^2 + Z_p^2 \tag{28}$$

and the equation of the elliptical section of the cylinder in Section A-A:

$$\frac{(Z_p - Z_c)^2}{(R_c/\cos\delta)^2} + \frac{y_p^2}{R_c^2} = 1 \tag{29}$$

which yields

$$Z_p = \sqrt{Z_c^2\cot^4\delta + (R^2 - R_c^2 + Z_c^2\cos^2\delta)/\sin^2\delta} - Z_c\cot^2\delta \tag{30}$$

For small angles, substitution of $\cos\delta = 1$ and $\sin\delta = \delta$ in Equation 30 results in the same value for Z_p as Equation 24 gives for the parallel cylinder. As before, y_p is then evaluated from Equation 28 as $\sqrt{R^2 - Z_p^2}$.

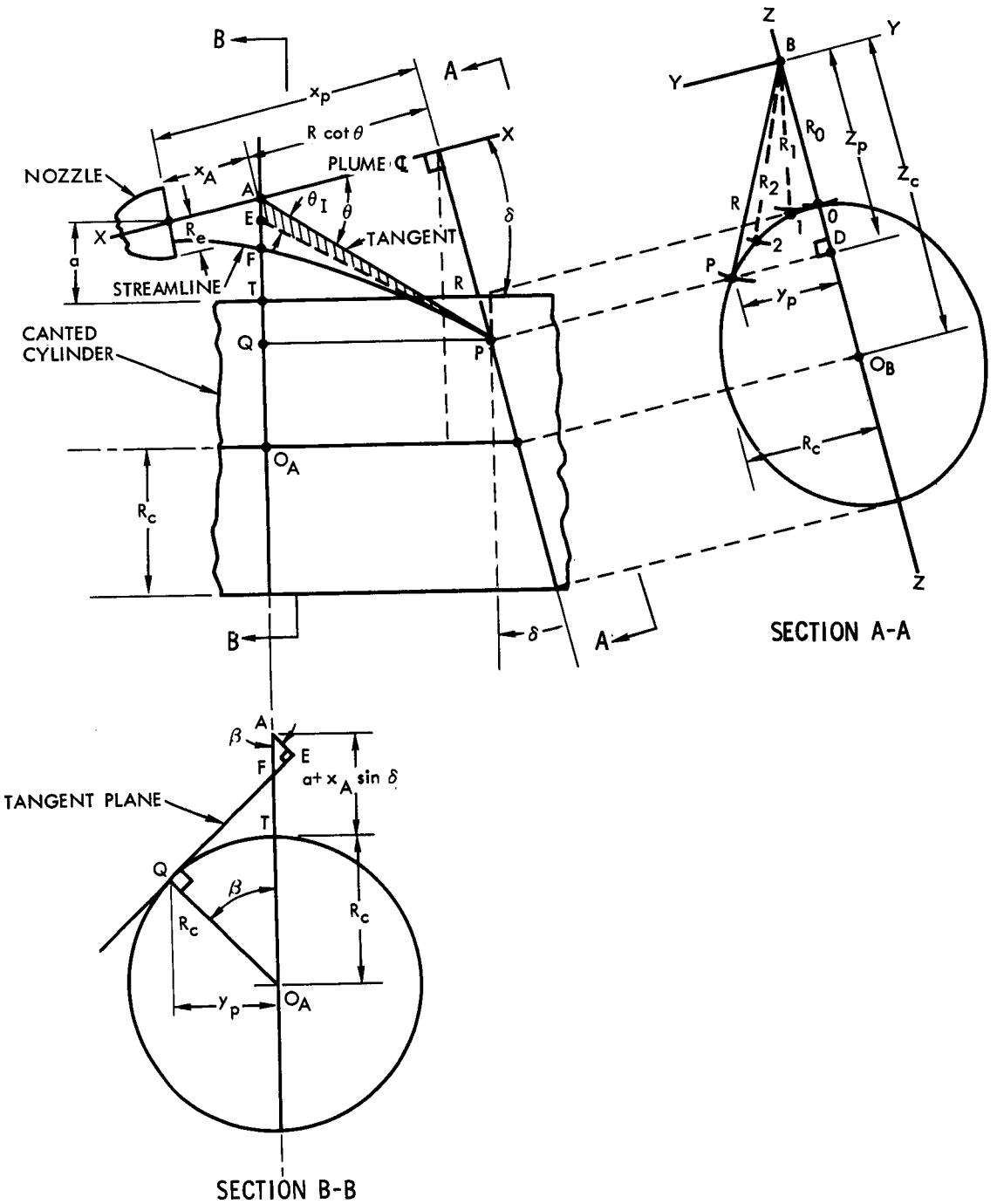

Figure 20. Geometry of Jet Impingement on Canted Convex Cylinder

Since Z_c varies for each selected value of x_p, it must be evaluated to complete the solution of the above equations. From the given geometry

$$Z_c = (a + x_p \sin \delta + R_c)/\cos \delta \tag{31}$$

Section B-B in Figure 20 provides the plane geometry for calculating the required perpendicular distance, AE, to the tangent plane EFQP from the similar right triangles O_AQF and FEA. Thus

$$AE = AF \cos \beta = (AO_A - FO_A) \cos \beta$$

$$= (a + x_A \sin \delta + R_c - R_c/\cos \beta) \cos \beta$$

with

$$\cos \beta = \sqrt{1 - \sin^2 \beta} = \sqrt{1 - (y_p/R_c)^2}$$

and the tangent length $AP = R/\sin \theta$, the desired sine function of the true impingement angle θ_I becomes

$$\sin \theta_{I_{ccv}} = \sin \theta \left[(a + x_A \sin \delta + R_c) \sqrt{1 - (y_p/R_c)^2} - R_c\right]/R \tag{32}$$

When the cant angle approaches zero, Equation 32 reduces to Equation 27 for the case of the parallel convex cylinder.

4. Convex Cylinder at Right Angles to Plume Axis

This case is typical for reaction-control roll engines having their thrust directed at right angles to the vehicle cylinder axis. Figure 21 shows a transverse section of the cylinder in a longitudinal section of the rocket plume. The locations x_c and y_c of the center of the cylinder relative to the reference nozzle-exit origin, 0, are needed together with a series of streamline tangent angles θ_o, θ_1, θ_2, and radii from the plume axis, R_o, R_1, R_2, for each transverse plane of the plume at distance x_p. A single tangent plane CDP_oP illustrated in the perspective sketch A (Figure 21) serves to locate all points of intersection of the impinging streamlines for each x_p plume plane. The true impingement angle θ_I is APD in this sketch, and the desired sine function can be evaluated as AD/AP, where AP is the tangent to the streamline and known from the plume flow field description parameters as $R/\sin \theta$. The perpendicular distance of the plume axis end of this tangent line to the tangent plane is always AD which is found from the right triangle ADP_o.

The location of the impingement point on the cylinder surface is determined from the simultaneous solution of two equations of circles:

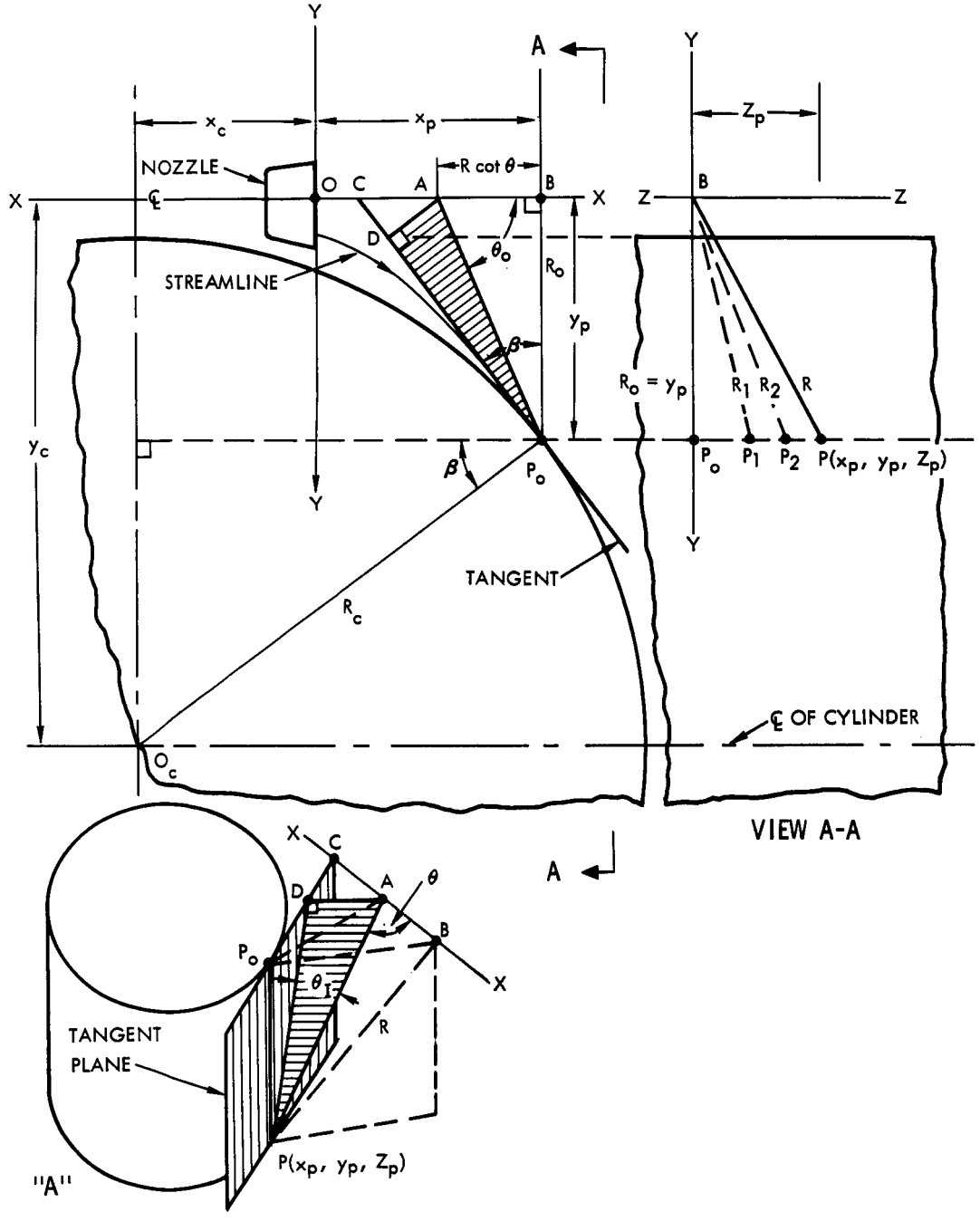

Figure 21. Geometry of Jet Impingement on Convex Cylinder at Right Angles to Plume Axis

$$R^2 = y_p^2 + Z_p^2 \tag{33}$$

for the plume radial distance circle, and

$$R_c^2 = (x_p + x_c)^2 + (y_p - y_c)^2 \tag{34}$$

for the cylinder.

Thus, since x_p is assumed constant for each plume section considered, Equations 33 and 34 now provide the remaining coordinates of the impingement point P (x_p, y_p, Z_p).

The angle AP_oD is ($\beta + \theta_o - 90°$) where β is $\sin^{-1}(y_c - y_p)/R_c$ and θ_o is $\tan^{-1} y_p$ (or R_o)/R cot θ.

Then

$$AD = AP_o \sin(\beta + \theta_o - 90°) = \sqrt{R^2 \cot^2\theta + y_p^2}\, \sin(\beta + \theta_o - 90°)$$

and the sine of the true impingement angle θ_I is:

$$\sin\theta_{I_{rc}} = \frac{\sqrt{R^2 \cot^2\theta + y_p^2}\, \sin(\beta + \theta_o - 90°)}{R/\sin\theta} \tag{35}$$

C. IMPINGEMENT ON SPHERES

Figure 22 shows the elements of the impingement problem for spherical surfaces partly or wholly immersed in the plume flow field. The familiar special case of a hemispherical blunt leading edge in aerodynamic flow could be obtained when the spherical center location $Z_s = y_s = 0$. As in all preceding cases, the result sought is the sine function of the true impingement angle θ_I in the plane perpendicular to the tangent surface at the point of impingement. Again, a series of transverse planes, transverse to the plume axis, must be considered to obtain the full range of impingement. The YZ-planes intersect the sphere in circles whose radii can be determined, together with the remaining coordinates y_p and Z_p of the impingement point in terms of the known plume and sphere parameters, by simultaneous solution of the following three equations:

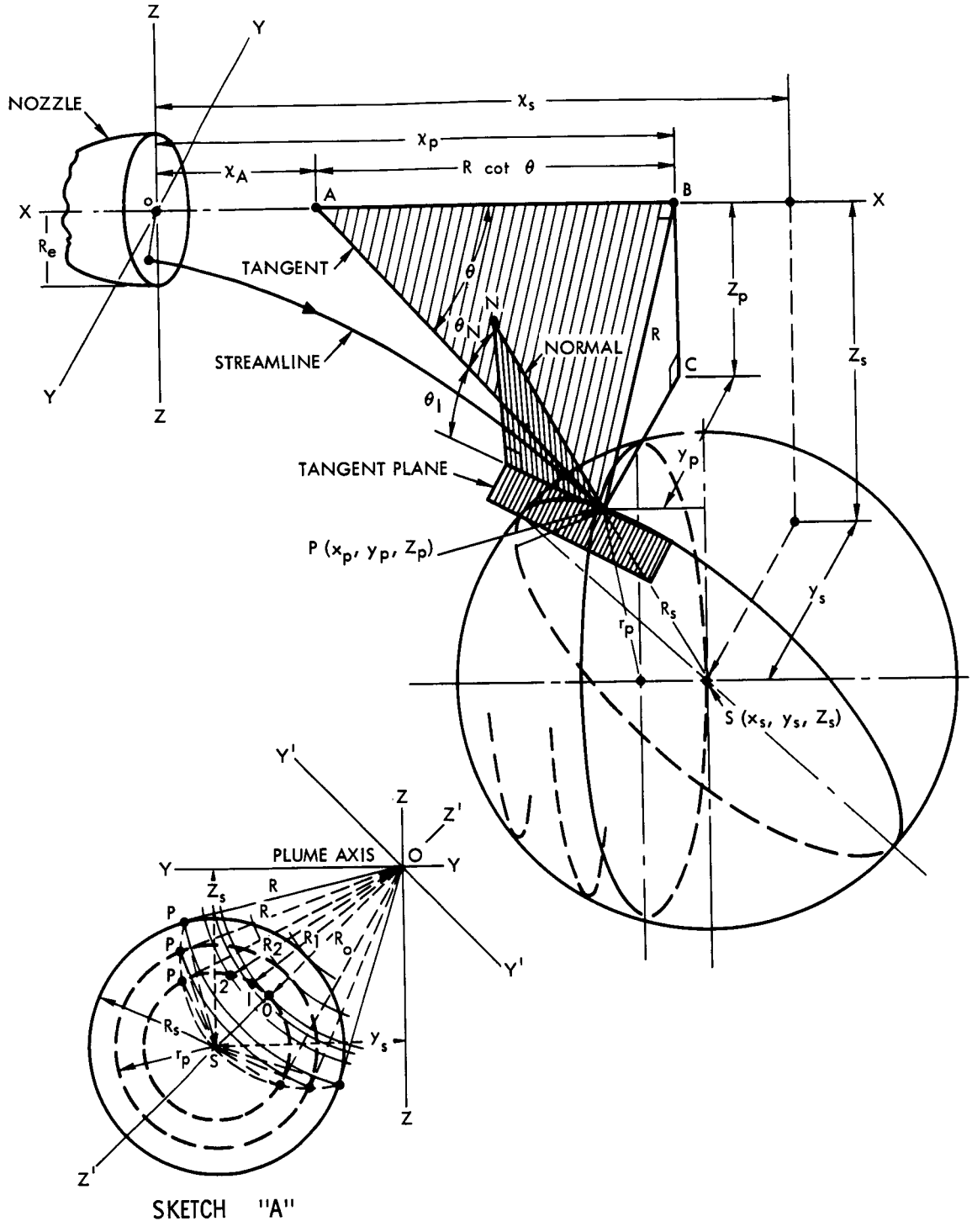

Figure 22. Geometry of Jet Impingement on Sphere

1. As before, the equation of the circle for the radial distance R of the impingement point from the plume axis:

$$R^2 = y_p^2 + Z_p^2 \tag{33}$$

2. The equation of the circle of intersection with the sphere in the x_p plane:

$$r_p^2 = (y_p - y_s)^2 + (Z_p - Z_s)^2 \tag{36}$$

3. The equation of the sphere:

$$R_s^2 = (x_p - x_s)^2 + (y_p - y_s)^2 + (Z_p - Z_s)^2 \tag{37}$$

Sketch A in Figure 22 indicates that the minimum plume radial distance R_o to be considered is:

$$R_o = \sqrt{y_s^2 + Z_s^2} - R_s \tag{38}$$

and the maximum plume radial distance,

$$R_{max} = \sqrt{y_s^2 + Z_s^2} + R_s \tag{39}$$

It is convenient in this case to determine the cosine of the complementary angle θ_n between the normal to the sphere at the point of impingement P and the streamline tangent AP as equivalent to the desired sine of the true impingement angle θ_I, or

$$\sin \theta_I = \cos \theta_n \tag{40}$$

with x_A equal to $x_p - R \cot \theta$, and $y_A = Z_A = O$ on the plume axis, the axis end coordinates of the space tangent line AP are known. After the impingement point coordinates are evaluated from Equations 33, 36, and 37, the direction cosines of this tangent can be determined. The coordinates of two points, P and S, on the normal NPS are now also known, so that its direction cosines likewise can be determined.

The cosine of the angle formed by the intersecting tangent AP and normal PS in terms of the two sets of direction cosines now may be found from the relation given in solid analytical geometry textbooks (Reference 23):

$$\cos \theta_n = \cos \alpha_t \cos \alpha_n + \cos \beta_t \cos \beta_n + \cos \gamma_t \cos \gamma_n \tag{41}$$

where the subscripts, t and n, refer to the tangent and normal lines, and the space angles α, β, and γ are the angles formed between the lines and the X, Y, and Z coordinate axes, respectively.

The direction cosines are defined by the ratios of the line intercepts parallel to XY, ZY, and ZX planes to the lengths of the lines between their two known point locations. Then, since the tangent length is known in terms of the plume parameters as $R/\sin\theta$, and the portion of the normal length PS is the given spherical radius, R_s, the direction cosines may be written as:

$$\cos\alpha_t = (x_p - x_A)/(R/\sin\theta) \tag{42}$$

$$\cos\beta_t = y_p/(R/\sin\theta) \tag{43}$$

$$\cos\gamma_t = Z_p/(R/\sin\theta) \tag{44}$$

for the tangent line, and as

$$\cos\alpha_n = (x_p - x_s)/R_s \tag{45}$$

$$\cos\beta_n = (y_p - y_s)/R_s \tag{46}$$

$$\cos\gamma_n = (Z_p - Z_s)/R_s \tag{47}$$

for the normal line.

Substituting the values of the direction cosines from Equations 42 through 47 into Equations 41 and 40 yields the desired sine function of the true impingement angle as

$$\sin\theta_{I_S} = \frac{\sin\theta}{R_s R}\left[(x_p - x_A)(x_p - x_s) + y_p(y_p - y_s) + Z_p(Z_p - Z_s)\right] \tag{48}$$

Note: As stated at the beginning of this section, all dimensions indicated by x_p, x_A, x_s, y_p, y_s, Z_p, Z_s, R_s and R in Equation 48, and similar dimensions in the final equations for the preceding cases, can be considered to be divided by the radius R_e of the nozzle in the exit plane, thus made dimensionless and compatible with the customary dimensionless plume parameters, x/R_e and R/R_e.

IV. IMPACT PRESSURES DUE TO JET PLUME IMPINGEMENT

A. NEWTONIAN IMPACT THEORY

With the makeup of the jet plume established in its environment of altitude and air flow, and the streamline impingement geometry prepared, the analysis proceeds to determine impingement forces on a flat plate or on the element of area of more complex surfaces. Preliminary use of two-dimensional shock-wave theory resulted in overestimating the extent of the pressure rise throughout the impingement zone by a factor of three or four on the measured values in cold-air tests (Reference 24). Later predictions using various model simulation laws went to the other extreme of underestimating the experimental cold-gas test pressures on a side plate.

These discrepancies may be avoided if the fundamental theory of a rocket propulsion force is kept firmly in mind; namely, that the total jet plume impingement force is no different, in a broad Newtonian sense, than the rocket propulsion force since it is defined by, and dependent on, the impacting plume momentum time rate of change. For example, a circular bundle of streamlines with cross-sectional area, A, striking a plate at the true impingement angle θ_I will cover a larger elliptical area, $A/\sin\theta_I$, as shown in Figure 23. This makes the equilibrium of dynamic forces, F_n, between the impingement pressure rise, p_I, times the impingement area, and the vertical time rate of momentum change, $\dot{m}V\sin\theta_I$, where $\dot{m} = \rho AV$,

$$F_n = \frac{p_I A}{\sin\theta_I} = \rho AV^2 \sin\theta_I$$

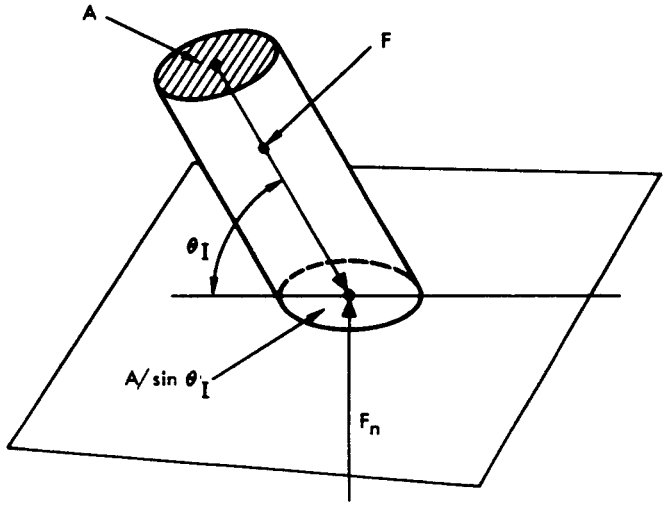

Figure 23. Geometry of Newtonian Impact Theory

from which the required dynamic pressure is found to be:

$$p_I = \rho V^2 \sin^2 \theta_I \tag{49}$$

Separation of the aerodynamic pressure equivalent $\rho V^2/2$ from Equation 49 yields the familiar expression for Newtonian pressure coefficient, $p_I/(\rho V^2/2)$,

$$C_p = 2 \sin^2 \theta_I \tag{50}$$

for drag on a canted flat plate in the form given in textbooks on hypersonic aerodynamics, although the derivation is somewhat different (Reference 25).

A modification of Equation 49 permits its more convenient use in terms of functions available in existing gas expansion tables, i.e., pressure ratios and Mach numbers, for the assumed isentropic expansion:

$$p_{I_x} = k\, p_T \left(\frac{p_x}{p_T}\right) M_x^2 \sin^2 \theta_{Ix} \tag{51}$$

where

p_{I_x} = impact pressure due to impingement at dimensionless distance x/R_e. (For total pressure at the surface, the static pressure p_x would be added.)

k = specific heat ratio of the gases at the nozzle exit, or averaged for the plume at some slightly higher value.

p_T = estimated total pressure required for the constant specific heat ratio k to give the same average exit pressure that the actual total chamber pressure (or stagnation pressure at the nozzle throat) and varying specific heat ratio would give during expansion through the nozzle.

Equations 49 and 51 were used to compare impingement pressures versus experimental values for a variety of jet plumes from sea-level to near-vacuum conditions. Detailed examples of two of these cases are given in the following subsection IV-B.

B. RESULTS OF CORRELATION STUDIES

1. Apollo Plume Pressure Correlation

For the Apollo SM-RCS test engines used in the high-altitude chamber tests at Tullahoma, the total (average) pressures at the nozzle exit were very nearly equal to the operating chamber pressures (83 to 101 psia) measured at the injector end (Reference 26). A reduction factor of 0.99 was estimated for the small effect of chamber-to-throat area contraction ratio. Effective gas specific-heat ratios corresponding to the nozzle area expansion ratios were used together with a constant assumed chamber gas temperature of 5400 R for the storable propellants. Except for the peak pressure which will be discussed subsequently, good correlation was obtained from Equation 51. Table 7 shows predicted and test impingement pressures for the centerline values for the cut-down nozzle with an area expansion ratio of 10, and an uncanted, or parallel, side impingement plate located 3-exit radii away from the nozzle and plume axis. Table 8 shows the pressure correlation along a transverse plane. Jet plume free-flow fields already available from prior Apollo work were used for the correlation study (Reference 27).

Table 7. Correlation of Predicted and Test Impingement Pressures Along Axial Centerline for High-Altitude Plume

Axial Distance (x/R_e)	Mach Number (M_x)	Impingement Angle (θ_x)	Impingement Pressures (psia)	
			Equation 51 Calculations	Faired Test Data
1	9.8	70	0.05	0.04
2	7.5	51	0.18	0.21
3	6.8	41	0.24	0.30
4	6.6	34	0.21	0.24
5	6.5	29	0.17	0.18
6	6.6	26	0.12	0.13
8	6.9	21	0.06	0.07
12	7.4	15	0.02	0.01

Table 8. Correlation of Predicted and Test Impingement Pressures in a Tranverse Plane (at $x/R_e = 7.4$) for High-Altitude Plume

y/R_e	R/R_e	θ_{xy}	M_{xy}	Impingement Pressures (psia)	
				Equation 51 Calculations	Faired Test Data
0	3.0	22	6.8	0.08	0.08
1.1	3.2	23	6.9	0.07	0.07
2.0	3.6	26	7.1	0.06	0.06
3.3	4.5	31	7.5	0.04	0.05
5.5	6.2	41	8.6	0.01	0.02

Following the concept of a critical shock location changing the laminar convective heat transfer from the oblique shock region to the normal shock region as discussed in subsection V-C, the hypothesis can be made that the peak impingement pressure is subject to a related interpretation of the larger impingement angle. An apparent preliminary correlation is obtained by use of the maximum deflection angle as a more appropriate effective impingement angle. Thus, in Table 7, for $M_x = 6.8$ and $k = 1.28$, the maximum deflection angle is about 48° instead of the 41° of the streamline. Substituting $\sin^2(48°)$ in Equation 51 now yields 0.31 psia as the impingement pressure which correlates well with the faired test value. The three-dimensional plot of the theoretical Newtonian pressure distribution on a parallel side plate (Figure 24) confirms an early prediction of the shape of the resulting warped surface, symmetrical only about the axial centerline of impingement on a parallel plate.

2. Saturn SA-5 Plume Pressure Correlation

The approximate dimensionless distances of the two data points from the eight nozzle-exit centers of the booster engine cluster were calculated from the geometry of the launch data of Reference 20 and are shown in Figure 25. Actual distances were divided by the radius of the nozzle exit (1.92 feet) to obtain the dimensionless values. The corresponding dimensionless axial and radial distances with respect to the nozzle-exit plane and the plume centerline as a function of flight time are shown in the chart on Figure 25. The nearest engine plume is inside of both Data Point No. 1 and 2 initially, and then sweeps over and beyond, indicating that the

ENVIRONMENT:

$\epsilon = 10$

$P_{T_e} = 88$ PSIA

$k = 1.28$

$h_\infty \approx 250{,}000$ FT

$h = 3\ R_e$

$\delta = 0°$

$M_\infty = 0$

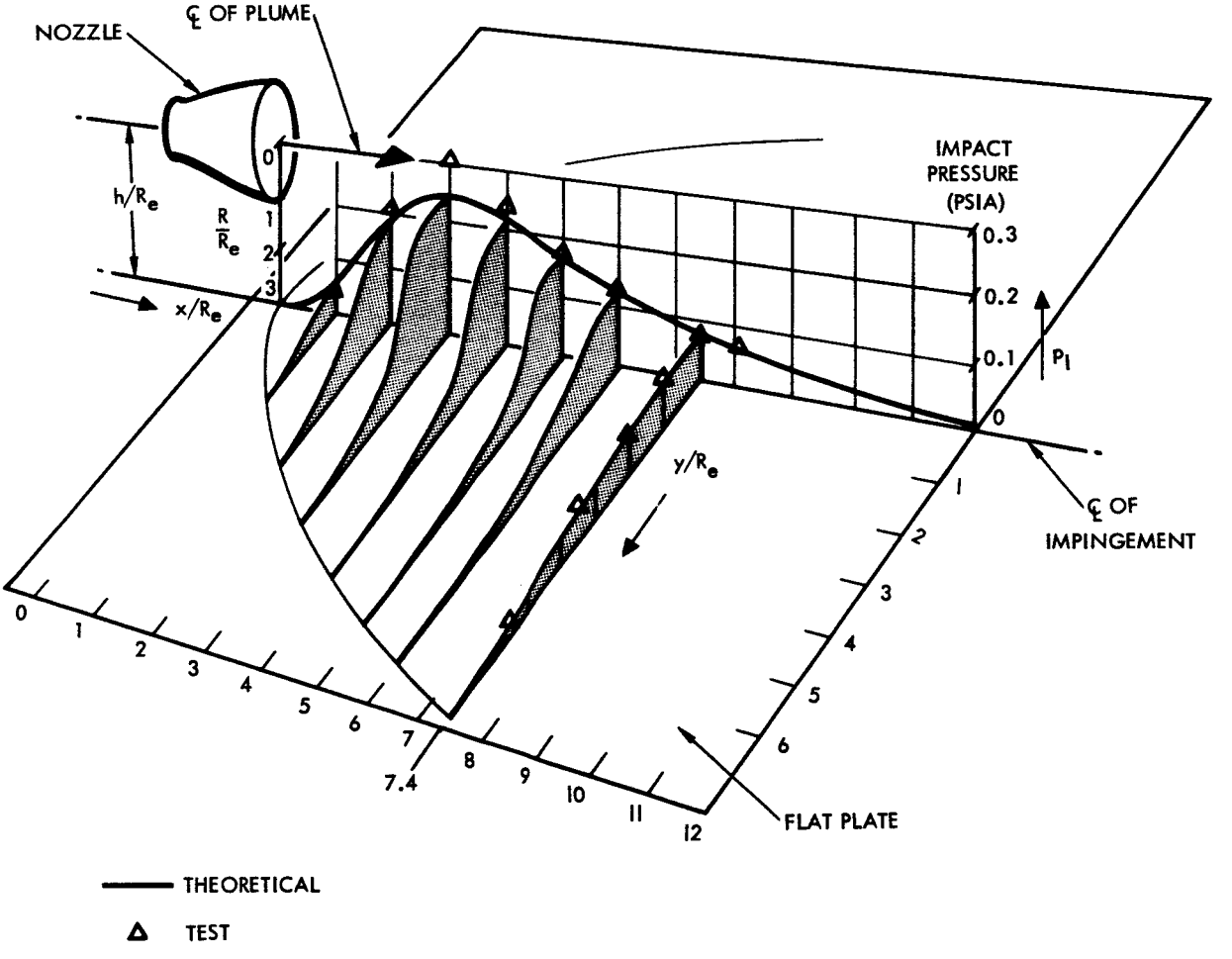

Figure 24. Three Dimensional Plot of Newtonian Pressure Distribution on a Parallel Flat Plate

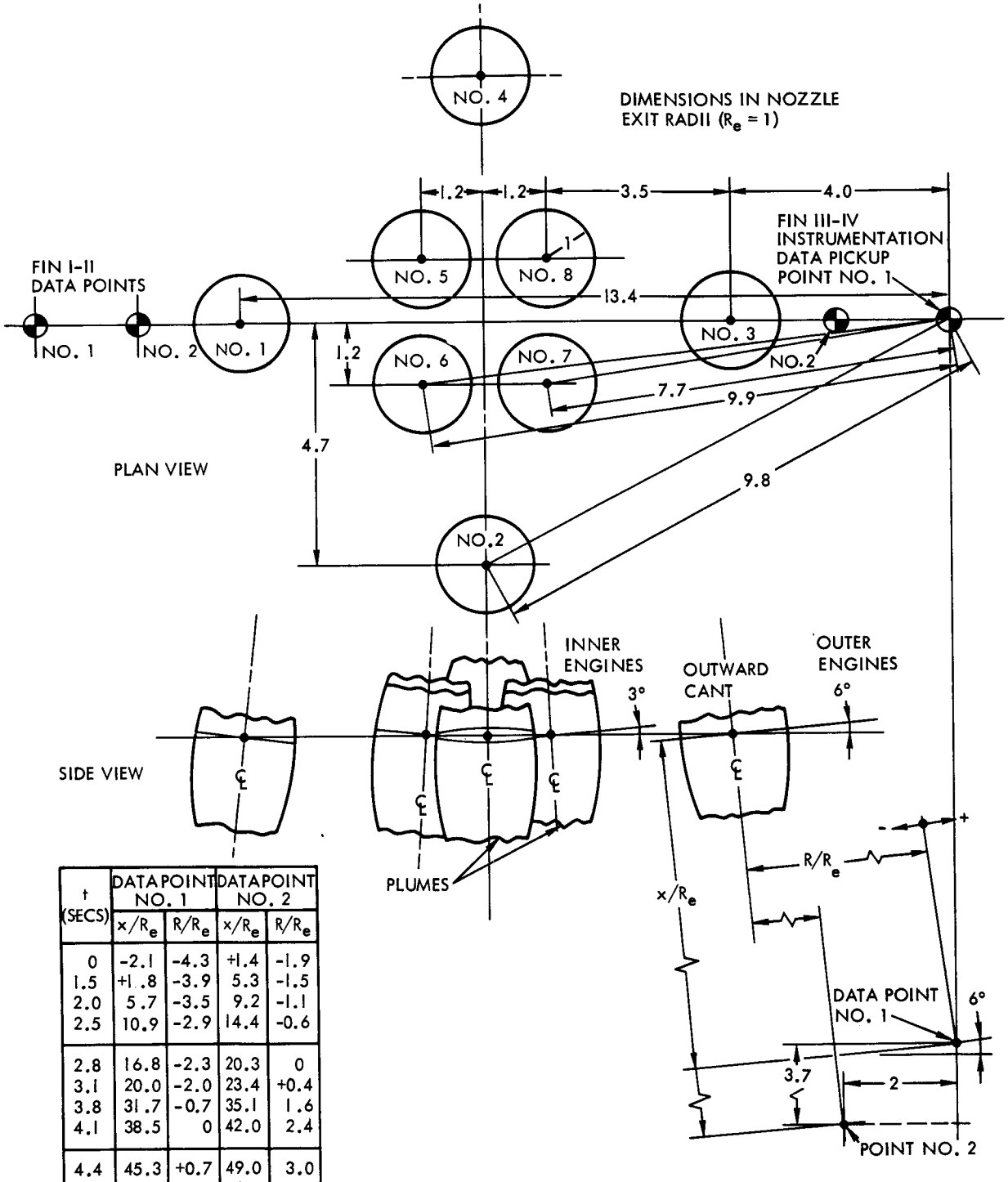

t (SECS)	DATA POINT NO. 1		DATA POINT NO. 2	
	x/R_e	R/R_e	x/R_e	R/R_e
0	-2.1	-4.3	+1.4	-1.9
1.5	+1.8	-3.9	5.3	-1.5
2.0	5.7	-3.5	9.2	-1.1
2.5	10.9	-2.9	14.4	-0.6
2.8	16.8	-2.3	20.3	0
3.1	20.0	-2.0	23.4	+0.4
3.8	31.7	-0.7	35.1	1.6
4.1	38.5	0	42.0	2.4
4.4	45.3	+0.7	49.0	3.0
5.0	60.9	2.3	64.5	4.7
5.5	75.0	3.8	78.5	6.2

Figure 25. Approximate Dimensionless Distances of Plume Centerlines and Nozzle Exits from Instrumentation for SA-5 Data Correlation

impingement force and heat loads should pass through maximum values; the predicted results and the test data show such maximum values.

Following the procedure outlined in Section II-B2, the prediction method requires that plume properties should be tabulated, or curves plotted (Figure 10), and should be used to determine local conditions at the different data point positions shown in Figure 25. Results are shown in Table 9, and plotted with the corresponding test data in Figure 26.

Table 9. Calculation of Predicted Pad Level Impingement Pressures for Saturn SA-5 Launch

t, secs	x/R_e	R/R_e	p_{Imx}	R_o/R_e	R/R_o	$\frac{q_x}{q_{mx}}$	p_{IRx}	p_{Iabs}
Data Point No. 1								
3.1	20.0	-2.0	87	1.0	2.0	0.02	1.7	16.4
3.8	31.7	-0.7	40	1.6	0.4	0.81	32.4	47.1
4.1	38.5	0.0	27	1.9	0.0	1.00	27.0	41.7
4.4	45.3	+0.7	18	2.3	0.3	0.91	16.4	31.1
Data Point No. 2								
2.0	9.2	-1.1	151	0.5	2.2	0.00	0.0	14.7
2.5	14.4	-0.6	125	0.8	0.8	0.45	56.2	70.9
2.8	20.3	0.0	85	1.0	0.0	1.00	85.0	99.7
3.1	23.4	0.4	70	1.2	0.3	0.91	63.7	78.4
3.8	35.1	1.6	32	1.8	0.9	0.37	11.8	26.5
4.1	42.0	2.4	22	2.1	1.1	0.25	5.5	20.2
4.4	49.0	3.0	15	2.6	1.2	0.20	3.0	17.7

Considering the rather approximate treatment (which is all that is justified in the application of Table 4 statistical ratios based on small engine tests without knowing the scale-up factors involved), the correlation of the prediction method values with the test values is indeed remarkable. Of course, additional checkout of the method is required to gain added confidence for general application.

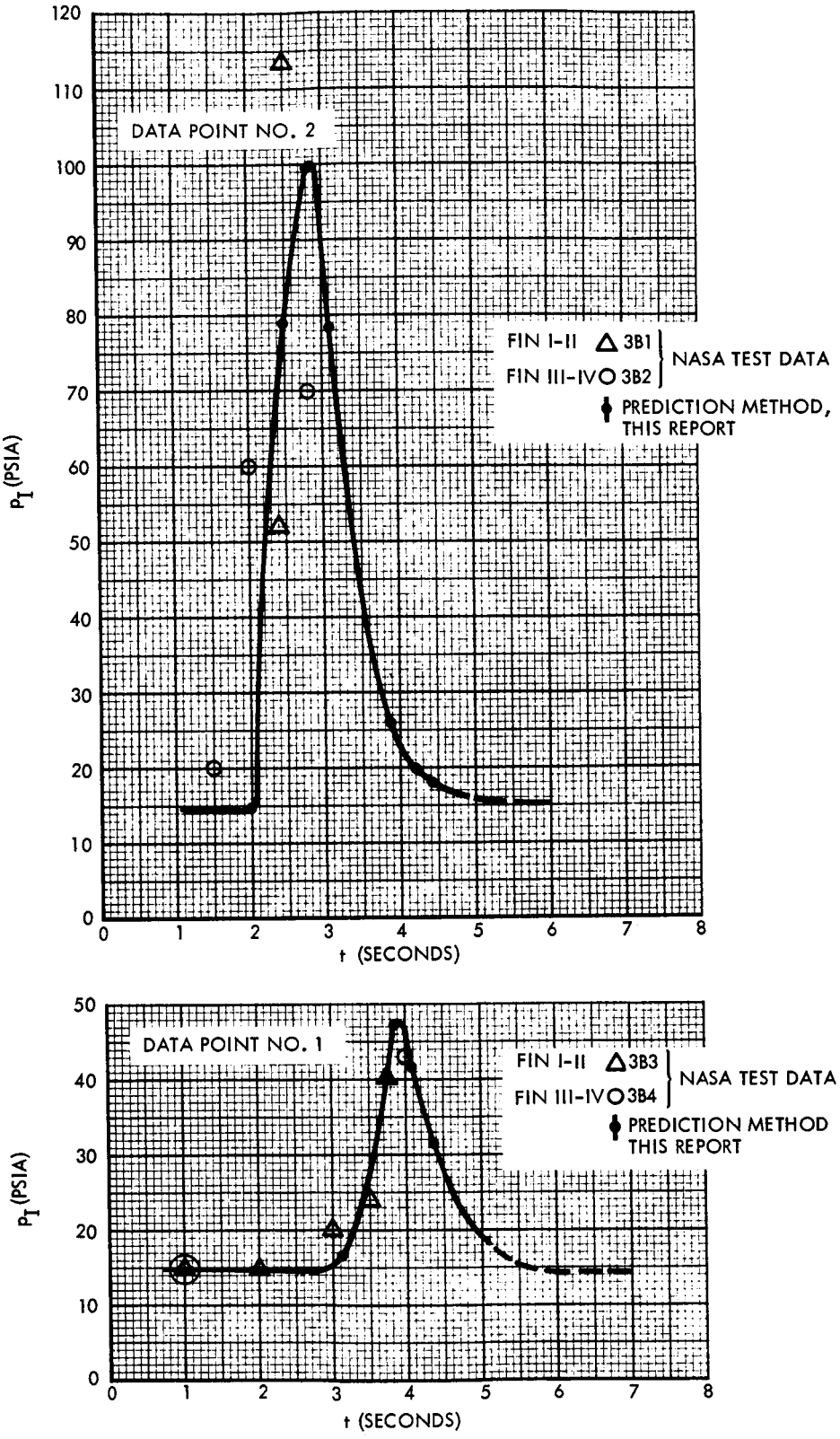

Figure 26. Correlation of Predicted Impact Pressures with SA-5 Launch Test Data

C. SPECIAL IMPINGEMENT PRESSURE EFFECTS

1. Turbulent Flow Effects

The maximum normal pressure predicted by Equation 50 with $\theta_I = 90°$ is the stagnation pressure corresponding to the plume velocity before impingement. With the local, or ambient, pressure added, the total stagnation pressure, p_s, should be from the kinetic theory of gas pressure:

$$p_s = \frac{\rho_s V_m^2}{3} \tag{52}$$

where ρ_s is mass density, and V_m, the randomly directed molecular velocity under stagnation temperature conditions.

In view of the good correlation obtained with the simple Newtonian Impact Theory, apparently negligible deviations occur from assumption of complete conversion of the gas transport velocity before impingement; yet a substantial gas transport velocity continues to exist beyond the small stagnation area region. A primary toroidal vortex and subsequent eddy flows must be considered to establish accurate local-flow fields. Centrifugal and centripetal forces probably adjust to maintain the basic stagnation pressure due to rate of change of the plume momentum. A study of these effects could be helpful in accounting for deviations from the simple impact pressure prediction theory in certain special cases and also from the heat transfer rate prediction theory, which is presented in Section V.

2. Radiation Impingement Effects

For the correlation of relatively gross pressures in the cases discussed in Section IVB, the small pressure resulting from momentum transfer during the photon impingement of radiation is easily shown to be negligible. The pressure due to solar radiation at the earth's distance is about 4.5×10^{-5} dynes/cm^2 (Reference 28) which converts to 9.4×10^{-8} lb/ft^2. The corresponding solar radiation is about 0.123 Btu/ft^2 sec. The radiation intensity from the high-temperature shock layer after impingement of a rocket jet plume may be about 1500 times greater, but the related ~~solar~~ radiation pressure is still negligible. However, the extreme environmental conditions of the exhaust plumes of plasma and photon rocket engines of the future could result in appreciable impingement pressure levels, due to this effect.

Aside from including this reference to radiation pressures to show that they are, at present, negligible, this study has provided support for a new concept (Section V-D) of the useful empirical relationship between heat transfer rates and the gross impingement pressures.

V. HEAT TRANSFER DUE TO JET PLUME IMPINGEMENT

A. RADIATION FROM NONIMPINGING PLUMES[1]

The objective has been to develop a general engineering method for the prediction of total radiant power incident upon a surface element from an axisymmetric exhaust plume whose composition and properties can be specified. Subsection A1 describes a method applicable to plumes containing only molecular radiators and presents numerical results for two cases; a typical storable propellant engine operating at high altitude, and the sea-level plume of the Saturn vehicle. Subsection A2 discusses the status of work on methods of evaluating radiation from plumes containing solid particles.

1. Radiation from Molecular Constituents

The principal source of radiation from gaseous exhaust plumes are vibrational - rotational transistions from heteronuclear, diatomic, and polyatomic molecules. In principle, it is possible to compute the complete absorption spectrum for all lines of all bands of each gas constituent present in the rocket exhaust. Approximate methods have been developed that avoid detailed consideration of the rotational structure of infrared spectra. The method adopted here is one of the simplest (although not necessarily the least accurate) and is based upon the concept of effective band width (Reference 29) and is similar in many respects to that described in Reference 30.

Each band can be characterized by an integrated absorption representing the total absorption of the band per unit length and per unit concentration of absorbing molecules integrated over wave number. The customary units of absorption are $cm^{-2}atm^{-1}$ where atmosphere in this case represents the molecular concentration corresponding to 1-atmosphere partial pressure and 273.16°K.

An effective bandwidth $\Delta\nu$ can be defined as being the wave number range occupied by lines having an absorptivity greater than some small fraction of the strongest line. Approximate theory (Reference 30) shows that bandwidth varies as the square root of the absolute gas temperature. The actual band absorption may then be approximated by a (uniform) average

[1] This section is a summary of the study made by Dr. E. P. French, of the Gas Dynamics group, S&ID Space Sciences Laboratory, in support of the Power and Environmental Systems program.

absorption coefficient extending over the effective bandwidth and so adjusted that the product of average absorption and bandwidth is equal to the integrated absorption, α.

Within the framework of the above approximation, the total absorption coefficient for a gas mixture may be expressed as the sum of the coefficient of all bands which include that wave number. Thus

$$\mu(\nu) = \Sigma \mu_i \tag{53}$$

$$\mu_i = \frac{\left[\alpha_i \left(\frac{p}{p_o}\right) N_i\right]}{\Delta \nu_i \left(\frac{T}{T_o}\right)} \tag{54}$$

$$\Delta \nu_i = \Delta \nu_{300} \sqrt{T/300} \tag{55}$$

If radiation originates from, or passes through, a radiating gas, its intensity may be evaluated by integrating the equation of radiative transfer along the optical path from source to sensor. For the case where local thermodynamic equilibrium exists within the gas, this transfer equation can be written:

$$\frac{dI}{dX} = -\mu (I-B) \tag{56}$$

where B is the Planck function at the local gas temperature.

Equation 56 can be integrated over a path thickness ΔS in which temperature and composition can be considered constant, to give

$$I_2 = B\left[1 - \exp(-\mu \Delta S)\right] + I_1 \exp(-\mu \Delta S) \tag{57}$$

For the general case of a gas with large property gradients, Equation 57 may be applied successively to small length increments along the optical path, within which property variations are small.

(a) Plume Geometrical Relationship

In order to evaluate the radiant intensity reaching a surface element from a given direction, it is convenient to work with two coordinate systems

shown in Figure 27. The integration of the equation of radiative transfer through the plume is carried out along lines of sight whose orientation is specified with respect to a reference plane defined by the position of the surface element, P, and the plume axis in Figure 27(A). Direction is given in terms of an azimuth angle θ measured from the rearward axial direction in the reference plane and an elevation angle ϕ measured perpendicular to the reference plane. Distance, S, along the line of sight defines a particular location, F, in the plume.

The same system is used to define the orientation of the surface element at point, P, in terms of the directional coordinates, θ_r and Φ_r, of its normal.

The temperature, pressure, and composition of the plume from which the radiative characteristics of the plume are determined, are most conveniently described in terms of x_p and R, the axial and radial coordinates depicted in Figure 27(B). These are related to the previously-described coordinates by

$$x_F = x_p + S \cos \Phi \cos \theta \tag{58}$$

$$R^2 = S^2 \sin^2 \Phi + R_o^2 - 2R_o S \cos \Phi \sin \theta + S^2 \cos^2 \Phi \sin^2 \theta \tag{59}$$

The spectral intensity I_ν reaching a given point in space from a given direction may be obtained by successively applying Equation 57 over small length increments along the line of sight from the far to the near boundaries of the plume. The plume properties (assumed constant over each length increments, ΔS) must be known as a function of radial R and X position in order that the appropriate spectral absorption coefficients may be calculated.

The total radiant power-per-unit area reaching a surface element from the plume is given by

$$P = \iint \left[\sin \Phi_r \sin \Phi + \cos \Phi_r \cos (\theta - \theta_r) \right] \left[\int_o^\infty I_\nu \, d\nu \right] \cos \Phi \, d\Phi \, d\theta \tag{60}$$

where the inner integral gives the contribution per-unit solid angle from a given direction and the first bracketed term corrects for nonnormal incidence. The integration over θ and ϕ covers the entire solid angle subtended by the plume.

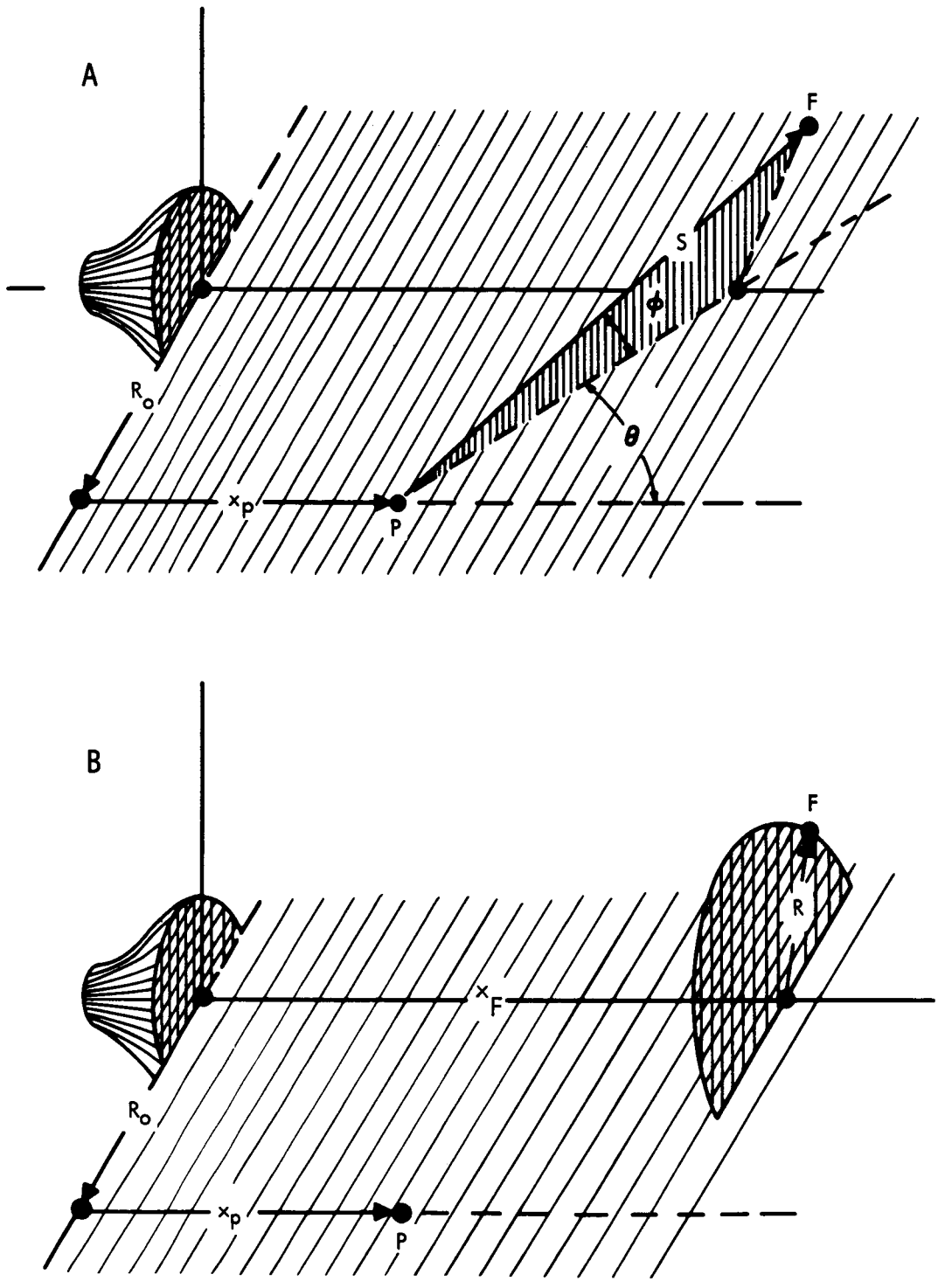

Figure 27. Plume Coordinate Systems for Radiation

(b) Numerical Calculations for High-Altitude Plumes

The above equations have been incorporated into a Fortran II digital computer program (REDJET) which is an extension of programs described in Reference 31. Representative calculations have been carried out for a typical storable propellant rocket, the main propulsion engine of the Apollo service module. The plume geometry and exhaust composition were held fixed, but a range of plume exit conditions, nozzle diameters, element locations, and element orientations were considered. A total of 220 cases were calculated.

Mach number distribution in the service module plume under vacuum conditions was available from method-of-characteristics solutions carried out at S&ID. The distribution was found to approximate closely the expression

$$M_F = \frac{2.06\left[\left(\frac{R_F}{R_e}\right)^2 - 1\right]}{\left(\frac{x_F}{R_e}\right)} + 0.206\left(\frac{x_F}{R_e}\right) + 5.26 \qquad (61)$$

except in the far plume, where the radiation is negligible, and very near the nozzle exit where conditions can be taken equal to those at the exit with small error. Equation 61 was used in making the radiation calculations. Plume properties are summarized in Table 10.

Table 10. Approximate Plume Gas Properties

Nozzle Exit Conditions	
Static Temperature (°K)	840.
Static Pressure (atmosphere)	0.00672
Specific Heat Ratio	1.30
Mach Number	4.75
Composition (mole fractions)	
CO	0.03637
NO	0.00502
OH	0.00692
CO_2	0.09035
H_2O	0.41547

Static properties throughout the plume were computed from plume Mach number (Equation 61) from the isentropic flow equations for a perfect gas.

The integrated absorption values and effective band widths used in the computation were taken from Reference 30 and are tabulated in Table 11.

The effects of plume temperature, pressure, and nozzle size (scale) were evaluated for a common element location in the exit plane ($x_p/R_e = 0$) and 10-nozzle radii from the axis ($R_o/R_e = 10$). Figure 28 shows the variation of power received as a function of nozzle-exit temperature, for an element whose normal lies in the reference plane ($\phi_r = 0$) and is perpendicular to the nozzle axis ($\theta_r = 90°$). However, power is approximately proportional to the fourth power of the exit temperature although the spectral emission is considerably different from the blackbody distribution and gas temperature varies throughout the plume.

Figure 29 shows the variation of power received as a function of the product of exit pressure and nozzle radius (a measure of the size of the plume) for the same element location and orientation. Power is approximately proportional to $(P_e/P_o)\ R_e$. The nonlinearity may be due in part to self-absorption and in part to plume nonuniformity.

Table 11. Band Characteristics (at 300°K)

Molecule	Band Frequency ($-cm^{-1}$)	Integrated Absorption ($cm^{-2}\ atm^{-1}$)	Effective Band Width (cm^{-1})
CO	2114	273.0	214
	4152	1.64	213
NO	1876	63.0	225
	3680	2.1	225
OH	3568	100.0	747
	6971	4.0	747
CO_2	2349	2706.0	106
	667	240.0	106
	3716	42.3	106
	3609	28.5	106
	721	7.5	106
	4984	1.01	106
H_2O	1590	175.0	430
	3700	126.0	430
	500	58.4	430
	5350	10.1	430
	7250	8.3	430
	9091	0.32	430

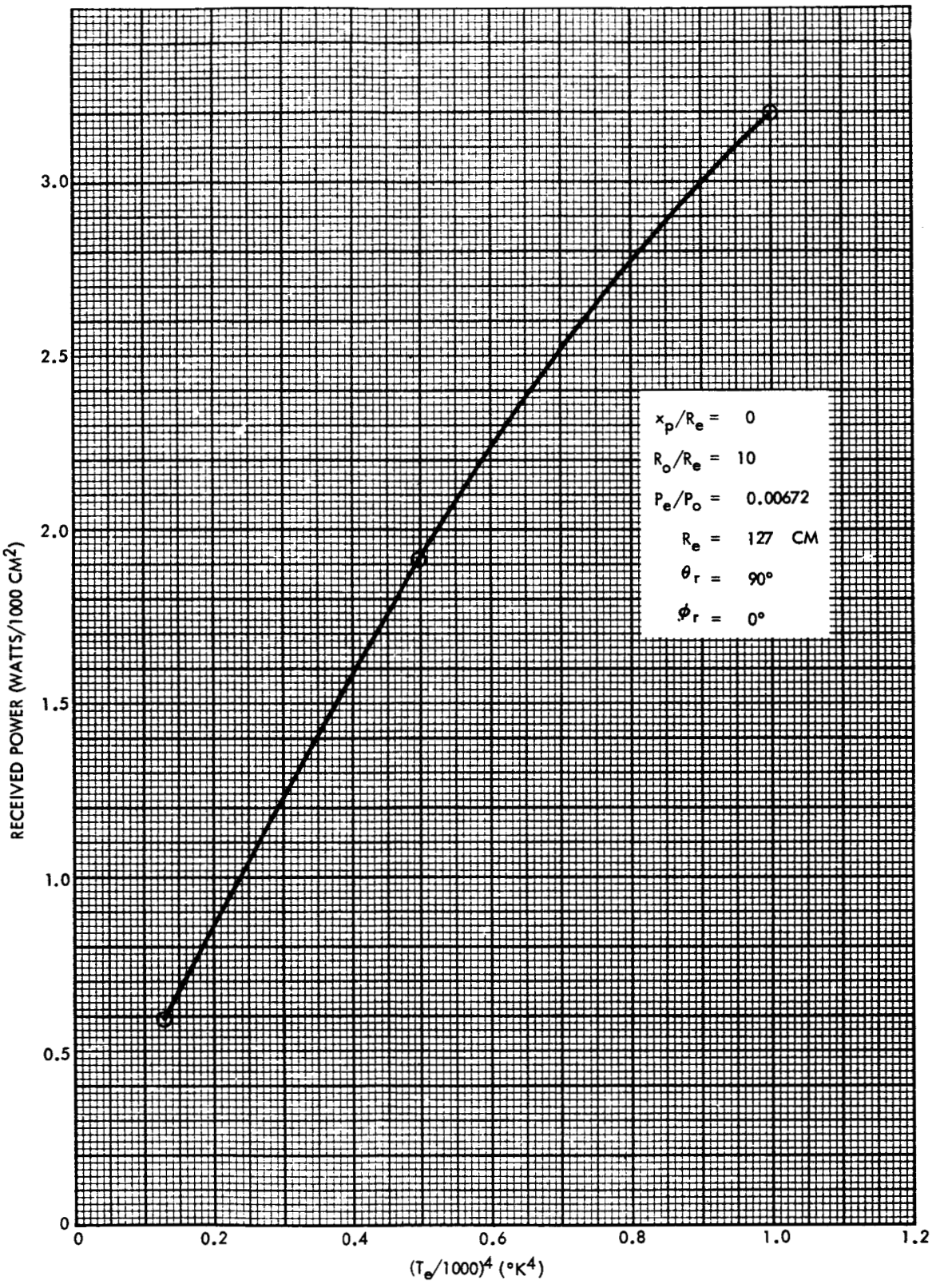

Figure 28. Effect of Temperature on Received Power

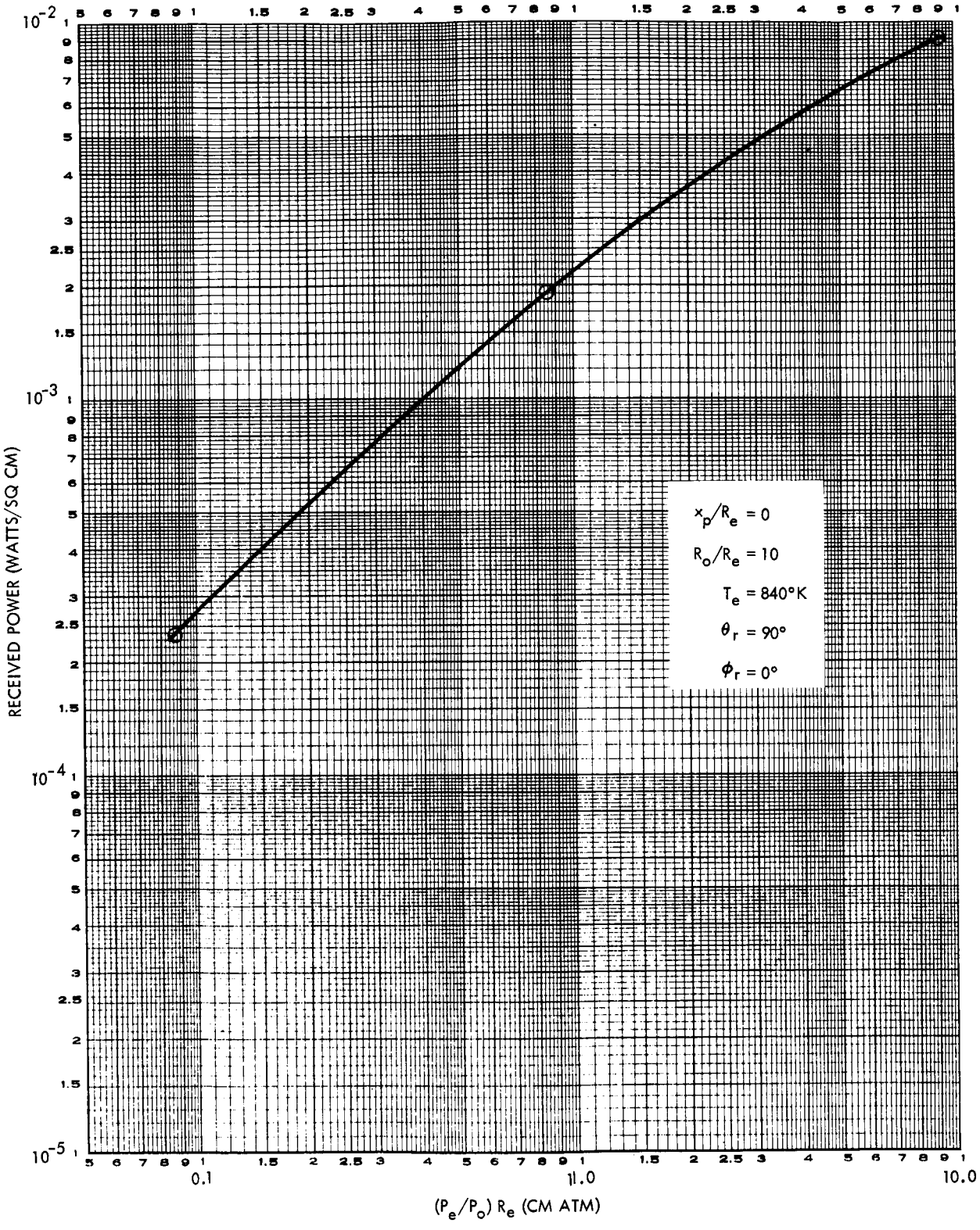

Figure 29. Effect of Pressure and Scale on Received Power

Figure 30 shows the variation in received power due to orientation for an element located at the nozzle lip($x_p = 0$; $R_o/R_e = 1$. In this position appreciable radiation is received over a considerable range of element orientations. Similar calculations were carried out for other element locations. It was found that for elements farther than 10 radii from the axis, the plume could be represented (approximately) by an effective point source located on the axis 2-nozzle radii downstream of the exit plane. This fact, together with the temperature, pressure, and scale variations discussed above, suggests the following approximate expression for the received power at intermediate and large distances:

$$P = \frac{K\sigma T_e^4 \left(\frac{p_e}{p_o}\right) R_e \cos\phi_r \cos(\theta_r - \theta^*)}{\frac{R_o^2}{R_e^2} + \frac{(x_p - \Delta)^2}{R_e^2}} \qquad (62)$$

where

K is a function of plume shape and composition
θ^* is the azimuth angle from element to effective point source
Δ is the downstream axial distance of effective point source

The quantity K was evaluated for all surface locations where $R_o/R_e \geq 10$ and for all orientations lying within 60° of the θ^* direction. The K variations are summarized in Table 12.

Table 12. Radiation Correlation

R_F/R_e	x_p/R_e	T_e(°K)	p_e/p_o	R_e(cm)	K(cm^{-1})
10	0	840	0.00672	127	0.0831 - 0.0889
50	0	840	0.00672	127	0.0911 - 0.0947
10	10	840	0.00672	127	0.0977 - 0.1061
10	50	840	0.00672	127	0.1284 - 0.1288
10	0	1000	0.00672	127	0.0703 - 0.0723
10	0	600	0.00672	127	0.0959 - 0.1109
10	0	840	0.00672	127	0.0976 - 0.1063
10	0	840	0.06720	127	0.0385 - 0.0392

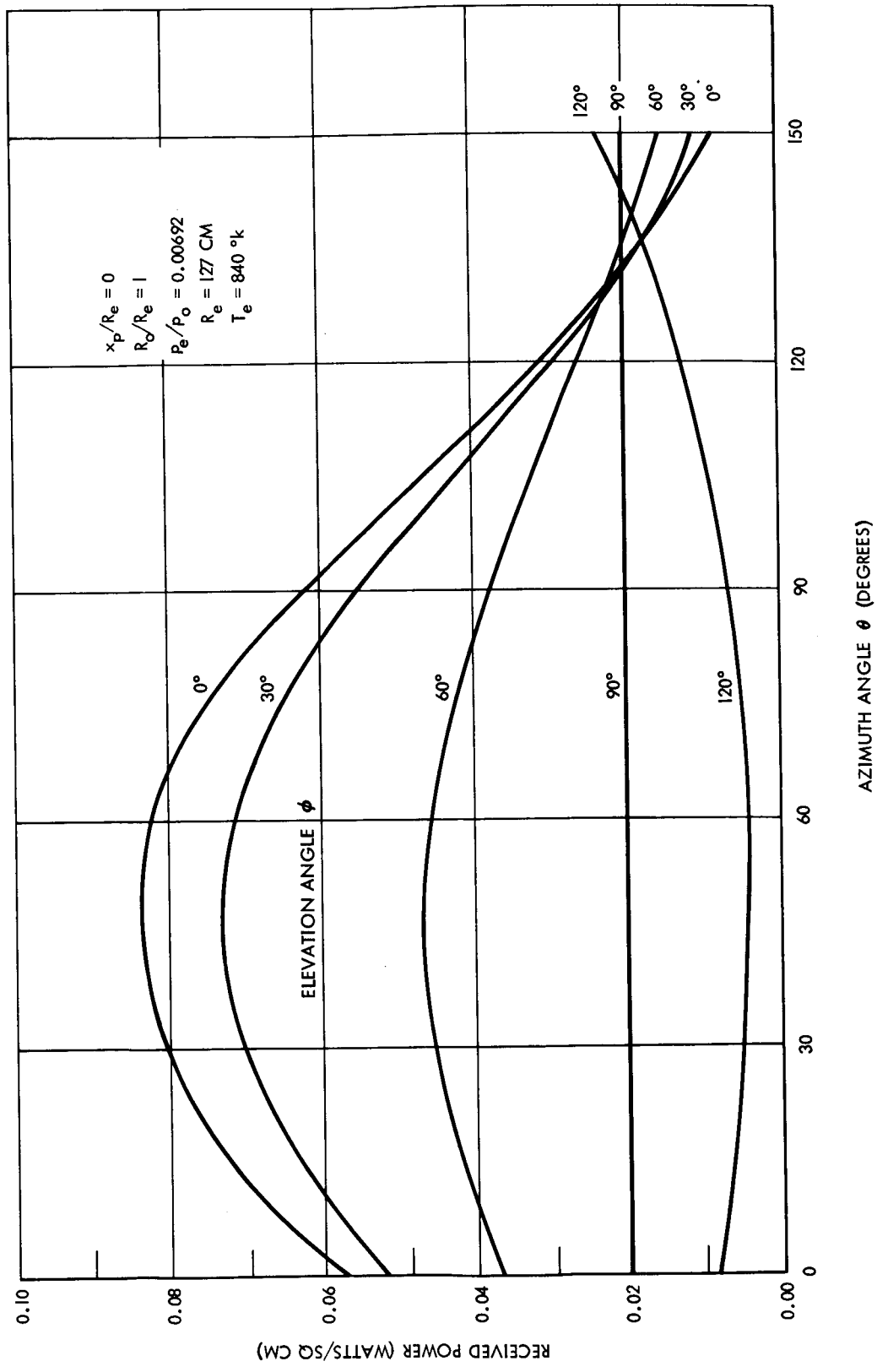

Figure 30. Effect of Element Orientation on Received Power

Except for the last line of data in Table 12 where the increased pressure would be expected to give lower radiant power due to self-absorption, the variation of K is not large. This indicates that Equation 62 would be useful for making rough estimates once a few detailed calculations had established the value of K and Δ.

(c) Molecular Radiation from Low-Altitude Plumes

At high altitudes and in space, the exhaust plume may be considered isentropic and nonreacting. Hence composition can be assumed constant and temperature and pressure may be simply computed from the local Mach number. Moreover, the Mach number can often be represented by a simple analytical function of axial and radial location (Equation 61), thus yielding a fairly compact representation of plume properties.

At low altitudes, these simplifications are no longer valid. The core of the plume will, in general, contain a series of expansion and compression shocks across which gas properties change discontinuously. Moreover, there may be large composition changes due to reaction between the fuel-rich exhaust and the entrained atmosphere (afterburning).

Instead of the relatively simple analytical expressions applicable to high altitude plumes, therefore, the more general expressions must be used.

$$T = T(x, R) \tag{63}$$

$$P = P(x, R) \tag{64}$$

$$N = N(x, R) \tag{65}$$

In machine computation, Equations 63, 64, and 65 would be represented by tabulated data with associated interpolation subroutines. In principle, however, the calculation of absorption coefficients proceeds exactly as in the case of the high altitude plume. The real difficulty is encountered in specifying the functions T, P, and N.

(d) Estimated Radiation Heating During Saturn SA-5 Launch

The method described in subsections (a) and (b) were used to make representative calculations of radiant heat transfer during sea-level launch of the Saturn vehicle. As described in Section V (C-4 and 5) total heat transfer measurements made on the launch structure are available and may be compared with analytical predictions of radiative and convective rates.

The instrumented location chosen for initial radiation calculations was designated Data Point No. 2. The procedure employed was to calculate heat transfer from the nearest engine plume only, and to multiply this by a factor estimated from the additional solid angle subtended by the other plumes and the assumption that each plume is optically thick. The relevant geometrical factors for three different launch times were as follows:

Time from launch (seconds)	2.0	2.8	3.8
Axial location (x/R_e)	9.2	20.3	35.1
Radial location (R/R_e)	1.1	0.0	1.6
Factor (for multiplume estimate)	1.0	1.0	2.0

Calculations were made using the program REDJET and the subprogram REDRAD. These programs were modified to accommodate the special features of a low-altitude plume.

Properties were handled in the following way; temperature was taken constant at any axial station and assumed to vary linearly with axial station, composition was taken to be constant within the plume and submicroscopic carbon particles were added as an additional constituent. The properties assigned at two axial stations were as follows:

Axial station (x/R_e)	0	50
Temperature (°K)	1670	1390
Pressure (atmosphere)	1	1
Plume Radius (R/R_e)	1	1.5
Gas composition (mole fraction):		
H_2O	0.38	0.38
CO	0.38	0.38
CO_2	0.12	0.12
Carbon concentration (assumed weight fraction)	0.01	0.01

The resulting radiant heat transfer rates were as follows:

Radiant Heat Transfer at Instrument Data Point No. 2:

Time from Launch (seconds)	2.0	2.8	3.8
Heat Transfer (Btu/ft^2-sec) Single Plume	12.7	21.4	9.8
Multiplume (estimated)	12.7	21.4	19.6

2. Radiation from Particle-Laden Plumes

Although radiation from particles generally has a simpler spectral dependence than that from molecular radiators, the overall problem of evaluating the contribution due to solid (or liquid) particles in an exhaust plume is very difficult. First, the radiative characteristics of individual particles must be determined as a function of wavelength and of particle size and temperature. Next, the net effect of a cloud of such particles (not necessarily uniform in size, concentration, or temperature) must be evaluated, considering both absorption and scattering of radiation. Finally, and perhaps the most difficult, the actual particle size distribution, concentration and temperature must be predicted as functions of plume location for a given rocket engine. The principal solid or liquid constituents in rocket plumes are carbon, resulting from the incomplete combustion of hydrocarbons, and the oxides of aluminum and magnesium which are equilibrium products for many solid propellants.

(a) Cross Sections for Carbon Particles

Stull and Plass (Reference 32) have computed the absorption, scattering, and total cross sections of spherical carbon particles, using the Mie scattering theory. They considered particle radii from 50 to 1000 A, the expected range for carbon particles in flames according to review of available measurements. Although the expressions for cross sections are quite complex, the resulting values can be represented fairly simply for wavelengths which are large compared to particle radius. Fortunately, this covers the spectral region from which most of the radiant energy is emitted at typical plume temperatures. The cross sections are

$$\sigma_s = 1.12 \times 10^{-4} \, r^6 \, \lambda^{-4} \tag{66}$$

$$\sigma_t \approx \sigma_a = 6.05 \times 10^{-7} \, r^3 \, \lambda^{-2} \tag{67}$$

The cross sections are in square centimeters, and radius and wavelength are in microns.

In the range where they apply ($r < 0.1\mu$, $\lambda > 1.0\mu$), Equations 66 and 67 have two important consequences; first, absorption is the dominant extinction mechanism and scattering can be ignored for most engineering purposes, and secondly, the product $N\sigma_t$, where N is the volume concentration of particles in a cloud, is proportional to $N\ r^3$ and thus to the mass density of particles. Thus $N\sigma_t$, which is essentially a volume absorption coefficient, is independent of particle size and size distribution.

(b) Cross Sections and Emmisivities of Oxide Particles

The aluminum and magnesium oxide particles observed in solid propellant exhausts range in size from less than a micron to several microns in radius (References 33, 34, and 35). Thus the spectral variation of radiation cross sections is more complicated than for the much smaller carbon particles. Typically, the total or extinction coefficient, σ_t, at a given wavelength increases monotonically with particle radius r_p, for particles small compared with the wavelength. For particles having radii greater than about one-third wavelength σ_t oscillates about the value $2\pi r_p^2$, finally damping out at large radii. Reference 34 gives total and absorption cross sections for Al_2O_3 and MgO particles over a range of sizes and wavelengths.

In an analysis, Morizumi and Carpenter (Reference 33) simplify this complicated behavior by assuming the constant asymptotic value $2\pi r_p^2$ for the extinction coefficient which represents a rough average to the actual values for particles in the micron range and is probably a reasonable choice since particle size and size distribution are not accurately known.

Current knowledge of Al_2O_3 and MgO particle emissivities, which can be derived from the absorption and total cross sections, is uncertain at present. Typical values derived from the cross sections computed by Plass (Reference 34) are less than 0.1 but later work by the same laboratory (Reference 35) indicates that these values are too low for particles at plume temperatures and that emissivities probably lie in the range 0.2 to 0.4. In Reference 33, the value 0.25 is adopted, based upon an analysis of radiation from actual rocket exhausts.

(c) Gas-Particle Nozzle Flow

There have been a number of numerical studies of the behavior of two-phase flow in rocket nozzles and isentropic plumes. The results of these calculations are presented in References 33, 36, and 37. In general,

the velocity and temperature history of the particles are computed from the drag and heat transfer exerted by the gas stream.

In all the references cited, the calculations are based upon the assumption of spherical particles. Drag and heat transfer are evaluated in the flow regime where viscous behavior predominates (Stokes flow). References 33, 36 and 37 include corrections for rarefaction effects, and in addition, Reference 37 employs corrections for compressibility and inertial effects which can be important for large particles and large relative velocities.

No similar computer program is available at S&ID, and it was not within the scope of the present study to develop one. As an alternative, the numerical results of detailed calculations have been correlated to provide engineering expressions useful for the estimation of the radiative properties of gas-particle clouds.

(d) Solid Particle Velocity Lag Correlation

In general, the axial velocity of a particle will lag the velocity of the gas stream during acceleration through the nozzle and in the external plume. The amount of this lag depends upon nozzle shape and size, particle size and density, and gas properties. Since carbon particles are found to be very small, only Al_2O_3 and M_gO particles in the micron range are likely to exhibit appreciable velocity lag. The densities of the latter two are fairly close so that, in practice, only particle size need be considered. Again, it is reasonable to expect that nozzle contours, gas composition, and temperature variation through the nozzle will be similar for modern solid propellant rockets. Thus, as an approximation, the significant variables are nozzle scale and axial distance along the nozzle.

The velocity lag $1 - K$, (where $K = V_p/V_g$) can be successfully correlated with the parameter $r_p(r^*)^{-1/2} Z^{-1/4}$ where r_p, r^*, and Z represent the particle radius in microns, the nozzle throat radius in centimeters, and the axial distance downstream of the throat in centimeters, respectively. This correlation is shown in Figure 31 where it is obvious that there is considerable difference between the curve which includes corrections for inertial and compressibility effects and that which includes only rarefaction effects.

(e) Solid Particle Temperature Lag Correlation

An examination of the numerical predictions for particle temperature lag $(T_p - T_g)/T_{go} - T_g)$, where T_{go} is the gas temperature in the combustion chamber, shows that lag reaches an asymptotic value within the diverging portion of the nozzle and remains essentially constant thereafter. Thus, the value of the temperature lag at the nozzle exit is apparently not sensitive to nozzle length. In fact, a reasonable satisfactory correlation of the data from References 36 and 37 can be made using particle radius alone (Figure 32).

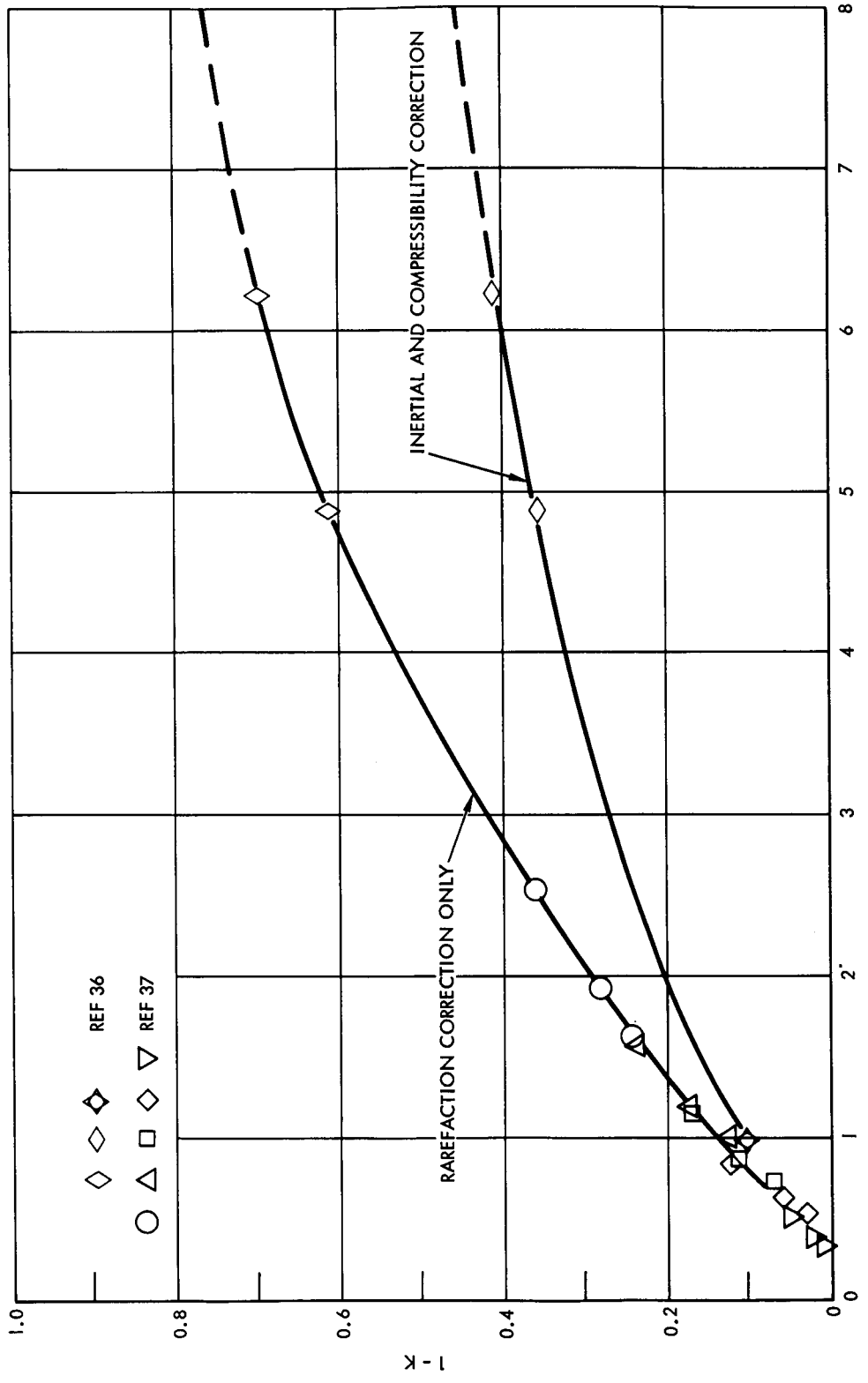

Figure 31. Solid-Particle Velocity-Lag Correlation

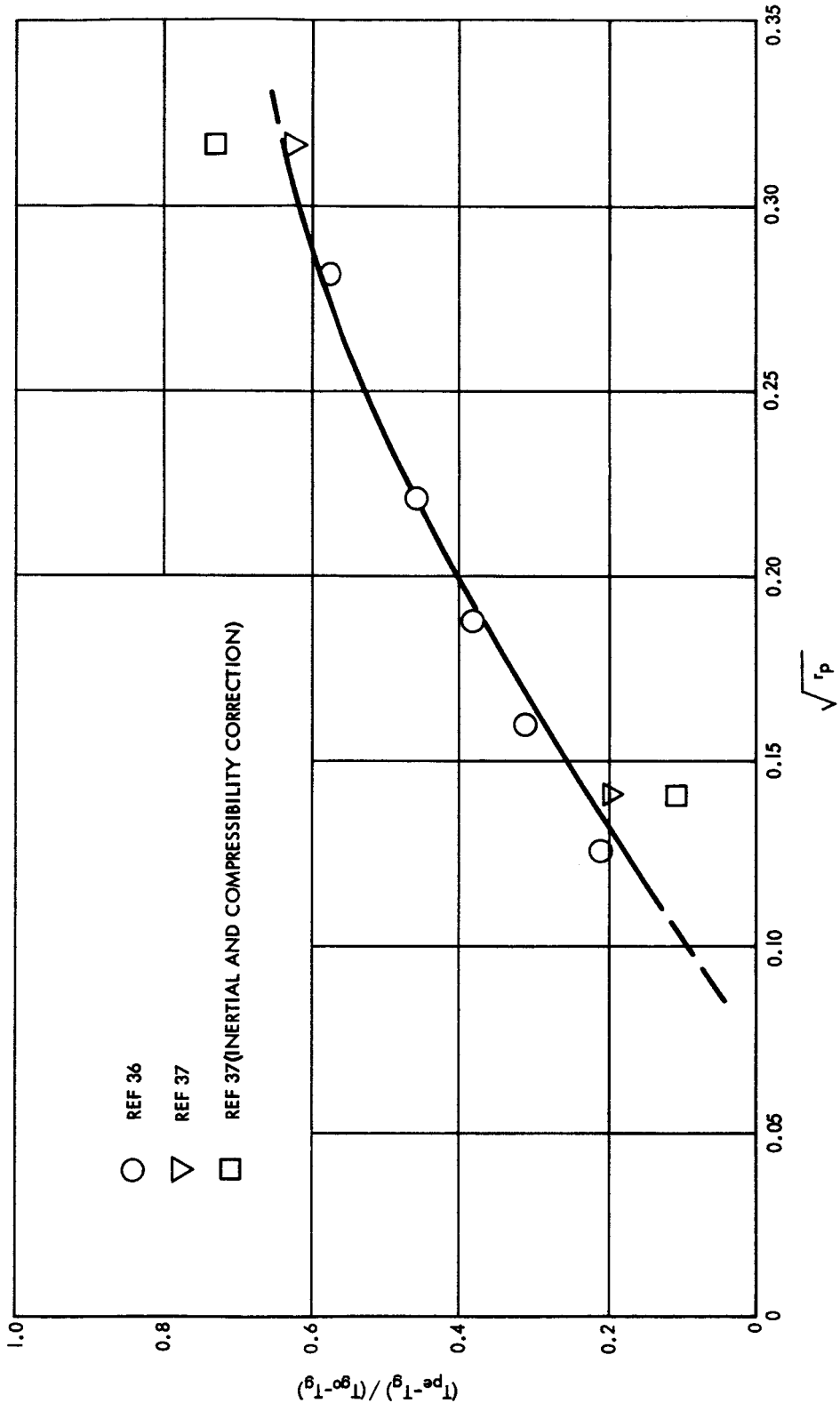

Figure 32. Solid-Particle Temperature-Lag Correlation

Unlike the situation with the velocity lag, there is no consistent trend identified with the consideration of inertial and compressibility effects. It should be noted that the apparent lack of influence of nozzle scale is based on the data used in Figure 32 which covers nozzle radii from 1.5 to 3.5 centimeters. For much larger nozzles, the temperature lag at the exit must certainly be less than the correlation indicates.

(f) Particle Concentration Correlation

As Kliegel (Reference 36) points out, particles tend to travel in straight lines in the diverging portion of the exit nozzle and in the plume, and in fact, exhibit conical flow regardless of nozzle contour. This observation is used as the basis for an approximate method of specifying particle concentrations in the plume.

Assume that particles in the plume are confined to a cone centered on the nozzle axis whose half angle θ_L is determined by the limiting streamline for a particular size. Assume further that the particle concentration, N_p, is constant in magnitude and directed along streamlines from the apex , as shown in Figure 33.

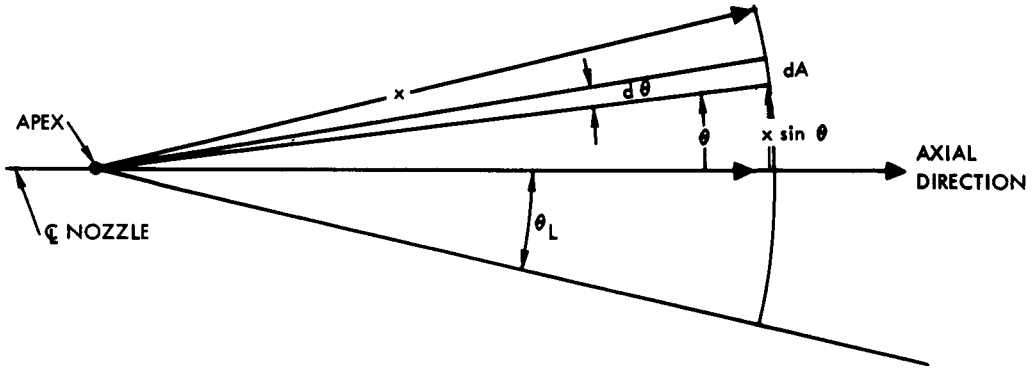

Figure 33. Relationships for Radial Particle Flow

Under these circumstances, the particle mass flow, $\dot{M}_p$, through any surface x = constant can be found as follows:

The spherical surface area, A, enclosed by the limiting streamlines θ_L is found by integrating an annular element $dA = 2\pi (x \sin \theta) \times d\theta$ from $\theta = 0$ to $\theta = \theta_L$.

$$A(x) = 2\pi x^2 \int_0^{\theta_L} \sin\theta \, d\theta = -2\pi x^2 (\cos\theta_L - 1)$$

$$= 2\pi x^2 \left[1 - \left(1 - \frac{\theta_L^2}{2!} + \ldots. \right) \right]$$

$$= \pi x^2 \theta_L^2, \quad \theta_L \ll 1 \tag{68}$$

For $\theta_L \ll 1$ the spherical surface x = constant is essentially a plane surface at Z = x. Thus

$$A(x) \approx \pi Z^2 \theta_L^2 \tag{69}$$

The particle mass flow is the product of mass density of particles, particle velocity, and the area. Thus

$$\dot{M}_p = \frac{4}{3} \pi r_p^3 \rho_p N_p V_p \pi Z^2 \theta_L^2 \tag{70}$$

From Equation 70, the particle number density becomes

$$N_p = \frac{\dot{M}_p}{\frac{4}{3}\pi^2 \rho_p V_g} \left[\frac{1}{r_p^3 K Z^2 \theta_L^2} \right] \tag{71}$$

The term in brackets depends upon the particle size and nozzle geometry. The particle velocity may be taken as the value at the nozzle exit and is obtainable from the gas-exit velocity through Figure 31. Limiting streamline angle θ_L may also be correlated with particle size as shown in Figure 34. θ_L varies inversely with the square root of the particle radius until it exceeds the nozzle half-angle, after which it remains roughly constant.

No published calculations of plume-particle concentrations have been found in which sufficient information is included to allow a direct test of Equation 71. However, Reference 33 presents calculated concentration distributions for two particle sizes, 0.79 and 3.95 μ, which are assumed to have equal mass fractions in the exit flow. Thus the term outside the bracket in Equation 71 is constant, and N should vary inversely with $r_p^3 K Z^2 \theta_L^2$. Figure 35 shows that the calculated concentrations obey this relation fairly closely.

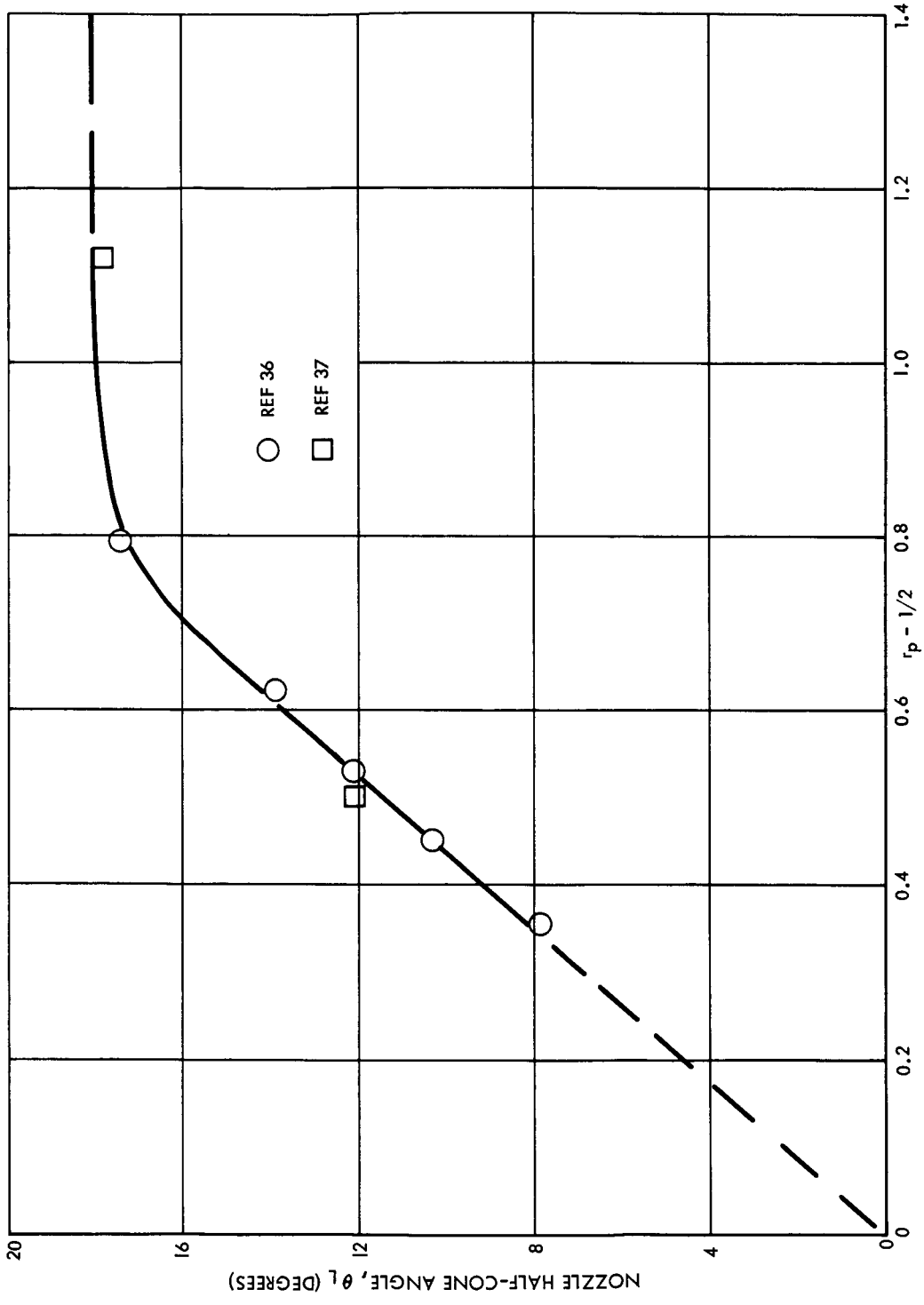

Figure 34. Limiting Particle Streamline Correlation

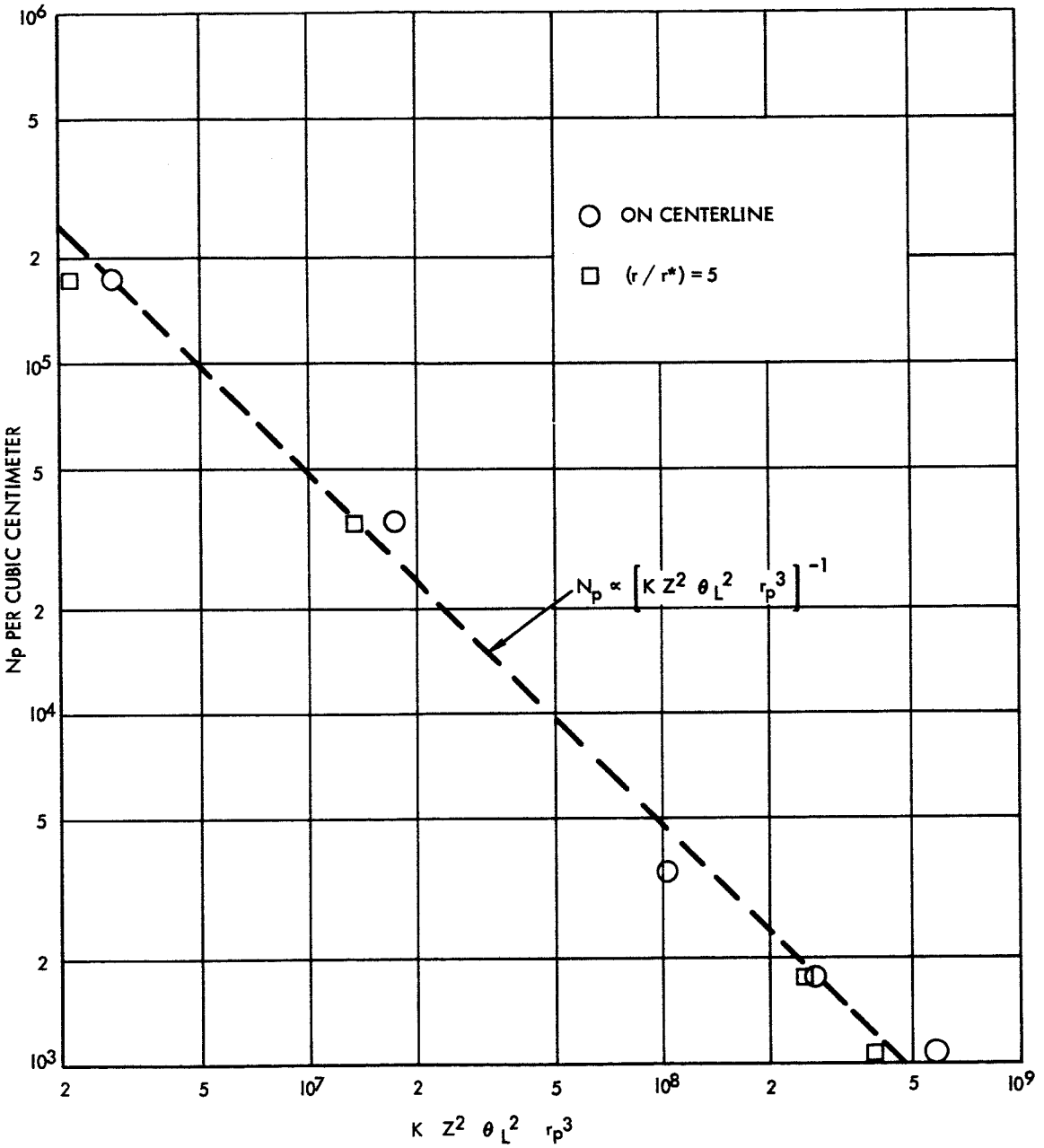

Figure 35. Particle Concentration Correlation

(g) Radiative Transfer from Submicroscopic Particles (Carbon)

Because of the small size ($r_p < 1000$ A) and high emissivity typical of carbon particles in a rocket exhaust, two important simplifications can be introduced. First, scattering of the radiation from one particle by adjacent particles can be ignored and the simple expression

$$I(\lambda) = B(\lambda, T)\left[1 - \exp(-\sigma_t N_p S)\right] \tag{72}$$

gives the intensity received by a surface element (normal to the line of sight) from a uniform cloud of particles S-units thick and having particle cross section σ_t and concentration N_p per unit volume. (See Equations 25, 26, and Reference 32.) From Equation 67 and the formula for the mass of a sphere of radius r_p

$$\sigma_t N_p = \frac{6.05 \times 10^5}{\lambda^2} \cdot \frac{3}{4\pi\rho_p} = \frac{1.45 \times 10^5 \, W_p}{\lambda^2 \rho_p} = \mu_p \tag{73}$$

Thus the particle cloud can be considered to nave an effective absorption coefficient, μ_p, which is proportional to the mass concentration of carbon W_p (in grams per cubic centimeter) and inversely proportional to the wave length (in microns). For a nonuniform cloud, the difference form of Equation 72 should be employed:

$$I_2 = B\left[1 - \exp(-\mu_p \Delta S)\right] + I_1 \exp(-\mu_p \Delta S) \tag{74}$$

Secondly, the correlations described previously show that submicroscopic particles are, for practical purposes, in equilibrium with the gas stream; and their velocity, temperature, and concentration can be treated in the same manner as molecular constituents.

(h) Radiative Transfer from Micron-Sized Particles (Al_2O_3, MgO)

Morizumi and Carpenter (Reference 31) have carried out calculations, including the effects of scattering, of radiative heat transfer from Al_2O_3 particles. They make the assumption that the total cross section is a constant, $2\pi r_p^2$, thus making it possible to work with total rather than spectral intensities. They compute apparent emissivity ϵ_A for two particle geometries, an infinite slab, and an infinite cylinder. Both yield the same

limiting value of apparent emissivity $\epsilon_A = \epsilon_p^{1/4}$ when the optical thickness $\tau = N_p \sigma_t L$ is very large. L is the thickness of the slab or diameter of the cylinder. At small τ

$$\epsilon_A = \frac{2}{3} \epsilon_p \tau \text{ (for a cylinder)}$$

$$\epsilon_A = 2 \epsilon_p \tau \text{ (for a slab)}$$

At all values of τ, their results can be represented fairly accurately by the expression

$$\epsilon_A = \epsilon_p^{1/4} \left[1 - \exp\left(-C \epsilon_p^{3/4} \tau\right) \right] \tag{75}$$

where C equals 2/3 for a cylinder and 2 for a slab. The radiant heat transfer to a surface element from a small portion of the plume is given by

$$\Delta P = \Delta F \epsilon_A \sigma T_p^4 \tag{76}$$

where ΔF is the shape factor between the portion of the particle cloud in question and the element. The total radiant heat transfer is the sum of the individual contributions. No computer program has been developed at S&ID to apply Equation 76 to the geometry of an actual particle cloud of micron-sized particles. However, its use is straightforward provided the correct values of ϵ_A are available.

(i) Example

To illustrate the use of Figures 31, 32 and 34 and Equations 71, 75 and 76 to obtain radiant heat transfer, consider the following idealized case. The surface element in question is oriented so that its normal is perpendicular to, and passes through, the plume axis. Moreover, assume that the element is located at the edge of the plume and 40-nozzle throat radii downstream of the throat. Under these circumstances, the shape factor ΔF is unity and the plume properties to be used are those occurring at $Z = 40r^*$.

Assume an exit temperature of 1000°K, a chamber temperature of 3000°K, and gas exit velocity (at $Z = 10r^*$) of 3×10^5 centimeters per second, a nozzle-throat radius of 5 centimeters and a total mass flow of 5×10^4 grams per second of which 20 percent is made up of 3 micron Al_2O_3 particles.

The velocity lag parameter at the nozzle exit is

$$\frac{r_p}{(r^*)^{1/2}\, Z^{1/4}} = \frac{3.0}{5^{1/2}\,(5 \times 10)^{1/4}} = 0.50$$

from which 1 - K = 0.050 from the upper curve in Figure 31. (At larger values of the parameter the lower curve from Figure 31 is probably more accurate.)

The temperature lag at the exit is found to be 0.32 from Figure 32 at

$$\sqrt{r_p} = \sqrt{3} = 1.73.$$

$$T_p = t_g + (T_{go} - T_g) \times 0.32$$

$$= 1000 + (3000 - 1000) \times 0.32 = 1640°K$$

Since both drag and heat transfer are greatly reduced in the plume beyond the exit, due to rapid gas expansion, the exit values of temperature and velocity can be assumed approximately constant thereafter.

The limiting conical half-angle for the particle cloud in the plume (at $1 \sqrt{r_p} = 0.58$) is $\theta_L = 13.1°$ (Figure 34). Taking the particle density at the room temperature value, 3.85 grams per cubic centimeter, the particle concentration can be evaluated at $Z = 40r^*$ from Equation 71.

$$N_p = \frac{0.2 \times 5 \times 10^4}{\frac{4}{3}\pi^2 \times 3.85 \times 3 \times 10^5} \frac{1}{(3 \times 10^{-4})^3\,(1 - 0.050)\,(40 \times 5)^2 \left(\frac{13.1}{57.3}\right)^2}$$

$$= 1.22 \times 10^4 \text{ cm}^{-3}$$

(Note that r_p must be in centimeters and θ_L in radians in Equation 71.)

The optical thickness τ is proportional to the local diameter of the conical particle cloud.

$$L = 2 Z \tan \theta_L$$

$$= 2 \times 40 \times 5 \times 0.233$$

$$= 93 \text{ cm}$$

Thus

$$\tau = N_p \sigma_t L$$

$$= N_p \times 2 \pi r_p^2 L$$

$$= 1.22 \times 10^4 \times 2 \pi (3 \times 10^{-4})^2 \times 93$$

$$= 0.64$$

The effective emissivity can now be calculated from Equation 75. Taking $\epsilon_p = 0.25$ and $C = 2/3$ (for a cylinder)

$$\epsilon_A = 0.25^{1/4} \left[1 - \exp \left(-\frac{2}{3} \times 0.25^{3/4} \times 0.64 \right) \right]$$

$$= 0.099$$

The radiant power received is then obtained from Equation 76.

$$\Delta P = 1.0 \times 0.099 \times 5.66 \times 10^{-12} \times (1640)^4$$

$$= 4.1 \text{ watts/cm}^2$$

B. RADIATION FROM IMPINGEMENT SHOCK LAYER

During the investigation, it was found that predicted convection heat-transfer rates due to jet plume impingement on a canted side plate using a method developed in prior Apollo work were in satisfactory correlation with the experimental results obtained in a high-altitude test chamber (≈250,000 feet). The variables checked included nozzle area expansion ratio, impingement-plate side distance from the nozzle and its cant angle, plume and impingement distance downstream of the nozzle-exit plane, lateral displacement distance from the centerline of the impinged plate, and plate temperature. However, when the method was applied to the sea-level test data from the Saturn SA-5 launch, the predicted value of 224 Btu/ft^2 sec fell far short of the reported maximum measured value of about 1100 Btu/ft^2 sec for Data Point No. 2.

Since this prediction equation was adapted from the empirical results of prior hypersonic, aerodynamic, reentry heating investigations for satellites (velocity, 20,000 ft/sec and above) and also was designed to fit the different geometry of the Apollo RCS engine freestream flow and the canted side plate in the Tullahoma test setup, it was not surprising that the major change in the environmental conditions to those of a booster engine at sea level strained the applicable empirical range. The results of the plume radiation study given in the previous section indicated only an almost negligible additional 22 Btu/ft^2 sec of received power from the 40-foot length of viewed plume (before impingement) for this case. The approximate geometry of the plume impingement on the instrumented hold-down unit together with upstream plume properties are shown in Figure 36 for the two data points selected for this correlation study; assumed conditions for later use in developing alternate convection heat-transfer prediction methods are also shown.

At the technical conference held at Huntsville on January 27-28, 1965, with J. Cody and K. Mitchell, the investigation of the local flow field after a normal shock impingement was suggested. It was thought that the high shock and stagnation temperatures existing very near the instrumented plate surfaces could contribute a substantial portion of the difference between the predicted convective heat transfer rate and the high-measured rate. This calculation was made, and the details are presented here, but even with favorable assumptions such as full emissivity, configuration factor, and stagnation temperature recovery, the maximum thermal radiation rate was indicated to be only 18 percent (approximately) of the experimental 1100 Btu/ft^2 sec. It is of interest to note that a similar discrepancy between predicted and experimental heat transfer was reported by Cose and Lee in a Technical Note in the AIAA Journal (Reference 38). They found that for a solid-propellant rocket plume impinging on a nearby side plate, "heat transfer in the impingement zone was 500 to 600% higher than a turbulent

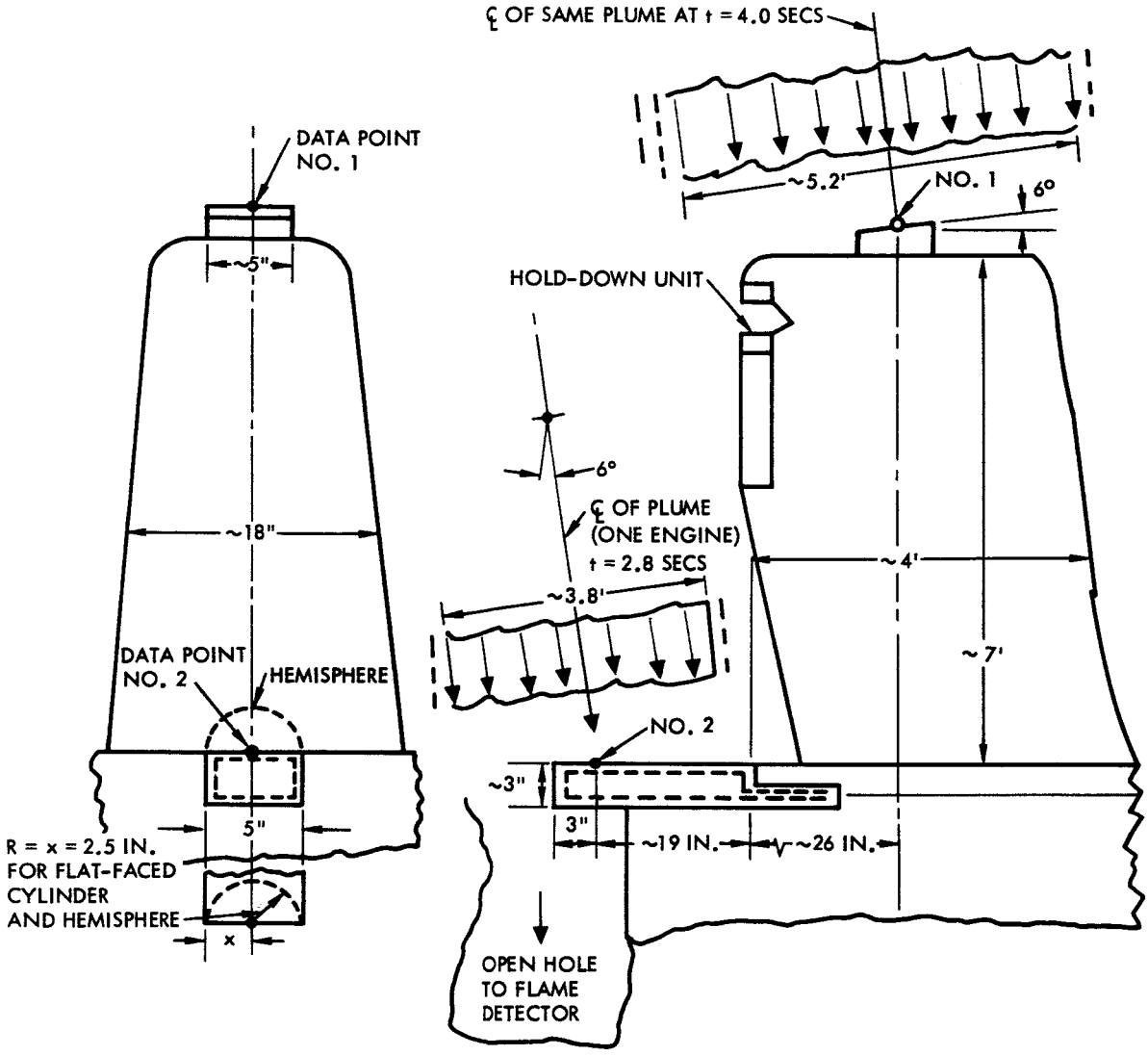

ASSUMED PLUME PROPERTIES BEFORE IMPINGEMENT

	DATA POINT NO. 1	DATA POINT NO. 2
VELOCITY, f/s	3200	5900
DENSITY, SLUGS/FT^3	3.8 X 10^{-4}	3.4 X 10^{-4}
TEMP, °R	2700	2900
GAS CONSTANT	61	67
PRESSURE, PSIA	14.7	14.7
SPECIFIC HEAT RATIO	1.23	1.23

Figure 36. Approximate Geometry of Jet Plume and Instrumented Data Points No. 1 and 2 for SA-5 Launch Data Correlation

boundary-layer analysis would predict (and) in this region, radiation was approximately 20% of the total heat transfer."

In the case under consideration (Data Point No. 2 in Figure 36), the full stagnation temperature, T_s,(with estimated upstream plume static temperature and velocity before impingement $T_1 = 2900°R$, and $V_1 = 5900$ ft/sec, respectively, gas specific heat ratio and gas constant, $k = 1.23$ and $R_g = 67$ ft lb/lb °R respectively), is

$$T_s = T_1 + V_1^2 \Big/ \frac{2gkR_g}{k-1} = 2900 + \left[\left(\frac{(5900)^2}{\frac{64.4 \times 1.23 \times 67}{0.23}}\right)\right] \qquad (77)$$

$$= 2900 + 1510 = 4410 \ °R$$

The maximum theoretical prediction for the thermal radiation from a flat shock disc at this temperature, which is so close to the instrumented plate that a configuration factor of one may be assumed, is:

$$q_{rs} = \sigma\epsilon F \left(T_s^4 - T_w^4\right) \qquad (78)$$

where

q_{rs} = stagnation value of thermal radiation, Btu/ft^2 sec

σ = Stefan-Boltzmann constant

$= 0.475 \times 10^{-12}$ Btu/ft^2 sec $(°R)^4$

ϵ = net emissivity (assumed = 1)

F = configuration factor (assumed = 1)

T_s = stagnation temperature, °R

T_w = wall temperature °R (effect of $(T_w)^4$ assumed negligible)

Inserting the estimated and assumed values of the parameters in Equation 78 yields

$$q_{rs} = 180 \ Btu/ft^2 \text{ sec}$$

Assuming the radiation from the nonimpinging, but viewed, plume to be additive, the maximum predictable radiation heat transfer for Data Point No. 2 becomes 22 + 180 = 202, or as stated earlier, about 18 percent of the average of the two maximum measurements of 1000 and 1200 Btu/ft^2 sec. This result supports the quoted estimate of about 20 percent of the total heat transfer attributed in Reference 38 to radiation.

C. CONVECTIVE HEAT TRANSFER

1. Determination of Flow Transition Location[1]

Based on a comparison with aerodynamic heating theory, different equations will be required depending on whether the impinging plume yields a normal or an oblique shock. These shock regions are shown schematically in Figure 37. In the oblique shock region, a further variation may be required, depending on whether the boundary layer is laminar or turbulent. The characteristic dimension used in aerodynamic heating calculations for a flat plate is taken to be the distance aft of the leading edge. For the present application, the corresponding distance would be the distance measured from the transition point between the normal and oblique shock regions to the point at which the heating rate is to be determined.

No simple relationship exists by which the point of transition may be computed, but the following procedure has been used in prior work on this problem. Shapiro (Reference 15) gives the following relationship for the maximum oblique angle for any particular Mach number and specific heat ratio.

$$\sin^2 \sigma_{max} = \frac{1}{kM_1^2}\left[\frac{k+1}{4} M_1^2 - 1 + \sqrt{(k+1)\left(1 + \frac{k-1}{2} M_1^2 + \frac{k+1}{16} M_1^4\right)}\right] \tag{79}$$

The relation for the corresponding deflection angle, δ_{max}, which produces this maximum oblique shock angle (e.g., see Reference 39) is:

$$\cot \delta_{max} = \tan \sigma_{max}\left[\frac{(k+1) M_1^2}{2\left(M_1^2 \sin^2 \sigma_{max} - 1\right)} - 1\right] \tag{80}$$

[1] This and the following two sections on convective heat transfer in the oblique and normal shock regions are based on a study made by J. W. Rolley, Power and Environmental Systems.

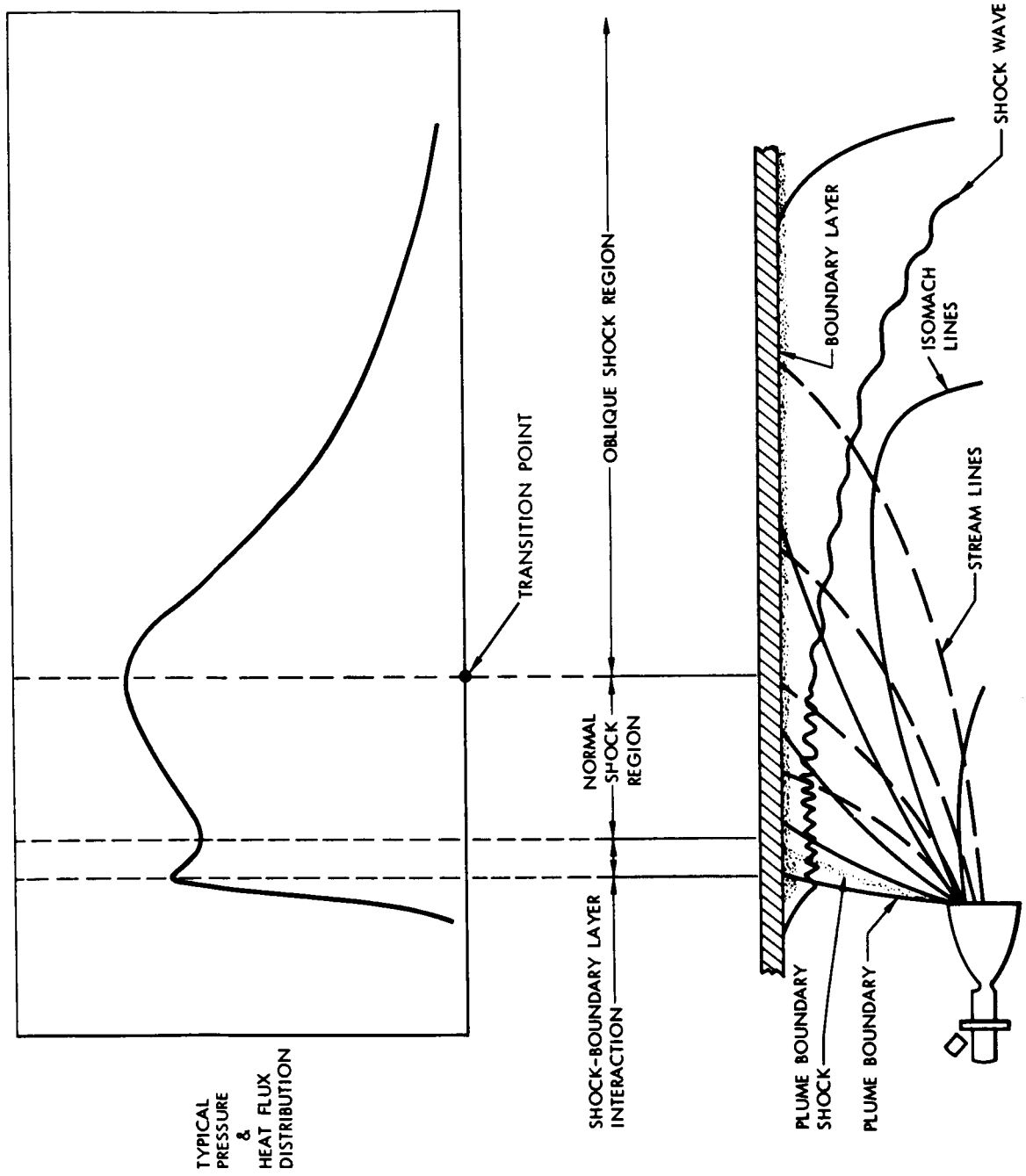

Figure 37. Jet Plume Heat Transfer Regions

This maximum deflection angle is plotted versus Mach number in Figure 38 for a number of values of specific heat ratio, and tabulated with the corresponding maximum shock angle, Mach number, and specific heat ratio in Table 13. At any particular point on the impinged plate, the Mach number and specific heat ratio determine if the impingement angle is greater or less than the maximum deflection angle. The transition point is assumed to be the location where the true impingement angle, θ_I, is greater than the maximum deflection angle for which an oblique shock can occur. The distance beyond this critical location is then $x - x_{cr}$ in the oblique-shock region.

2. Oblique Shock Region with Laminar Boundary Layer

In the region where the flow field produces an oblique shock with a laminar boundary layer, a preliminary correlation with experimental data has been obtained by computing the heating rate from the following equation which is a modified form of the Van Driest laminar flow equation for the oblique region (Reference 26):

$$q_{co_{(M_x<7)}} = \frac{1.49 \times 10^{-9}}{\sqrt{x - x_{cr}}} \left(\frac{\rho_x}{\rho_{o_{air}}}\right)^{0.5} U_x^{2.39} T_x^{0.383} \left[1 + \frac{5}{M_x^2}\left(1 - \frac{T_w}{T_x}\right)\right] \quad (81)$$

where

q_{co} = laminar flow convective heat transfer in the oblique shock region, Btu/ft^2 sec, for $M_x<7$

x_{cr} = axial location on the impinged plate from nozzle exit plane, where the flow changes from oblique to normal because the streamline impingement angle is greater than the maximum deflection angle for which an oblique shock can occur, ft.

x = axial location of point in the oblique shock region, ft.

ρ_x = mass density of gas before impingement, slugs/ft^3

$\rho_{o_{air}}$ = reference air mass density used in original development of equation to yield a dimensionless ratio with ρ_x, slugs/ft^3

U_x = velocity in direction parallel to plate, ft/sec.

T_x = temperature of gas before impingement, °R

T_w = wall temperature, °R

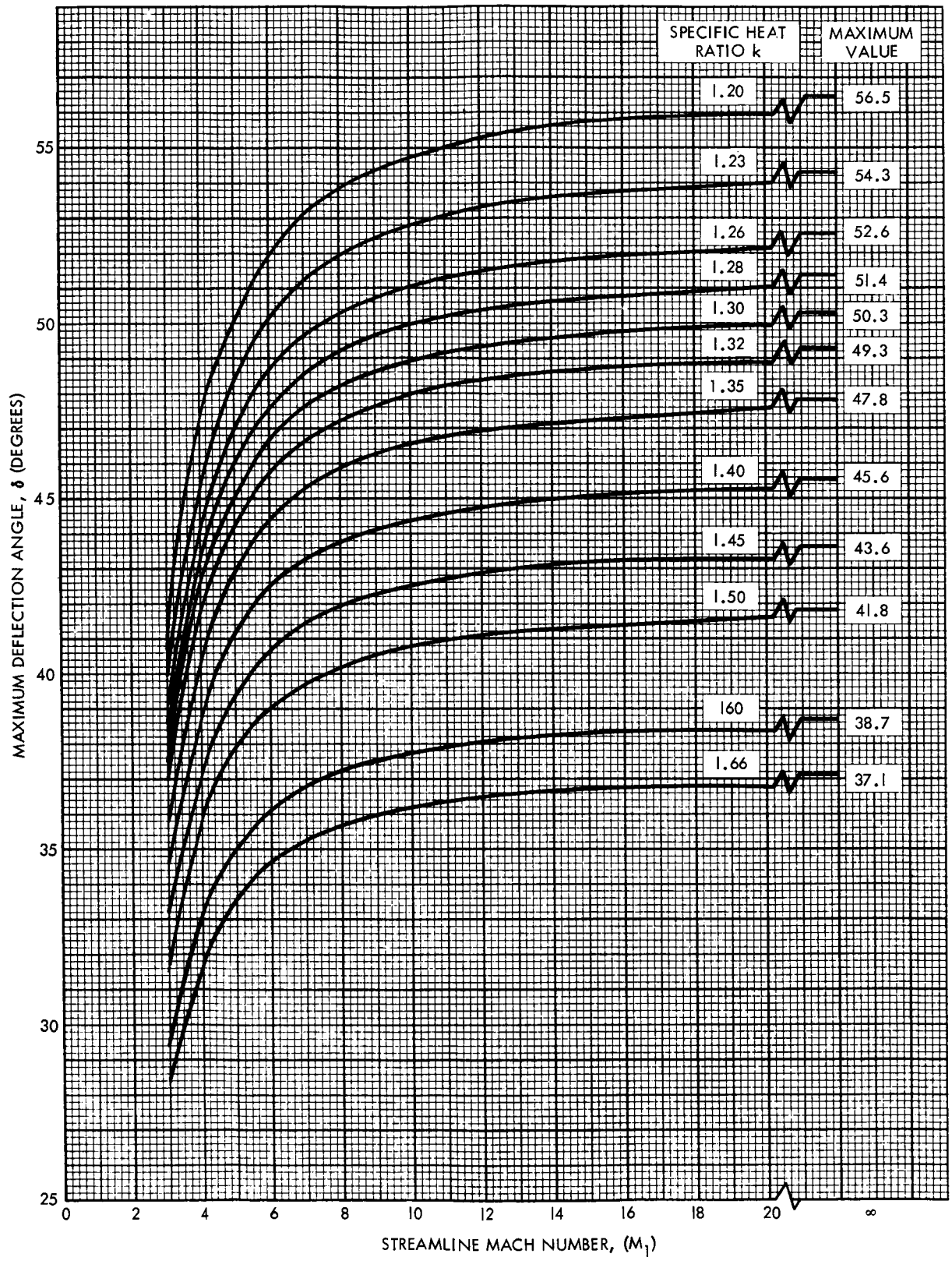

Figure 38. Maximum Deflection Angle for an Oblique Shock

Table 13. Maximum Oblique Shock and Flow Deflection Angles Versus Upstream Mach Number and Specific Heat Ratio

k	M_1	σ	δ
1.20	3	68.2	40.7
1.20	4	69.8	46.9
1.20	5	70.9	50.1
1.20	6	71.5	51.9
1.20	8	72.2	53.8
1.20	10	72.6	54.8
1.20	15	72.9	55.7
1.20	20	73.1	56.0
1.23	3	67.6	39.5
1.23	4	69.2	45.4
1.23	5	70.1	48.5
1.23	6	70.7	50.2
1.23	8	71.3	52.0
1.23	10	71.6	52.8
1.23	15	71.9	53.7
1.23	20	72.0	54.0
1.26	3	67.2	38.4
1.26	4	68.5	44.1
1.26	5	69.4	46.9
1.26	6	69.9	48.6
1.26	8	70.5	50.3
1.26	10	70.7	51.1
1.26	15	71.0	51.9
1.26	20	71.1	52.2
1.28	3	66.9	37.7
1.28	4	68.1	43.2
1.28	5	68.9	46.0
1.28	6	69.4	47.6
1.28	8	69.9	49.2
1.28	10	70.2	50.0
1.28	15	70.5	50.7
1.28	20	70.6	51.0

k	M_1	σ	δ
1.30	3	66.6	37.1
1.30	4	67.7	42.4
1.30	5	68.5	45.1
1.30	6	68.9	46.6
1.30	8	69.4	48.2
1.30	10	69.7	48.9
1.30	15	69.9	49.7
1.30	20	70.0	49.9
1.32	3	66.3	36.4
1.32	4	67.4	41.6
1.32	5	68.1	44.2
1.32	6	68.5	45.7
1.32	8	68.9	47.2
1.32	10	69.2	47.9
1.32	15	69.4	48.7
1.32	20	69.5	48.9
1.40	3	65.2	34.1
1.40	4	66.1	38.8
1.40	5	66.6	41.1
1.40	6	66.9	42.4
1.40	8	67.3	43.8
1.40	10	67.5	44.4
1.40	15	67.6	45.1
1.40	20	67.7	45.3
1.66	3	62.7	28.3
1.66	4	62.9	31.9
1.66	5	63.1	33.7
1.66	6	63.2	34.7
1.66	8	63.3	35.7
1.66	10	63.4	36.2
1.66	15	63.5	36.7
1.66	20	63.5	36.8

Equation 81 was used for computing the predicted convective heat transfer in the oblique shock region for several cases where experimental data were available from the Apollo SM-RCS program (Reference 26). These computations were made using theoretical values of the Mach number and impingement angle from prior results of the Apollo AP-214 Plume Program. The combustion chamber pressure measured at the injector end during the tests was assumed as the total pressure at the nozzle exit. The small test rocket engine used an Aerozine-50, N_2O_4 fuel-oxidizer mixture. The nozzle exit ratio was varied in these tests from 10:1 to 40:1. The side-impingement plate was mounted parallel to the engine center line and displaced a distance h = 3 to 17.5 R_e. The equation was evaluated by using an available IBM 7094 computer program. This program also contains a subroutine which computes the local properties, downstream of an oblique shock. Typical cases of the heating rates, calculated in this manner, are shown in Figures 39, 40, and 41, and in Table 14, along with the experimental data for the same conditions. Except for the excessively high values at, or close to, the transition point, when $x = x_{cr}$ in Equation 81 would yield an infinite rate, the correlation is good in most of the axial and transverse locations for this high-altitude plume.

However, when Equation 81 was used in the analysis of experimental heat transfer data for low-altitude plumes, the predicted values were far too low. Therefore, the derivation was studied to provide an understanding of its elements, and to indicate how its versatility could be improved. The rate of convective heat transfer to a flat, isothermal, plate with laminar boundary layer may be written as

$$q_c = h\,(T_r - T_w) \tag{82}$$

where the recovery temperature, T_r, is given by

$$T_r = T_x + r\left(\frac{U_x^2}{2J\,g_o\,c_p}\right) \tag{83}$$

Equation (82) in terms of Stanton Number ($C_H = h/\rho U c_p$) and with Equation (83) for the recovery temperature, yields

$$q_c = C_{Hx}\,\rho_x\,U_x\,c_p\left[T_x + r\left(\frac{U_x^2}{2J\,g_o\,c_p}\right) - T_w\right] \tag{84}$$

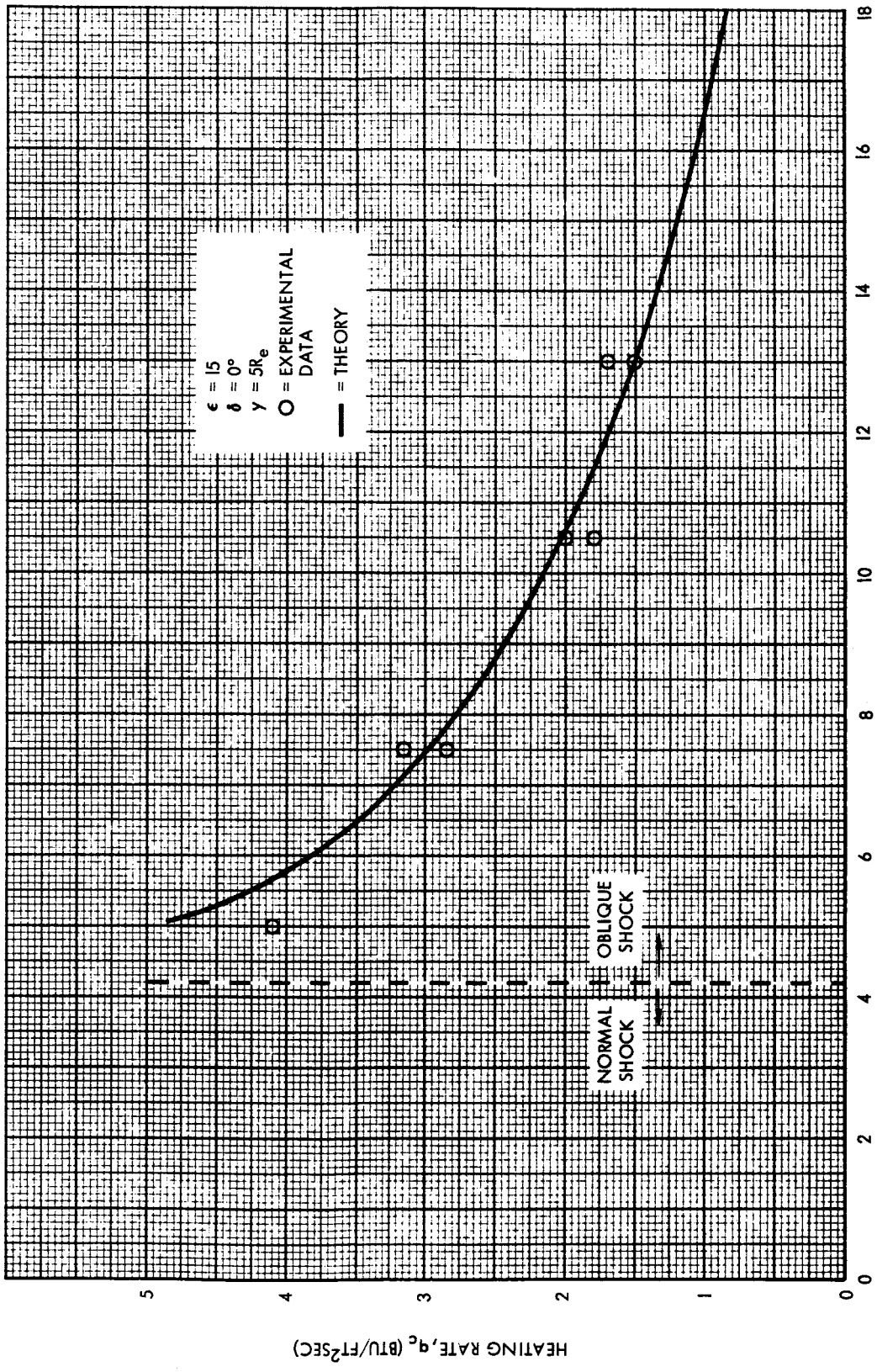

Figure 39. Correlation of Theoretical and Experimental Heating Rates (ϵ = 15)

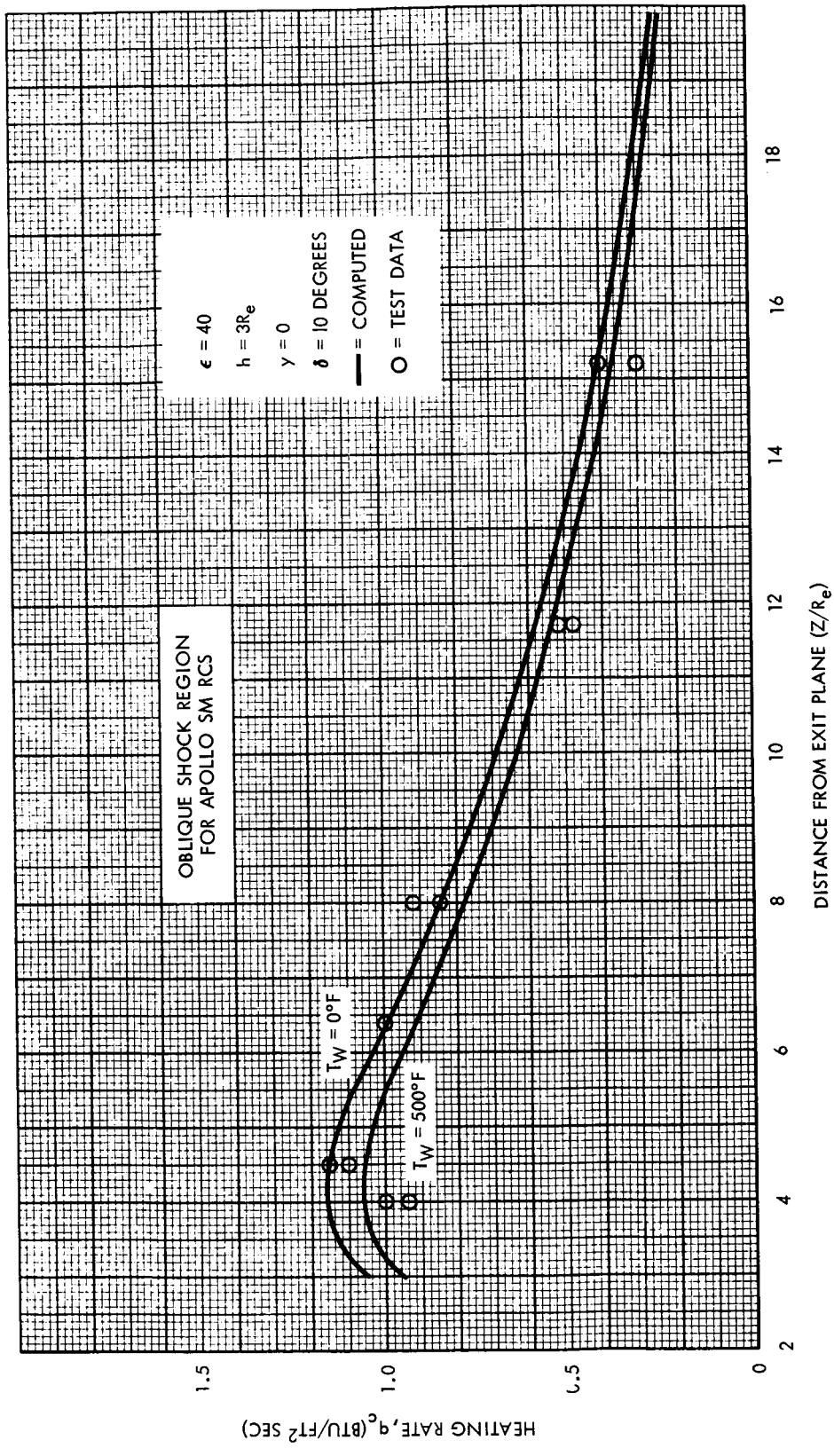

Figure 40. Correlation of Theoretical and Experimental Heating Rates (ϵ = 40)

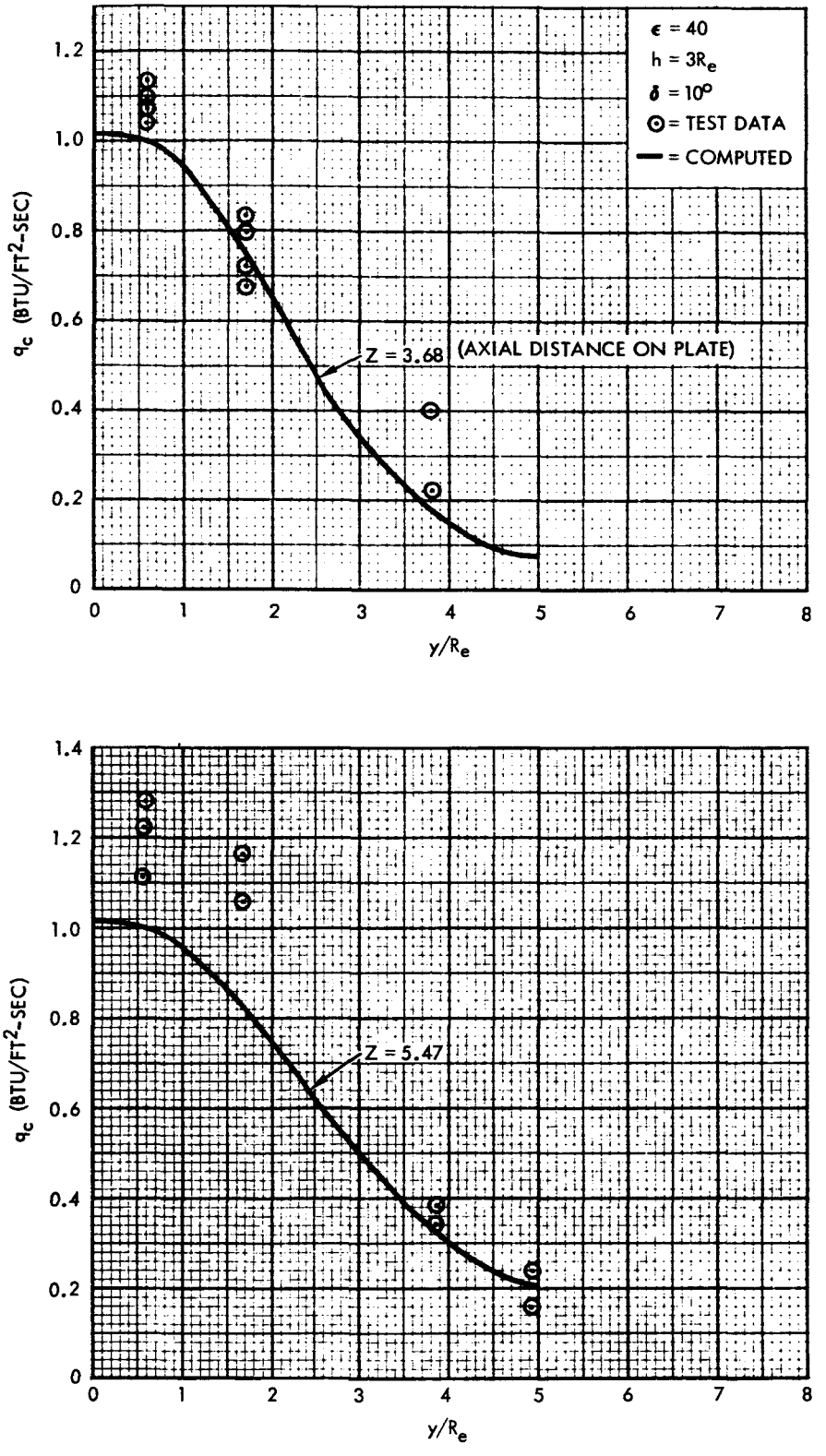

Figure 41. Correlation of Theoretical and Experimental Heating Rates in Two Transverse Planes

Table 14. Correlation of Predicted and Experimental Heating Rates in the Oblique Shock Region for Apollo SM-RCS Plume*

Position on Side Plate		Predicted Heating Rates (Btu/ft^2 Sec)	Experimental Heating Rates (Btu/ft^2 Sec)			
Axial (Z/R_e)	Transverse (y/R_e)					
2.4	0.55	0.85	0.79	0.75	0.77	0.89
2.4	1.65	0.47	0.54	0.59	0.68	
3.7	0.55	1.03	1.05	1.10	1.13	1.09
3.7	1.68	0.75	0.69	0.73	0.89	0.82
3.7	3.85	0.17	0.23	0.40		
5.5	0.55	1.05	1.11	1.11	1.23	1.28
5.5	1.65	0.84	1.06	1.16		
5.5	3.85	0.33	0.35	0.38		
5.5	4.95	0.20	0.16	0.24		
7.4	0.55	0.86	0.86	0.88	0.88	0.94
7.4	1.65	0.76	0.89	0.99		
7.4	2.75	0.58	0.64	0.64		
7.4	3.85	0.40	0.40	0.48		
7.4	4.95	0.27	0.30	0.21		
10.6	0.55	0.63	0.56	0.59		
10.6	1.65	0.57	0.63	0.67		
10.6	3.85	0.38	0.44	0.50		
10.6	4.95	0.30	0.31	0.35		

*Area expansion ratio $\epsilon = 40$; side plate cant angle relative to plume axis $\delta = 10°$ (making $Z/R_e = x/R_e/\cos 10°$);

distance of plate from nozzle center in nozzle exit plane, $h/R_e = 3$;

assumed wall temperature $T_w = 120$ F.

In order to arrange the equation so that the wall temperature appears in a correction factor, the heating rate may be expressed as

$$q_c = C_{Hx} \rho_x U_x c_p r \left(\frac{U_x^2}{2J\, g_o\, c_p} \right) F \tag{85}$$

where, as may be found by comparing Equations 84 and 85,

$$F = \frac{T_x - T_w + r\, \dfrac{U_x^2}{2J\, g_o\, c_p}}{r\, \dfrac{U_x^2}{2J\, g_o\, c_p}} \tag{86}$$

Rearranging Equation 86 and expressing the velocity in terms of Mach No. M_x and local velocity of sound, a_x, gives

$$F = 1 + \frac{T_x\, 2J\, g_o\, c_p}{r\, a_x^2\, M_x^2} \left(1 - \frac{T_w}{T_x} \right) \tag{87}$$

Substituting $a_x^2 = k\, g_o\, R_g\, T_x$ and $c_p - c_v = R_g / J$, for a perfect gas, in Equation 87 gives

$$F = 1 + \frac{2}{r M_x^2 (k - 1)} \left(1 - \frac{T_w}{T_x} \right) \tag{88}$$

If we let the recovery factor equal unity and substitute 1.4 for k (air) we have

$$F = 1 + \frac{5}{M_x^2}\left(1 - \frac{T_w}{T_x}\right) \tag{89}$$

From Equation 85 with the local flow conditions known and r assumed constant, every term, except the Stanton number, can be evaluated. Van Driest (Reference 40) presented a graph of $C_H \sqrt{Re_{xa}}$ versus Mach number and Harthun (Reference 41) empirically fit the curves by a relationship of the form

$$C_{Hx}\sqrt{Re_{xa}} = C_1 M_x^{C_2} \tag{90}$$

where

$$\left\{\begin{matrix} C_1 = +0.45 \\ C_2 = -0.115 \end{matrix}\right\} \text{ for } 2 < M_x \leq 7 \text{ and} \left\{\begin{matrix} C_1 = 0.65 \\ C_2 = -0.3 \end{matrix}\right\} \text{ for } M_x > 7$$

Substituting this expression for the Stanton number in Equation 85, but with $x_a = x - x_{cr}$ yields

$$q_c = \frac{C_1 M_x^{C_2}}{\sqrt{Re_{(x-x_{cr})}}} \rho_x c_{p_r} \frac{U_x^3}{2Jg_o c_p} \tag{91}$$

which, upon expanding the Reynolds number, becomes

$$q_c = \frac{C_1 M_x^{C_2} \mu_x^{1/2}}{U_x^{1/2} \rho_x^{1/2} \left(x - x_{cr}\right)^{1/2}} \left(\frac{r \rho_x U_x^3}{2Jg_o}\right) F \qquad (92)$$

Now expressing the Mach number in terms of the velocity, and approximating the viscosity as $\mu = \mu_o (T_x/T_o)^{0.65}$ where T_o is an assumed base temperature, and collecting terms, Equation 92 becomes

$$q_c = \frac{C_3}{\sqrt{x - x_{cr}}} \left(\frac{\rho_x}{\rho_o}\right)^{1/2} U_x^{2.5 + C_2} T_x^{\left(0.325 - 0.5 C_2\right)} F \qquad (93)$$

where

$$C_3 = \frac{C_1 r \mu_o^{1/2} \rho_o^{1/2}}{2Jg_o \left(kR_g g_o\right)^{\frac{C_2}{2}} T_o^{0.325}} \qquad (94)$$

Values of C_1 and C_2 corresponding to a local Mach number downstream of the shock and less than 7, and C_{3aver} using the properties of air ($r = 0.85$, $T_o = 492\ ^\circ R$, $\rho_o = 0.00237$ slugs/ft^3, and $\mu_o = 3.7 \times 10^{-4}$ slugs/ft sec) then result in Equation 81. The corresponding equation for Mach numbers greater than 7, but with $\sqrt{\rho_o}$ eliminated is:

$$q_{co_{(M_x > 7)}} = 9.07 \times 10^{-8} \sqrt{\frac{\rho_x}{x - x_{cr}}} T_x^{0.475} U_x^{2.2} \left[1 + \frac{5}{M_x^2}\left(1 - \frac{T_w}{T_x}\right)\right] \qquad (95)$$

The better correlation with test data, obtained with the use of air properties instead of exhaust gas properties, in evaluating the constant and the wall temperature correction factor presents an anomaly requiring additional correlation studies before resolution. As more rocket jet plume data accumulate over a wide range, the equation may be related more directly to the exhaust gas properties.

3. Convective Heat Transfer in Normal Shock Region

An available empirical equation giving the convective heat transfer in the normal shock region from the known upstream plume properties which was developed in prior S&ID Apollo work in this area (Reference 27) is:

$$q_{cn} = \frac{15200}{\epsilon + \frac{0.75h}{R_e}} \left(\frac{\rho}{\rho_{SL}}\right)^{0.5} \left(\frac{V}{V_m}\right)^{3.25} \left(1 - \frac{h_w}{h_s}\right) \qquad (96)$$

where

q_{cn} = convective heat transfer for normal shock, Btu/ft^2 sec

ϵ = nozzle area expansion ratio

$\frac{h}{R_e}$ = dimensionless distance in the nozzle-exit plane from center of nozzle to the impinged side plate

$\frac{\rho}{\rho_{SL}}$ = ratio of gas density before impingement to that of standard air at sea level

$\frac{V}{V_m}$ = ratio of gas velocity before impingement to maximum velocity in a vacuum, and

$\frac{h_w}{h_s}$ = ratio of gas boundary layer enthalpy at the wall to total enthalpy.

This equation was adapted from the Kemp and Riddell empirical satellite reentry heating equation (Reference 42), keeping the basic form, but replacing the value of the original constant (20, 800) by 15, 200 and the square root of the aerodynamic nose radius ($\sqrt{R}$) in the denominator by the expression $\epsilon + 0.75h/R_e$ to relate the equation empirically to the engine and test configuration.

The reciprocal of the square root of the reference air density is, of course, a constant which can be combined with the 15, 200 to give 55, 000 as the numerical coefficient. Also, the theoretical ratio of rocket exhaust velocity to its maximum under fully expanded conditions in a vacuum is simply the square root of the ratio of the nozzle expansion efficiencies $\sqrt{\eta/1} = \sqrt{1 - T_x/T_s}$. Finally, if the specific heat is assumed nearly constant, the ratio of local wall to stagnation enthalpy can be approximated by the temperature ratio T_w/T_s giving the simplified relation:

$$q_{c_n} = \frac{55000}{\epsilon + 0.75h/Re} \left(g_o \rho_x\right)^{0.5} \left(1 - \frac{T_x}{T_s}\right)^{1.625} \left(1 - \frac{T_w}{T_s}\right) \qquad (97)$$

Further modifications are desirable to make the relation dependent only on the impingement gas velocity or Mach number, density, and orientation. However, to permit the Phase II correlation effort to proceed on schedule, the form of Equation 96 or 97 was used. Upstream Mach numbers, streamline orientations, and constant nozzle-exit specific-heat ratio obtained from prior Apollo characteristics solution of jet plume free-flow fields were used, together with the estimated nozzle exit conditions and density and temperature ratios from the gas tables for isentropic expansion to evaluate this equation.

Comparison of the predicted and experimental convective heat transfer rates for this normal shock region are shown in Table 15 for various positions on a side plate parallel to the nozzle axis, for two area expansion ratios, and wall separation positions; again, the correlation appears to be good.

Table 15. Correlation of Predicted and Experimental Heating Rates in the Normal Shock Region*

Expansion Ratio ϵ	Separation h/R_e	Distance Z/R_e	Wall Temp** °F	Heating Rates Btu/ft^2-sec	
				Computed	Measured**
10	7	3.9	0	3.55	3.6
			500	3.23	
		6.1	0	5.4	4.2
			500	4.85	
	5	1.2	0	2.05	2.9
			500	2.35	
		3.7	0	7.3	8.2
			500	6.6	
15	7	5	120	2.55	2.1, 2.4
	5	3	120	3.1	3.45, 3.75

*For Apollo SM-RCS Plume (Cant angle $\delta = 0$ giving $Z/R_e = x/R_e$)
**Applies to computed heating rates only; wall temperature for measured heating rate between 70 and 200 F.

4. Stagnation Surface Heating Analysis[1]

Hoshizaki's simplified equation for stagnation surface heating (Eq. 21, Reference 43, for air) may be expressed as:

$$q_s = 2.59 \sqrt{\frac{p_s}{V_{max}}} \sqrt{\frac{dV}{dx_s}} \left[\frac{V_{max}}{10000}\right]^{2.19} \left(1 - \frac{h_w}{h_s}\right) \qquad (98)$$

[1]The sections on stagnation surface heating and turbulent flat plate heating, are based on the results of a study made for Power & Environmental Systems by G. M. Hanley and R. Norcross, of the S&ID Flight Sciences Department, particularly to evaluate the velocity gradient term typical in the aerodynamic heating equations, after it became apparent that alternate aerodynamic heating relations were needed in view of the low predictions from Equations 81 and 96 for the case of sea-level jet plume impingement.

where

q_s = stagnation surface heat transfer rate, Btu/ft^2 sec

P_s = stagnation surface pressure, psfa, evaluated from the upstream static pressure, p_1 = 14.7 psia, mass density $\rho_1 = 3.4 \times 10^{-4}$ slugs/ft^3; and plume velocity V_1 = 5900 ft/sec, for Data Point No. 2

$$= \rho_1 V_1^2 + p_1$$

$$= 3.4 \times 10^{-4} (5900)^2 + 14.7 \times 144$$

$$= 11840 + 2120$$

$$= 13950 \text{ psfa}$$

V_{max} = maximum gas velocity corresponding to total gas enthalpy, h_s, at upstream conditions

$$= V_1 \sqrt{\frac{T_s}{(T_s - T_1)}} = \sqrt{2gJ}\ \sqrt{h_s}$$

$$= 5900 \sqrt{\frac{4410}{(4410-2900)}} = 224 \sqrt{h_s}$$

$$= 10100 \text{ ft/sec; making } h_s = 2040, \frac{P_s}{V_{max}} = 1.38, \text{ and}$$

$$\left[\frac{V_{max}}{10{,}000}\right]^{2.19} = 1.02$$

$\left(\frac{dV}{dx}\right)_s$ = the stagnation point velocity gradient (sec^{-1})

$$\approx \left[\frac{J\left(\frac{dV}{dx}\right)_{\text{Flat faced cyl.}}}{J\left(\frac{dV}{dx}\right)_{\text{Sphere}}}\right]\left(\frac{V_1}{R}\sqrt{\frac{2\rho_1}{\rho_s}}\right) \qquad (99)$$

where the right hand expression in parentheses is the stagnation point velocity gradient of a spherical surface, thus permitting evaluation of the gradient by using the same radius as for the assumed flat faced cylinder, R = 2.5 in., or half the width of the instrumented plate shown in Figure 36, when the bracketed ratio value is available as a function of freestream Mach number from experimental data (Reference 44) as follows:

Mach Number	Ratio $\left[\frac{J\left(\frac{dV}{dx}\right)\text{Flat Faced Cyl.}}{J\left(\frac{dV}{dx}\right)\text{Sphere}}\right]$
1	(0.50)
2	0.45
3	0.42
4	0.40
5	0.38

(For Mach Number $M_1 = \sqrt{\frac{2}{k-1}\frac{T_s - T_1}{T_1}}$

$= \sqrt{\frac{2}{0.23}\left(\frac{1510}{2900}\right)} = 2.13,$

the corresponding experimental ratio is about 0.45, and with $\rho_1/\rho_s = (p_1/p_s)(T_s/T_1) = (2120/13950)(4410/2900) = 0.231$, the stagnation velocity gradient is evaluated as

$$\left(\frac{dV}{dx}\right)_s = 0.45 \frac{5900}{\left(\frac{2.5}{12}\right)} \sqrt{2 \times 0.231} = 8660 \text{ sec}^{-1},$$

and $\sqrt{8660} = 93.1$)

h_w = wall enthalpy, assumed at 120 Btu/lb, as a representative cold wall condition, and

h_s = total stagnation enthalpy of the plume gas at the upstream condition, already evaluated above as 2040 Btu/lb with the calculation for V_{max} for convenience, giving for the wall loss effect $(1 - 120/2040) = (.941)$.

Combining the factors evaluated above to show use of consistent units, Equation 98 now yields

$$q_s = 2.59 \times 1.38 \times 93.1 \times 1.02 \times .941 = 320 \text{ Btu/ft}^2\text{sec},$$

as the Hoshizaki stagnation heating rate for Data Point No. 2. With the radiation heat transfer added, the total heat transfer rate becomes 320 + 22 + 180 = 524 Btu/ft^2 sec, or only 46% of the experimental 1100 Btu/ft^2 sec[1].

[1]The possibility that the discrepancy might have been due to use of instrumentation beyond its temperature limit was investigated. Gardon (Reference 45) states that the reliable limit of an early design of the Constantan foil, heavy copper disc heat-sink type of calorimeter was only about 100 cal/cm^2 sec (368 BTU/ft^2 sec) for soft soldered leads, and about 150 cal/cm^2 sec (542 BTU/ft^2 sec) using a hard silver solder (M.P. 630°C) and a special nonlinear calibration of the emf-intensity relation. However, according to information received from NASA/MSFC, the thermocouple leads were welded in the SA5-SA6 instrumentation, and independently proved to be capable of recording the high heat transfer rates. Hence, the peak test values must be accepted as valid; and in an effort to improve the correlation, a second alternate analysis based on a turbulent flat plate heating condition was made.

5. Turbulent Flow Flat Plate Heating Analysis

This analysis is based on Reynold's modified skin friction relationship, the Blasius flat surface skin friction formulation, and Eckert's reference enthalpy method (Reference 46). The heating rate is based on the product of a turbulent heat transfer coefficient, H_T, and the available enthalpy difference between the recovery enthalpy, h_{reT}, and the wall enthalpy, h_w:

$$q_T = H_T (h_{reT} - h_w) \tag{100}$$

where the coefficient is empirically defined from test data as

$$H_T = 0.0358 (g_o \rho_s U_x)^{0.8} \left(\frac{\mu_s}{x}\right)^{0.2} \tag{101}$$

The density (lb/ft^3), evaluated at stagnation conditions (p_s = 13950 psfa, T_s = 4410 R, and R_g = 67), is:

$$g_o \rho_s = \frac{p_s}{R_g T_s}$$

$$= \frac{13950}{67} \times 4410$$

$$= 0.0472 \text{ lb/ft}^3 \tag{102}$$

The viscosity, μ_s, here evaluated at stagnation temperature, may be approximated by weighting the separate viscosities of the principal exhaust gases (CO_1, CO_2, H_2O), in the ratio 0.5, 0.25, 0.25, for 0.07, 0.08, 0.08 ctp, respectively, or:

$$\mu_s \approx f_1 \mu_1 + f_2 \mu_2 + f_3 \mu_3 +$$

$$\approx 0.075 \text{ centipoise, or at } 6.72 \times 10^{-4} \text{ lb/ft sec per ctp,}$$

$$\approx 5 \times 10^{-5} \text{ lb/ft sec} \tag{103}$$

Local velocity, U_x, results from the assumption that the flat plate stagnation velocity gradient remains constant across the transverse flow length x = R = 2.5 in. or 0.208 ft, or:

$$U_x = \left(\frac{dV}{dx}\right)_s x = 8660 \times 0.208 = 1800 \text{ ft/sec} \quad (104)$$

Combining the evaluated factors, the turbulent heat transfer coefficient becomes

$$H_T = 0.0358 \, (0.0472 \times 1800)^{0.8} \left(\frac{5 \times 10^{-5}}{0.208}\right)^{0.2}$$

$$= 0.0358 \times 34.9 \times 0.189 = 0.236 \text{ lb/ft}^2 \text{ sec}$$

With stagnation enthalpy h_s = 2040 Btu/lb, as before, and local enthalpy

$$h_x = h_s - \frac{U_x^2}{2gJ} = 2040 - \frac{(1800)^2}{50,000} = 1975 \text{ Btu/lb} \quad (105)$$

the recovery enthalpy is determined to be

$$h_{reT} = h_x + 0.18 \left(\frac{U_x}{100}\right)^2 = 1975 + 0.18 \left(\frac{1800}{100}\right)^2 = 2030 \text{ Btu/lb} \quad (106)$$

Substituting the values found for H_T and h_{reT} in Equation 100 with 120 again assumed as the cold wall enthalpy, the turbulent flat heating rate becomes:

$$q_T = 0.236 \, (2030 - 120) = 451 \text{ Btu/ft}^2 \text{ sec}$$

This result, with the estimated radiation rate from the non-impinging plume, 22, and from the shock disc, 180, together now indicate a predicted total heat transfer rate at Data Point No. 2 of 653 Btu/ft^2 sec. This total is in better agreement with the test value (59%) but still too low. A small additional amount of radiation is conceivable from the Mach shock discs in the plume upstream of the impingement plane. However, an estimate of the effect indicates it would increase the correlation with the total measured heat transfer rate by only about 5% for a total of 64%. To establish realistic relationships between the plume impingement environments and the results of prior experimental studies, further investigations along these lines are desirable over a wider range of cases to provide additional verification of the method.

D. CHARACTERISTIC VELOCITY OF HEAT TRANSFER

The turbulent heat transfer method of analysis presented in the previous section probably gives as good a correlation as can be expected in view of the complex local geometry and the rather sporadic test data available for the sevère case of sea-level plume impingement. For example, the duplicate instrumented data point located at the symmetrically opposed hold-down unit from Data Point No. 2 in the Saturn SA-5 launch (Figure 25) recorded jagged peaks and valleys of about 20% of the averaged maximum value. For Data Point No. 1, the measured peak values at the opposed locations with presumed similar jet-plume environments were widely divergent at 380 and 780 Btu/ft^2 sec, or 580 ±35%.

However, pending further improvements in both the parent aerodynamic heating relations and the experimental data, an independent check method of predicting the heat transfer due to jet plume impingement would be desirable. An approach to such a method is indicated by the observation of an apparent relationship between the average experimental heat transfer rates and the well-correlated theoretical and experimental plume impingement pressures. For example, if the simple linear ratio of the test $q_c/p_I = 1100/97 = 11.4$ Btu/ft^2 sec per psi for Data Point No. 2 is applied directly to the maximum recorded impingement pressure of 46 psia of Data Point No. 1, the resulting 525 Btu/ft^2 sec supports the average of the two divergent values within about 10%.

This q/p_I ratio would not be expected to be linear for other locations in the same plume or for other plumes and impingement environments. It will be shown subsequently that the fraction of the total energy flux of the jet plume transferred to the receiving instrumentation is very small for dense booster plumes (~1%) while it rises, along with the q/p_I ratio, for the tenuous high altitude plumes, as would be expected from the decrease in cushioning effect. The few cases available where both the heat transfer rates and impingement pressures were measured simultaneously, and accurately, are not sufficient to determine this variation at the present time. However, the following analysis presents a basis for exploring the relationship and planning future experimentation with this new concept in mind.

Let the general relationship for the ratio be defined as:

$$q_I = c_q^* p_I \tag{107}$$

where

q_I = total convective heat transfer rate, Btu/ft^2 sec, due to impingement

p_I = local impingement pressure, lb/ft^2, absolute, and

c^*_q = the ratio of the heat transfer rate to the impingement pressure, or characteristic velocity of heat transfer.

Looking at the dimensions of c^*_q for clues as to its characteristic, we find that one reduced dimension could be Btu/lb sec, a possible specific heat per unit of impulse. Or, preferably expanding Btu x J to ft-lbs of work done per ft^2 per sec per lb/ft^2 of impact pressure, the reduced dimensional unit becomes ft/sec, a pseudo-velocity somewhat analogous to the pseudo-velocity called characteristic velocity ("c*") of a rocket combustion chamber, which, however, is related to its capability for producing chamber gas pressure per unit of propellant mass flow rate per unit throat area, or "specific pressure"[1]. Similarly, the concept of c^*_q can be interpreted as the characteristic or specific heat transfer capability with respect to the easily measured or calculated impingement pressure.

If the energy flux were completely absorbed during impingement, the ceiling value for the heat transfer rate per square foot would be the maximum energy per pound of fluid, or the total enthalpy, h_s Btu/lb, times the corresponding weight flow rate per unit area, $\dot{w}/A$. The very small fraction of the total energy flux which cannot be diverted by the flow stream during impingement is here designated as f_1, (a variable, for different plume and impingement environments). Applying the continuity law, $\dot{w} = g\rho_1 A_1 V_1$, the impingement heat transfer rate may be expressed as:

$$q_I = f_1 \frac{dQ}{Adt} = f_1 \left(\frac{\dot{w}}{A_1}\right) h_s J$$

or (108)

$$q_I = gJf_1 \rho_1 V_1 h_s$$

[1] $c^* = \dfrac{g_o p_c A_t}{\dot{w}} = \dfrac{p_c}{\left(\dfrac{\dot{m}}{A_t}\right)}$

The total enthalpy of the plume stream is related to the upstream conditions by:

$$h_s = h_1 + \frac{V_1^2}{2gJ} = \frac{V_1^2}{2gJ\eta_1} \tag{109}$$

and

$$T_s = T_1 + \frac{V_1^2}{\left(\frac{2gkR_g}{k-1}\right)} \tag{77}$$

where

h_1 = static enthalpy due to p_1, ρ_1, T_1

$g = 32.2$ ft/sec^2

$J = 778$ ftlb/Btu

k = gas specific heat ratio, $\frac{c_p}{c_v}$

R_g = gas constant ft lb/mole lb °R

T_s = total stagnation temperature, °R.

and $\eta_1 = 1 - \frac{T_1}{T_s}$

Combining the above defined equivalents of q_I and p_I (normal) results in an expression for the heat transfer characteristic velocity:

$$c_q^* = \frac{q_I}{p_I} = \frac{gf_1\rho_1 V_1 h_s J}{p_1 + \rho_1 V_1^2} \tag{110}$$

Concrete values illustrating the new concepts are shown in Table 16 for the two plume data points of the Saturn SA-5 launch and for one of the Apollo SM-RCS plume data points.

Table 16. Numerical Examples of "Characteristic Velocity" of Heat Transfer and Related Parameters

Parameter	Units	SA-5 Data Point No. 1	SA-5 Data Point No. 2	Apollo Data Point No. 3*
h_∞	ft	0(S. L.)	0(S. L.)	~250,000
V_1	ft/sec	3200	5900	9400
ρ_1	slugs/ft^3	3.8×10^{-4}	3.4×10^{-4}	8.8×10^{-7}
T_1	degrees, R	2700	2900	480
k	-	1.23	1.23	1.28
T_s	degrees, R	3140	4410	5400
R_g	ft lb/lb mole °R	61	67	66
$\dot{w}/A$	lb/ft^2 sec	39	65	0.27
h_s	Btu/lb	1340	2040	2040
dQ/Adt	Btu/ft^2 sec	52,500	132,000	540
q_c(test)	Btu/ft^2 sec	580	1100	16
f_1	-	0.011	0.008	0.03
p_I(test)	lb/ft^2 (abs)	6000	13,950	78
c^*_q	(Btu/ft^2 sec)/psia	12.6	11.4	30
c^*_q	ft/sec	68	61	160

*For a parallel side plate at distance $h/R_e = 3$ from plume centerline, but assumed normal impingement into a turbulent zone.

Equation 110 apparently would give a zero value for c^*_q with $V_1 = 0$, thus lacks sufficient generality to include the effects of thermal radiation and its associated radiation pressure, and does not isolate the separate

contribution that a stagnated gas would make without turbulence. Figure 42(a), (b), and (c) illustrate proposed test setups that would

1. provide pure radiation without contact of the hot gas with the face of the calorimeter;

2. provide the heat transfer contribution of a stagnated gas with no transport velocity,

3. provide the customary combined heat transfer rate that would be measured by a calorimeter for the case of normal impingement.

A number of miniaturized pressure transducers and adjacent calorimeters (not shown in Figure 42) are required to show the relationship with impingement pressure.

Consideration of the separate inputs results in the more precise definition of the characteristic velocity of heat transfer as:

$$c_q^* = \frac{q_r + q_s + q_f}{p_r + p_s + p_f} \qquad (111)$$

where

q_r = heat transfer due to impact by impinging photons (radiation)

q_s = heat transfer due to impact by impinging molecules in accordance with the kinetic theory of gas pressure, without apparent transport velocity at the stagnation pressure conditions, but certainly with a statistical root mean square velocity and molecular flow rate which can be calculated. Conduction through a laminar static gas film would best describe this contribution, which would be obtained by subtracting q_r from the measured rate of 42(b).

q_f = heat transfer due to additional impact by molecules directed toward the surface by steady and unsteady vortex or eddy effects (turbulent heating). The case of heat transfer due to the principal toroidal vortex in equilibrium might possibly be tested and analyzed, together with the stagnation case. However, even if simply the difference between the heat transfer of the two isolated modes 42(a) and 42(b) and the normally measured total heat transfer 42(c) could be evaluated, such a test program would be expected to result in an advance in the state-of-the-art.

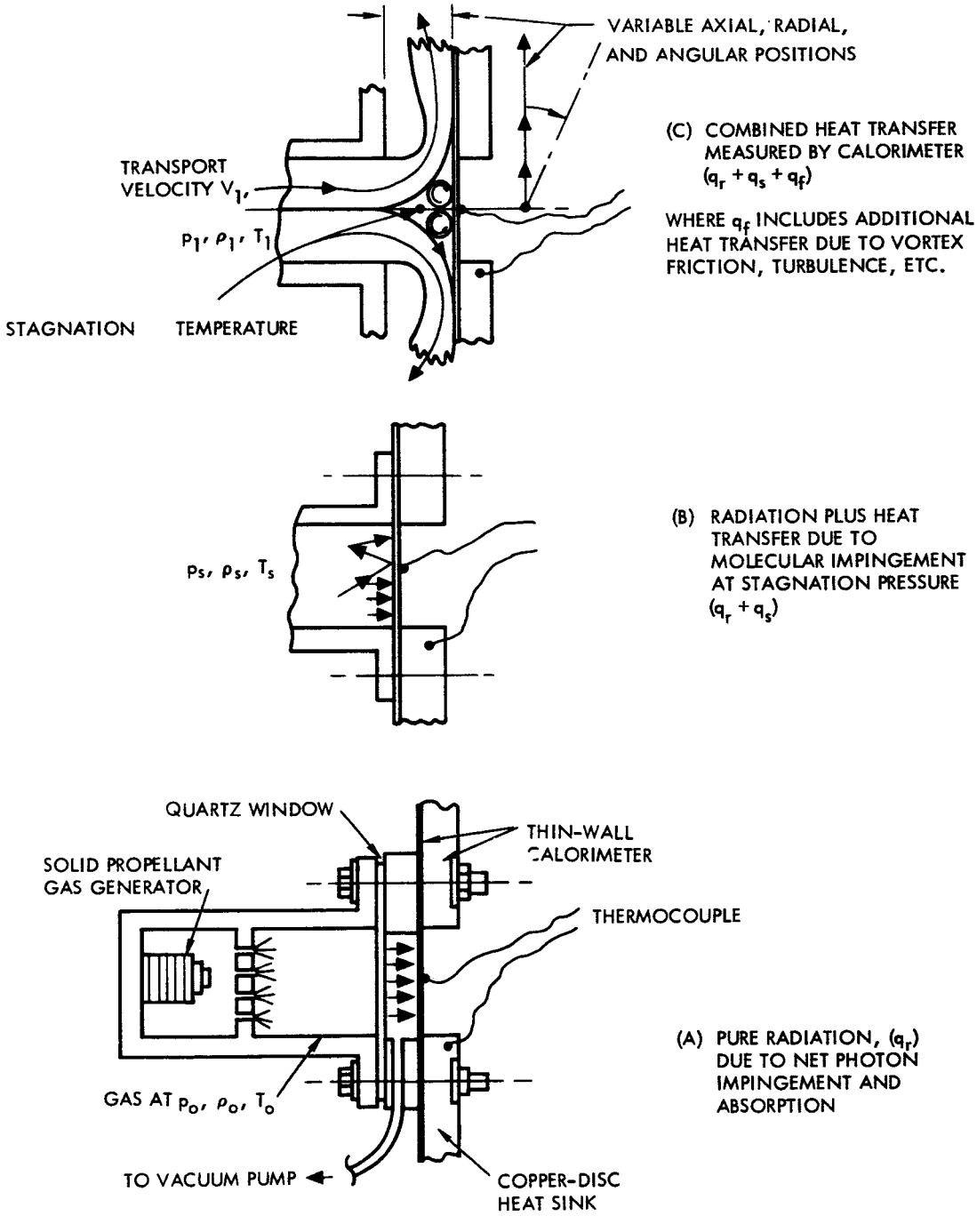

Figure 42. Proposed Test Setups for Isolating Basic Concepts of Heat Transfer Due to Rocket Jet Impingement

Equation 111 now permits an interesting limiting evaluation of the characteristic velocity parameter to be made. For a nonimpinging plume, the incident photons, in reality, do impinge on the surface of the thin-walled calorimeter. The maximum radiation heat transfer from the hot stagnation or shock disc layer to a cold black body receiver would be σT^4, or 180 Btu/ft^2 sec as previously found for Data Point No. 2 of the Saturn SA-5 launch data. The radiation pressure due to impingement and capture of these photons is very low, but is calculable in relation to the radiation heat transfer rate as follows:

$$\text{Pressure: } p_r = \frac{F}{A} \approx \frac{\dot{m}c}{A} \approx \frac{\rho A c^2}{A} \approx \rho c^2 \tag{112}$$

$$\text{Radiation: } q_r = J\sigma T_s^4 \approx \frac{\dot{m}c^2}{A} \approx \frac{\rho A c^3}{A} \approx \rho c^3 \tag{113}$$

$$\text{Characteristic Velocity: } c_q^* = \frac{q_r}{p_r} \approx \frac{\rho c^3}{\rho c^2} \approx c \text{ (in the limit)} \tag{114}$$

The amazing result of dividing Equation 113 by Equation 112, without worrying about the nature of "ρ" which hopefully cancels out, reveals the absolute ceiling value of the characteristic velocity of heat transfer as approaching the velocity of light![1] Figure 43 shows this limiting value on a plot of c_q^* vs h_s (in Btu/lb). With the aid of the asymptotic tangent line passed through this point ($h_{sc} \approx c^2/Jg_o$), a tentative prediction curve now can be drawn through the three test data points of Table 16.

A practical result of the foregoing exercise in imaginative analysis is to conclude that the radiation pressure may be dispensed with in the denominator of Equation 111 for the more typical heat transfer cases, while retaining the desired radiation rate in the numerator. It is also convenient to omit the extra pressure p_f due to the unknown vortex or eddy effects, leaving the empirical evaluation of f_1 in Equation 110 applied to the whole of the theoretical numerator of Equation 111, based on upstream rocket jet plume properties for predicting the total heat transfer relative to the

[1] The same ceiling value would result for the characteristic velocity of the photon rocket engine concept, from $c^* = g_o p_c A_t/\dot{w} = F/\dot{m} \approx \dot{m}c/\dot{m} \approx c$, when the ideal flat plate engine "nozzle" thrust coefficient would be $c/c^* = c/c = 1$. Since the generated plate pressure is simply a reverse impact (acceleration instead of deceleration) the two ceiling values of the characteristic velocity concepts are evidently not only related, but are one and the same for relating the transfer in energy flux and the pressure in the limiting case. Note that the solar radiation intensity at the earth's distance, in ft lbs/ft^{2}sec, divided by the corresponding radiation pressure, lbs/ft^2 (see Section IV C2), is the velocity of light.

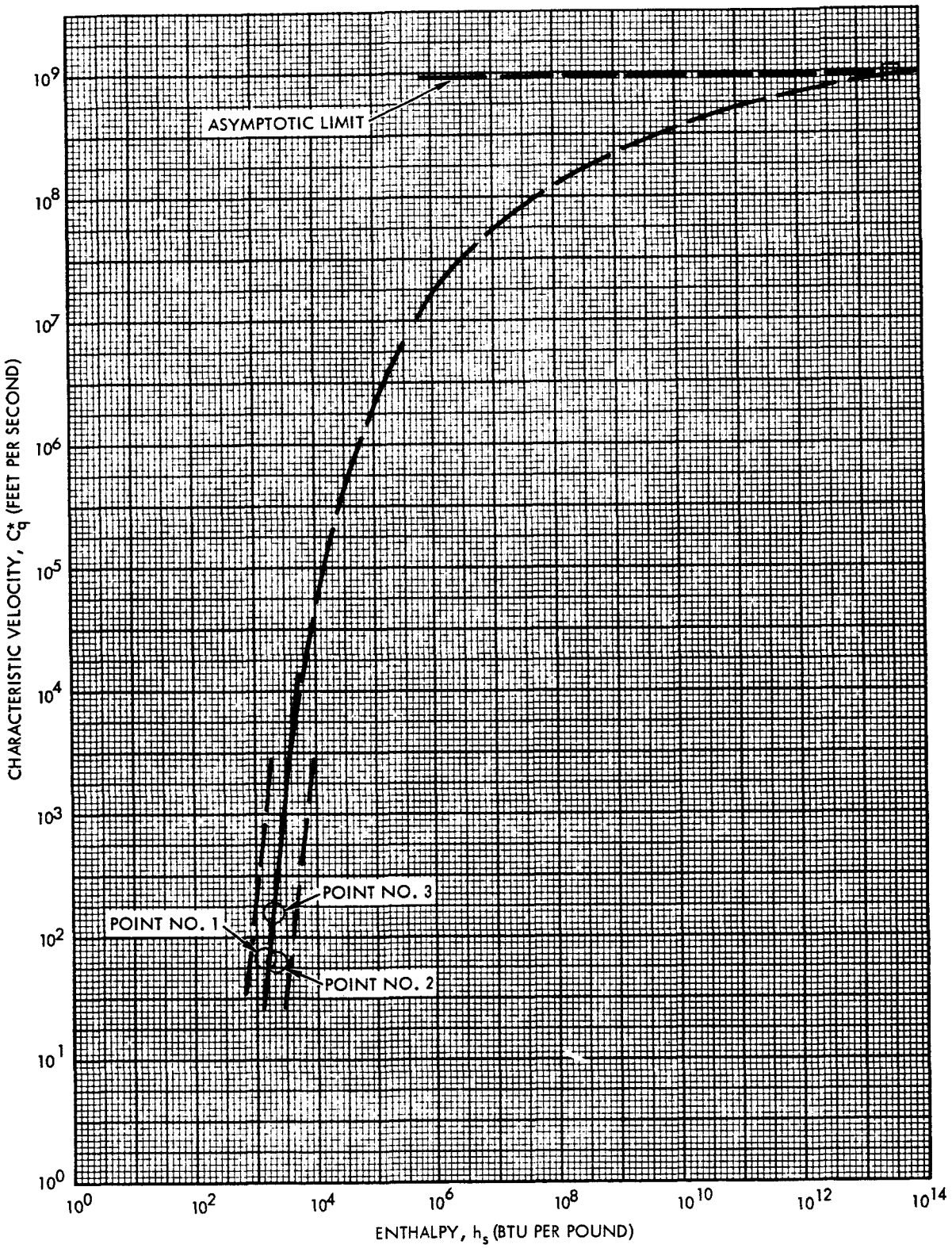

Figure 43. Tentative Prediction of Trend of Characteristic Velocity of Heat Transfer Versus Total Enthalpy of Rocket Jet Plume Before Impingement

calculable impingement pressure. An exponential decay-ratio function for distances radially away from the maximum value based on experimental data would be incorporated in this equation. It is believed that a special test program designed to develop empirical values of the ratio of the rocket jet plume heat transfer rate to impingement pressure for a variety of conditions of interest could yield some very promising new results which would help advance the state-of-the-art.

VI. CONCLUSIONS AND RECOMMENDATIONS

In general, the analytical investigations and their correlation with the available experimental data resulted in a set of prediction methods for the pressure and heat loads due to rocket jet impingement, which are as satisfactory as the state-of-the-art permits at this time. Specifically, the correlation of impingement pressures for high-altitude plumes impinging obliquely on flat side plates, and for low-altitude plumes impinging almost perpendicularly on flat plates may be considered remarkably good. The correlation of predicted heat transfer rates with test data for the high-altitude plumes is very good, and for the low-altitude plumes, only fair, but still adequate for design use with a suitable safety factor, pending further improvement of the prediction equations.

Simple Newtonian Impact Theory was found to be suitable for predicting impingement pressures in most of the normal and oblique shock laminar flow regions. The only exception occurs at the critical transition point, or area, when both the pressure and the heat transfer rate predictions fall below the corresponding peak experimental results. Since the background aerodynamic satellite reentry heating relations are related to test data by concrete parameters such as the radius of a leading edge and distance from this edge, which are only phantom concepts in the physical environments of the typical plume-flat plate impingement problem, difficulties in completely adapting these relations were to be expected. As additional reliable data becomes available, continued analytical studies are recommended to improve the present adaptations with respect to the effect of the properties of rocket plume gases on the empirical coefficients and exponents. Though yielding good correlation in certain narrow ranges where differences from the properties of air may be small, these "constants" can hardly be expected to apply universally because of the empirical conditions under which they were derived.

In addition, a special small-scale test program specially oriented to rocket exhaust plume effects is recommended to isolate the separate contributions of radiative, conductive, and convective heat transfer. Analysis of such data is expected to support the new concept of a characteristic velocity of total heat transfer related to the total impingement pressure comprising photon impingement, molecular impingement without transport velocity (stagnation pressure), and the additional effects of turbulent flow.

The section on jet plume impingement geometry presents a collection of original solutions for the sine of the true impingement angle not found

in published literature. Though based on classical analytical geometry, the objective sought is peculiarly related to the plume impingement problem. The visualization technique, repeatedly demonstrated in progressing from relatively simple flat plate impingement to the more complex cylinder and sphere impingement cases, should be useful in the application of the method to special problems. Continued effort is recommended to recast the solutions in a form suitable for general programming, and to correlate resulting predicted impingement pressures with new test impingement pressure data, particularly for cylinders and spheres.

The results of the shifting specific heat ratio study indicate that an appreciable decrease in the width of the free-flow field plume boundary occurs at high altitudes compared with the boundary width obtained by use of an assumed constant specific heat ratio. Apparently, the principal parametric cause of the shift in level to higher values of the specific heat ratio is the reduction in temperature as the gas expands; hence, little other difference resulted from the choice of equilibrium composition, frozen chamber composition, or a combined equilibrium-frozen case where predetermined "freezing point" criteria cause the computer program to shift from the equilibrium to the frozen condition. Some additional study is needed to conclude that the use of an effective constant value of specific heat ratio will provide accuracy adequate for most applications.

The preliminary results of a coaxial freestream interaction with the free-flow field jet plume boundary indicate the possibility of generating sets of useful influence coefficients based on a few "standard" jet plumes for selected environmental conditions to permit rapid estimates of the relatively small effects of minor variables to be made. Continuation of this approach toward feasible handling of the great number of possible combinations of jet plume parameters and operating altitudes is recommended.

Other existing plume impingement problem areas described in the early part of this report which need further development include the effects of reverse flow from clustered engine plumes into the vehicle base shield, the nonaxisymmetric plumes from scarfed nozzles, erosion and sooting effects, and the bending of jet plumes due to oblique air flow.

VII. REFERENCES

1. Engineering Method to Predict Saturn V Vehicle and Launch Complex Environments Due to Rocket Jet Impingement. RFQ, DCN 1-4-50-01213-01, NASA/MSFC (16 April 1964).

2. Proposal for an Engineering Method to Predict Saturn V Vehicle and Launch Complex Environments Due to Rocket Jet Impingement. NAA S&ID, SID 64-920 (14 May 1964).

3. Engineering Method to Predict Saturn V Vehicle and Launch Complex Environments Due to Rocket Jet Impingement, Quarterly Progress Report No. 1. Contract NAS8-11407, NAA S&ID, SID 64-1896 (15 October 1964).

4. Engineering Method to Predict Saturn V Vehicle and Launch Complex Environments Due to Rocket Jet Impingement, Quarterly Report No. 2. Contract NAS8-11407, NAA S&ID, SID 65-44 (15 January 1965).

5. Engineering Method to Predict Saturn V Vehicle and Launch Complex Environments Due to Rocket Jet Impingement, Quarterly Report No. 3. Contract NAS8-11407, NAA S&ID, SID 65-550 (15 April 1965).

6. Saturn V Service Arms, Preliminary Engineering Report, Complex 39, NASA TR-4-4-2-D (10 July 1963).

7. Roeck, G.D. Saturn General Protuberance Force and Pressure Wind Tunnel Test Report, Contract NAS7-101, Douglas Report SM-46670, Missile and Space Systems Division, Douglas Aircraft Co., Inc., Santa Monica, California (July 1964).

8. Goethert, B.H. "Base Flow Characteristics of Missiles with Cluster-Rocket Exhausts," Aerospace Engineering, Vol. XX, No. 3 (March 1961).

9. Goethert, B.H. Studies of the Flow Characteristics and Performance of Multi-Nozzle Rocket Exhausts. AEDC-TR-59-16, Arnold Engineering Development Center.

10. Morris, J.V., and A.J. Cannell. Basic Recirculation of a 1/10-Scale Saturn S-IV Stage at Simulated Altitudes Above 142,000 Feet. AEDC-TN-61-102, Arnold Engineering Development Center (August 1961).

11. Dehm, W.K., and H.B. Wilson. Some Preliminary Results of the Saturn Base Heating Program. AEDC TR-61-14, Vol. I, Symposium Proceedings, Arnold Engineering Development Center, June 28-29, 1961 (October 1961).

12. Matz, R.J., and D.W. Little. Experimental Investigation of the Influence of Altitude and Nozzle Geometry on the Base Flow Characteristics of a Four-Nozzle Cold Flow Rocket Model. AEDC-TN-61-125, Arnold Engineering Development Center (December 1961).

13. Maiden, C.J., and A.R. McMillan. An Investigation of the Protection Afforded a Spacecraft by a Thin Shield; paper presented at the AIAA Aerospace Sciences Meeting, 20-22 January 1964 (Preprint No. 64-95).

14. Latvala, E.K. Spreading of Rocket Exhaust Jets at High Altitudes. AEDC-TR-59-11, Arnold Engineering Development Center (June 1959).

15. Shapiro, A.H. The Dynamics and Thermodynamics of Compressible Fluid Flow, Vol. I, Ronald Press, New York (1953).

16. Adamson Jr., T.C. The Structure of the Rocket Exhaust Plume Without Reaction at Various Altitudes, Report of BAMIRAC 4613-45-T, University of Michigan, Ann Arbor, Michigan (June 1963)

17. Anderson, A.R., and F.R. Johns. "Characteristics of Free Supersonic Jets Exhausting into Quiescent Air," Jet Propulsion (January 1955).

18. Cody, J.C., and K. Mitchell. Personal Communication During Visit of Dr. W.H.T. Loh and A. Africano to NASA/MSFC, Huntsville, for Technical Discussions, 27-28 January 1965.

19. Love, E.S., C.E. Grigsby, L.P. Lee, and M.J. Woodling. Experimental and Theoretical Studies of Axisymmetric Free Jets, NASA Report TR R-6, (1959).

20. Cody, J.C. to A. Africano. Letter Transmitting SA5-SA6 Launch Test Data on Impingement Forces and Heat Loads for Analysis of Two Data Points. R-P&VE-PTE-64-L-99, NASA/MSFC, Huntsville (2 December 1964).

21. Wang, C.J., and J.P. Peterson. "Spreading of Supersonic Jets from Axially Symmetrical Nozzles," Jet Propulsion, ARS, May 1958.

22. Hoffman, R.J. Method of Characteristics Rocket Exhaust Plume Analysis Program, Phase I-Constant Ratio of Specific Heats. NAA S&ID SID 64-1217 (1 June 1964).

23. Kindle, J.H. Theory and Problems of Plane and Solid Analytic Geometry, Schaum's Outline Series, Schaum Publishing Company, New York (1950).

24. Bauer, R.C., and R.L. Schlumpf. Experimental Investigation of Free Jet Impingement on a Flat Plate. AEDC-TN-60-223, Arnold Engineering Development Center (March 1961).

25. Truitt, R.W. Hypersonic Aerodynamics, Ronald Press, New York (1959).

26. Piesik, E.T., and M.L. Lofland. High-Vacuum Plume Impingement Test Report, NAA S&ID, SID 63-1520 (24 February 1964).

27. Piesik, E.T. High-Vacuum Plume Impingement Test Correlation. NAA S&ID, SID 64-1563, Contract NAS9-150 (August 1964).

28. Seifert, H.S. (Ed). Space Technology, John Wiley and Sons, New York (1959).

29. DeSoto, S. The Radiation from an Axisymmetric, Real Gas System with a Non-Isothermal Temperature Distribution. Paper presented at the Seventh National Heat Transfer Conference (9-12 August 1964).

30. Penner, S.S. Quantitative Molecular Spectroscopy and Gas Emissivity. Addison-Wesley, Reading, Mass. (1959).

31. French, Dr. E.P. Effect of Rocket Exhaust Plumes on Operation of Infrared Earth Sensors. NAA S&ID, SID 64-251.(January 1964).

32. Stull, R.V., and G.N. Plass. Emissivity of Dispersed Carbon Particles, Journal, Optical Society of America, Vol. 50, No. 2 (February 1960).

33. Morizumi, S.J., and H.J. Carpenter. Thermal Radiation from the Exhaust Plume of an Aluminized Composite Propellant Rocket, Reprint No. 64-61, presented at the AIAA First Aerospace Sciences Meeting, New York (January 20-22, 1964).

34. Plass, G.N. "Mie Scattering and Absorption Cross-Sections for Aluminum Oxide and Magnesium Oxide," Applied Optics, Vol. 3, No. 7, July 1964.

35. Gryvnak, D.A., and D.E. Burch. Optical and Infrared Properties of Al_2O_3 at Elevated Temperatures, Philco Research Laboratories, Report V-2623 (May 1964).

36. Kliegel, J.R. Gas Particle Nozzle Flows. Paper presented at Ninth Symposium (International) on Combustion, Academic Press, New York (1963).

37. Carlson, D.J., and R.F. Hoglund. "Particle Drag and Heat Transfer in Rocket Nozzles," AIAA Journal, Vol. 2, No. 11 (December 1964).

38. Cose, D.A., and B.T. Lee. "Heat Transfer from an Impinging Jet," Technical Note, p. 173, AIAA Journal, Vol. 3, No. 1 (January 1965).

39. Equations, Tables, and Charts for Compressible Flow. NACA Report 1135 (1953).

40. Van Driest, E.R. Investigation of Laminar Boundary Layer in Compressible Fluids Using the Crocco Method, NACA TN-2597 (1952).

41. Harthun, M.H. "Derivation of Approximate Aerodynamic Heating Solutions," Aerodynamic Heating Manual, Vol. III, NAA Missile Division, ATS/60-169 (1960).

42. Kemp, N.H., and F.R. Riddell. "Heat Transfer to Satellite Vehicles Reentering the Atmosphere," Vol. 27, No. 2, Part 1, Jet Propulsion, ARS (February 1957).

43. Hoshizaki, R.M. "Heat Transfer in Planetary Atmospheres at Supersatellite Speeds," JARS, Vol. 32, No. 10 (October 1962).

44. Boison, J.C., and H.A. Curtiss. "An Experimental Investigation of Blunt Body Stagnation Point Velocity Gradient," JARS, Vol. 29, No. 2 (February 1959).

45. Gardon, R. "An Instrument for the Direct Measurement of Intense Thermal Radiation," Review of Scientific Instruments, Vol, 24, No. 5 (May 1953).

46. Eckert, E.R.G. Survey on Heat Transfer at High Speeds, WADC Technical Report 54-70, Wright-Patterson Air Development Center, Ohio (April 1954).

VIII. GLOSSARY OF SYMBOLS

A	area
a	speed of sound
α	integrated absorption (radiation)
β	azimuth angle
γ	gas specific heat ratio (gamma)
α, β, γ	space angles to XX, YY, and ZZ axes, respectively
B	Planck function at local gas temperature
C_H	Stanton number
c^*	gas characteristic velocity
c_q^*	heat transfer characteristic velocity
c_p	specific heat at constant pressure
c_v	specific heat at constant volume
c	velocity of light
D	diameter, distance
D_e	diameter of rocket engine nozzle exit
D_s	diameter of pitch circle of centers of clustered engines
Δ	axial downstream distance of effective point source (radiation)
$\frac{dV}{dx}$	velocity gradient in stagnation and flat plate turbulent flow analyses
δ	cant angle; stream deflection angle
δ_{max}	maximum stream deflection angle

ε	area expansion ratio; emissivity
F	force; wall temperature correction factor; shape factor
f_l	fraction of energy of impinging plume per unit area lost to heat transfer
Φ	elevation angle in plane perpendicular to reference plane (radiation)
g_o	standard acceleration of gravity
H_T	turbulent heat transfer coefficient
h	heat transfer coefficient; lateral distance of side impingement plate from center of nozzle exit
h_∞	ambient altitude
h_s	stagnation enthalpy
I	radiation intensity
I_ν	spectral intensity
J	mechanical equivalent of heat, 778 ft lb/Btu
K	constant; function of streamline and Mach angles; function of plume shape and composition (radiation)
k	specific heat ratio, c_p/c_v
k_e	effective specific heat ratio in nozzle exit plane
λ	wave length (radiation)
M	Mach number; molecular weight; mass
M_B	Mach number at plume boundary
M_e	Exhaust-gas Mach number at nozzle exit
M_∞	freestream Mach number

$\dot{m}$	mass flow rate
μ	viscosity; Mach expansion angle; absorption coefficient of bandwidth (radiation); micron
N	number; volume concentration of particles in a cloud
$\Delta\nu$	effective band width (radiation)
P	element of surface; radiant power per unit area
p	pressure
$p_{b1, b2}$	pressure at two plume boundary points
p_∞	ambient pressure
p_{Te}	total pressure at nozzle exit
p_I	impingement pressure
$p_{I_{mx}}$	maximum impingement pressure along centerline
p_{I_e}	impact pressure at nozzle exit (= $2\,q_e$)
$p_{I_{xs}}$	impact pressure at end of supersonic cone
p_T	total pressure
p_e/p_∞	ratio of average nozzle exit pressure to ambient pressure
p_L/p_∞	ratio of nozzle exit pressure at lip to ambient pressure
p_T/p_∞	ratio of total to ambient pressure
p_T/p_L	ratio total to exit pressure at nozzle lip
q	dynamic pressure equivalent, $\rho V^2/2$
q_c	convective heat transfer rate, Btu/ft^2 sec
$\frac{q_{mx}}{q_e}$	empirical decay ratio of maximum dynamic pressure along axial centerline to value at nozzle exit
R	radius; Rankine
R_e	radius of nozzle exit

R_g	gas constant
R_c	point location indicating center of radius
Re	Reynolds number
r_p	particle radius
r_{vs}	empirical ratio of subsonic axial velocity to local velocity of sound
r*	radius of nozzle throat
$r_{\Delta T}$	temperature difference ratio $(T_{mx} - T_\infty)/(T_e - T_\infty)$
R/R_e	ratio of transverse plume radius to nozzle exit radius
R_c/R_e	ratio of Latvala's circular arc radius to nozzle exit radius; ratio of cylindrical radius to exit radius
R/R_o	ratio of radial distance to half-velocity radius
R_o/R_e	ratio of transverse plume radius at half of axial velocity to nozzle exit radius
ρ	mass density
ρ_e	mass density at nozzle exit
ρ_x	mass density at axial distance x
ρ_1	mass density upstream of a shock
S	thickness of particle cloud (radiation)
S	entropy; distance along line of sight
Δs	path thickness; increments along line of sight (radiation)
σ	shock angle; Stefan-Boltzmann constant; cross-sections of solid particles
T	temperature

T_{mx}	maximum plume temperature along axis
T_e	plume temperature at nozzle exit
T_∞	ambient temperature; freestream temperature
T_{xs}	temperature along axis in subsonic portion of plume
t	temperature; time
τ	optical thickness (radiation)
θ	streamline flow angle with plume axis; azimuth angle (radiation)
θ_a	Prandtl-Meyer expansion angle (M = 1 to M∞)
$\theta_{b1, b2}$	plume boundary angle at 2 points
θ_B	plume boundary angle
θ_e	Prandtl-Meyer expansion angle (M = 1 to M_e)
θ_N	nozzle half-cone angle at exit
θ^*	azimuth angle from element to effective point source (radiation)
U	velocity in direction parallel to surface
V	velocity
V_s	velocity of sound
V_{ss}	axial subsonic velocity
V/V_{mx}	ratio of plume velocity in transverse plane to maximum velocity along axis
V_{mx}/V_s	ratio maximum axial velocity to local velocity of sound
$\dot{w}$	weight flow rate
W_p	carbon particle concentration, or density, g/cc
x	axial distance

x_p	coordinate of point of impingement in XX direction
x/R_e	dimensionless axial distance ratio to nozzle exit radius
$\Delta x/R_e$	increment beyond plume supersonic cone distance
y	coordinate in YY direction
Z	coordinate in ZZ direction

SUBSCRIPTS

a, ∞	ambient
B	boundary
b1, b2	boundary points
c	center; velocity of light
cc	concave cylinder
c*	gas characteristic velocity
c_q^*	characteristic velocity of heat transfer
cv	convex cylinder
cr	critical
e	exit
g	gas
I	impact, or impingement
i	species
L	lip
m,max	maximum
m	molecular
N	nozzle

n	normal
o	oblique; origin; reference; total
p	particle; point (of impingement); pressure
R	radius
r	radiation
re	recovery
s	shock; solid; sound; sphere; stagnation
T, t	total
t	tangent
v	velocity
w	wall
x	at axial distance x
xy	at axial distance x and transverse distance y